PolyPublie
Polytechnique Montréal

POLYTECHNIQUE MONTRÉAL
UNIVERSITÉ D'INGÉNIERIE

Titre: Title:	46 Sc Gamma-Ray Assembly for Studying Erbium and Erbium-Ytterbium Doped Optical Fibers for Space Applications
Auteur: Author:	Clarent Diep
Date:	2022
Type:	Mémoire ou thèse / Dissertation or Thesis
Référence: Citation:	Diep, C. (2022). 46 Sc Gamma-Ray Assembly for Studying Erbium and Erbium-Ytterbium Doped Optical Fibers for Space Applications [Mémoire de maîtrise, Polytechnique Montréal]. PolyPublie. https://publications.polymtl.ca/10742/

Document en libre accès dans PolyPublie
Open Access document in PolyPublie

URL de PolyPublie: PolyPublie URL:	https://publications.polymtl.ca/10742/
Directeurs de recherche: Advisors:	Cornelia Chilian, Jamal Chaouki, & Emile Haddad
Programme: Program:	Génie physique

Ce fichier a été téléchargé à partir de PolyPublie, le dépôt institutionnel de Polytechnique Montréal
This file has been downloaded from PolyPublie, the institutional repository of Polytechnique Montréal

https://publications.polymtl.ca

POLYTECHNIQUE MONTRÉAL

affiliée à l'Université de Montréal

46 Sc Gamma-Ray Assembly for Studying Erbium and Erbium-Ytterbium Doped Optical Fibers for Space Applications

CLARENT DIEP

Département de génie physique

Mémoire présenté en vue de l'obtention du diplôme de *Maîtrise ès sciences appliquées*

Génie physique

Décembre 2022

© Clarent Diep, 2022.

POLYTECHNIQUE MONTRÉAL

affiliée à l'Université de Montréal

Ce mémoire intitulé :

46 Sc Gamma-Ray Assembly for Studying Erbium and Erbium-Ytterbium Doped Optical Fibers for Space Applications

présenté par **Clarent Diep**

en vue de l'obtention du diplôme de *Maîtrise ès sciences appliquées*

a été dûment accepté par le jury d'examen constitué de :

Yves-Alain PETER, président
Cornélia CHILIAN, membre et directrice de recherche
Jamal CHAOUKI, membre et codirecteur de recherche
Émile HADDAD, membre et codirecteur de recherche
Nicolas GODBOUT, membre

DEDICATION

To my beloved family

ACKNOWLEDGEMENTS

First of all, I would like to thank Dr. Emile Haddad for believing in me and giving me the opportunity to work on this project. I am also grateful for his time, help and support throughout my master's, which helped me grow scientifically.

I want to thank my research director, Dr. Cornelia Chilian for giving me the chance to work with her team. Her time, support, and discussions have helped me realize this master's project while developing myself personally.

I'm beyond grateful to my colleagues in the department. To Ahmed Naceur, who supported and advised me throughout my master's degree and for our great discussions. To Darren Hall, who helped me with various concepts and also with the linguistic revision of my article.

Thank you to Dr. Yves-Alain Peter and Dr. Nicolas Godbout for agreeing to be part of my jury.

The last mention goes to my beloved family. Especially to my parents, Renée and Quoc, and my grandparents, for always being present and supporting me in many different ways and for encouraging me throughout my studies.

RÉSUMÉ

Avec l'effervescence de l'internet par satellite, la recherche pour le meilleur rendement des systèmes de télécommunication est essentielle pour offrir le débit le plus élevé. Dans ces systèmes, les fibres dopées aux terres rares (REDF), utilisées pour amplifier le signal, sont les principaux composants limitant le système. Leur efficacité est grandement affectée par leur exposition aux rayonnements présent dans l'espace. Ainsi, avant d'envoyer ces appareils en missions spatiales, un test d'irradiation accéléré est effectué sur les REDFs pour vérifier leurs performances face aux radiations. Ces tests utilisent un débit de dose au moins dix fois plus rapide que celui dans l'espace à des fins économiques et de gain de temps. Ceux-ci sont actuellement la norme en recherche et développement. Cependant, il existe une controverse sur l'effet du débit de dose d'irradiation sur les REDFs. Certaines études prétendent qu'un débit de dose plus faible induit une perte de performance plus importante, alors que d'autres prétendent le contraire.

Ce projet vise à clarifier le comportement des REDFs dans l'espace et à démystifier si leurs pertes sont plus importantes dans l'espace que dans les tests d'irradiation accélérés. Ce mémoire porte sur le développement et l'utilisation d'un nouveau test d'irradiation accéléré pour les REDFs atteignant un débit de dose analogue à celui dans l'espace.

Basé sur le ^{46}Sc au lieu du ^{60}Co habituellement utilisé, cet irradiateur gamma à faible débit de dose a permis l'étude de performance de sept amplificateurs à fibre dopée aux terres rares (REDFAs). Dans ce test, seules les fibres étaient exposées aux rayonnements gamma, leur induisant une atténuation induite par rayonnement (RIA), alors que les parties électroniques et optoélectroniques des amplificateurs étaient en dehors de la zone d'irradiation.

La structure mécanique de l'irradiateur a été conçue et construite de forme cylindrique de 208 mm de hauteur par 102 mm de diamètre extérieur. Ces spécifications ont été choisies afin que l'irradiateur puisse s'insérer dans un blindage cylindrique en plomb, abritant l'installation avec les sources radioactives. Ces sources étaient constituées de quatre flacons remplis de ^{46}Sc positionnés sur l'axe de révolution du cylindre. Ceci a permis un débit de dose de rayons gamma homogène à la surface du cylindre, là où les fibres optiques étaient enroulées.

L'activité relative et la position de chaque capsule de ^{46}Sc dans le montage ont été modélisées et optimisées afin d'obtenir une distribution des rayonnements gamma homogène de la surface du cylindre de l'irradiateur sur sa longueur. Cette modélisation point par point, programmée en Python

3.7, a considérée l'activité des sources et leur autoprotection spatiale formée par activation neutronique dans le réacteur nucléaire SLOWPOKE-2, et l'atténuation des rayons gamma. Une fois les sources activées, l'irradiation des fibres a débuté avec un débit de dose initial de 27 rad/h sur les fibres. En raison de la demi-vie du ^{46}Sc, ce débit de dose a diminué à 1,1 rad/h à la fin de l'irradiation, atteignant une dose totale de 75 krad après 382 jours.

De plus, dans les satellites, il y a des REDFAs sous forme active, étant fonctionnels et pompés pendant leur mission, et des REDFAs redondants de secours, étant inactif, par conséquent sous forme passive. Quatre ensembles de sept REDFs ont été irradiés, soit sous une forme active ou passive, pour étudier les effets du rayonnement sur les fibres et sur leurs formes. Le premier ensemble de fibres était sous forme active, subissant du photoblanchiment, un contre mécanisme de la RIA. Leur puissance de sortie était comprise entre 20 dBm, représentant les liaisons optiques intrasatellites, et 30,6 dBm, représentant les liaisons optiques intersatellites. Trois autres ensembles ont été irradiés sous forme passive, un ensemble pour une dose totale de 60 krad et deux autres pour 30 krad à différents débits de dose.

Cet irradiateur a permis d'atteindre un faible débit de dose, d'environ un ordre de grandeur inférieur aux débits de dose couramment utilisés (200-400 rad/h) dans les tests de rayonnement gamma pour REDFs. À notre connaissance, c'est la première fois qu'un test de rayonnement pour REDFs est effectué à un débit de dose aussi faible, proche du débit auquel les satellites en orbite terrestre basse (LEO) et en orbite équatoriale géostationnaire (GEO) sont exposés. Ceux-ci sont généralement compris entre 0,1 et 10 rad/h, en fonction de leur orbite et du blindage total des fibres optiques à l'intérieur du satellite.

Ce projet de maîtrise est principalement consacré à la réalisation de l'irradiateur, plus précisément la conception et la fabrication de l'assemblage mécanique, la modélisation de l'irradiation gamma, l'activation des sources et le montage des instrumentations en laboratoire avec l'acquisition des données. Il présente également un aperçu préliminaire des données des fibres actives acquises lors de l'irradiation sous photoblanchiment et des données des fibres passives après irradiation, incluant une comparaison préliminaire entre elles. Il compare également les données d'une même fibre irradiée lors d'un test précédent sous ^{60}Co et de ce test sous ^{46}Sc.

Plusieurs tests expérimentaux et analyses doivent être poursuivis pour étudier les effets des rayonnements sur les fibres irradiées. De plus, un modèle mathématique pourrait être développé sur l'effet du RIA et du photoblanchiment sur les fibres à partir de ces données.

ABSTRACT

With the effervescence of the Internet by satellite, the search for the best yield of the telecommunication systems is essential to offer the highest bit rate. In these systems, rare-earth doped fibers (REDFs), used to amplify the signal, are the main components that limit the system. Their effectiveness is greatly affected by their exposure to radiation present in space. Thus, before sending these devices for space missions, a terrestrial accelerated-radiation test is carried out on the REDFs to verify their performance against radiation. These tests use a dose rate at least ten times faster than that in space for economic and time-saving purposes. They are currently the standard in research and development. However, there is a controversy over the effect of the irradiation dose rate on REDFs. Some studies claim that a lower dose rate induces greater performance loss, while others claim the opposite.

This project aims to clarify the behavior of REDFs in space and to demystify whether their losses are more significant in space than in accelerated-radiation tests. This thesis focuses on developing and using a new terrestrial accelerated-radiation test for REDFs with a dose rate analogous to that in space.

Based on ^{46}Sc instead of ^{60}Co customarily used, this low dose rate gamma irradiator allowed the performance study of seven rare-earth doped fiber amplifiers (REDFAs). In this test, only the fibers were facing gamma-ray irradiation, producing radiation-induced attenuation (RIA) on them, whereas the electronic and optoelectronic parts of the amplifiers were outside of the irradiation area.

The irradiator mechanical structure was designed and built in a cylindrical shape of 208 mm in height and 102 mm in outer diameter. These specifications were chosen so that the irradiator could be inserted into a cylindrical lead shielding that was hosting the installation with the radioactive sources. These sources consisted of four vials filled with ^{46}Sc positioned on the axis of revolution of the cylinder. This allowed a homogeneous gamma-ray dose rate on the surface of the cylinder, where the optical fibers were spooled.

The relative activity and position of each ^{46}Sc vial in the setup were modeled and optimized to obtain homogeneous radiation distribution along the surface of the irradiator cylinder. This point-by-point modeling, programmed in Python 3.7, considered the activity of the sources, their neutron self-shielding during the neutron activation in the SLOWPOKE-2 nuclear reactor and the gamma-

ray attenuation by the layers separating the source from the fibers. Once the sources were activated, the irradiation of the fibers started with an initial dose rate of 27 rad/h on the fibers. Due to the ^{46}Sc half-life, this dose rate decreased to 1.1 rad/h at the end of irradiation, reaching a total dose of 75 krad after 382 days.

Moreover, in satellites, there are REDFAs in active form, being functional and pumped during their mission, and redundant backup REDFAs, being inactive, therefore in passive form. Four sets of seven REDFs were irradiated, either in an active or passive form, to study the effects of radiation on the fibers and their form. The first set of fibers was in active form, undergoing photobleaching, a counter mechanism of RIA. Their output power ranged between 20 dBm, representing intra-satellite optical links, and 30.6 dBm, representing inter-satellite optical links. Three other sets were irradiated in passive form, one set for a total dose of 60 krad and two others for 30 krad at different dose rates.

This irradiator generated a low dose rate, about one order of magnitude lower than the dose rates commonly used (200-400 rad/h) in gamma radiation REDFs tests. To our knowledge, this is the first time that a radiation REDFs test has been performed at such a low dose rate, close to the rate at which satellites in low Earth orbit (LEO) and geostationary equatorial orbit (GEO) are exposed. These are commonly between 0.1 and 10 rad/h, depending on the orbit and the overall shielding of the optical fibers inside the satellite.

This master's project is mainly dedicated to the implementation of the irradiator, more precisely the design and fabrication of the mechanical assembly, the modeling of the gamma irradiation, the activation of sources, and the assembly of the instrumentation in the laboratory with the data acquisition. It also presents a preliminary overview of data taken from active fibers during irradiation under photobleaching and the data from passive fibers after irradiation including a preliminary comparison between them. It also compares the data of the same fiber irradiated during a previous test under ^{60}Co and this test under ^{46}Sc.

Several experimental tests and analyzes must be pursued to investigate the effects of radiation on REDFs. Moreover, a mathematical model could be developed on the effect of RIA and photobleaching on the fibers from these data.

TABLE OF CONTENTS

LIST OF TABLES

LIST OF FIGURES

LIST OF SYMBOLS AND ABBREVIATIONS

CC	Color center
COTS	Component of-the-shelf
DIAL	Differential absorption light detection and ranging
EDFA	Erbium-doped fiber amplifier
ELDRS	Enhanced low-dose-rate sensitivity
ESA	European Space Agency
EYDFA	Erbium-ytterbium doped fiber amplifier
FOG	Fiber optical gyroscope
FSO	Free space optic
GCR	Galactic Cosmic Rays
GEO	Geostationary equatorial orbit
HVL	Half value layer
IL	Insertion loss
LEU	Low enrichment uranium
LIBS	Laser induced breakdown spectroscopy
LIDAR	Light detection and ranging
LEO	Low earth orbit
RE	Rare earth
REDF	Rare earth doped fiber
REDFA	Rare earth doped fiber amplifier
RIA	Radiation induced attenuation
SAA	South Atlantic Anomaly

SI	International system of units
WDM	Wavelength division multiplexing

CHAPTER 1 INTRODUCTION

In 1985, the first reproducible technique for the uniform incorporation of ions in the core of an optical fiber was achieved [1]. This technique represents the creation of a reliable rare earth doped fiber amplifier (REDFA). Two years later, in 1987, the first erbium-doped fiber amplifier (EDFA) was created [2]. This fiber working in the 1550 nm window, revolutionized the telecommunication field for minimum attenuation in the silica-based fiber of 0.15 dBm/km [3]. Since then, REDFAs are widely used in telecommunications for data amplification by taking advantage of the spectroscopic proprieties of rare earth (RE) ions such as erbium, ytterbium, and a combination of them. REDFAs allow transmission over a long distance in the telecommunication wavelength band with a high gain, a low noise, a low insertion loss (IL) and the ability to amplify multiple optical signals simultaneously [4, 5].

Those advantages make the optical transmission system interesting for other fields, including space applications. Their small size, light weight, large bandwidth, and low power consumption make them good candidates in this field [6]. Moreover, the optical transmission system is immune to electric interference, making them suitable for transmitting information in the radiative environment of space. Radioactive particles of various types and energies make space a harsh radiation environment and deteriorate the components and instruments of spacecraft bombarded with ionizing radiation.

Under the pressure of the expansion of the internet, while looking for the highest bit rate, the internet by satellite is booming, requiring the highest yield using the minimum energy. However, EDFAs and erbium-ytterbium doped fiber amplifiers (EYDFAs) are the major limiting factor in REDFAs caused by their sensitivity to radiation [7, 8]. When exposed to radiation, electrons and holes are trapped in the amorphous silica network of the REDFAs, called color center (CC) or point defects. This modification in the silica network is at the origin of the radiation induced attenuation (RIA), the optical gain reduction increasing with the irradiation dose [9-12]. This gain reduction depends on the core composition, primarily on the co-dopant used to fabricate the REDFAs and not the RE dopant itself [13].

Facing this challenge, producers of optical fibers are developing radiation-hardened EDFs and EYDFs for decreasing the radiation sensitivity of their fibers. However, the high cost of those fibers limits the commercialization of these technologies. Commercial off-the-shelf (COTS) devices are now commonly used in space missions. Since space technologies require extreme reliability caused by the severe cost of space missions and the impossibility of repairs, COTS optic components need to pass several tests [14]. One of those tests is the radiation hardness assurance usually done by a terrestrial accelerated-radiation test on components.

This test is intended to simulate the space radiation environment to quantify the performance of rare earth doped fibers (REDFs) to study the RIA on REDFA and is mainly done using ^{60}Co. With this isotope, REDFs are under radiation with dose rates usually between 100 rad/h and 400 rad/h and can be up to 44 krad/h [9, 15, 16]. However, dose rates are estimated to be between 0.1 and 10 rad/h for fibers in satellites, depending on the total fiber shielding and the satellite orbit. Then, accelerated radiation tests have a dose rate up to 10 times higher than in space for time and cost-efficiency [17, 18].

This difference in the irradiation dose rate between the space and the accelerated-radiation tests has raised questions about its effect on RIA, generating controversy on the effect of the irradiation dose rate on REDFs, which is still unclear. Many researchers claim that a lower dose rate induces a higher RIA [11, 19, 20]. Likewise, a theoretical approach suggests that above a dose rate threshold, defined mainly by the characteristics of the fiber, the RIA can be six times lower than a low dose rate under this threshold [12]. However, those results and this theory are not observed in all the tests carried out in laboratories showing the RIA increasing with a higher dose rate [17, 18, 21]. Furthermore, the REDFA of the European Space Agency (ESA) Proba-2 satellite in service is exposed to a low dose rate of an average of 1.11 krad per year and does not demonstrate a higher than expected RIA as observed with the accelerated-radiation test [22]. Therefore, low dose rate radiation environments, like space, tested with accelerated gamma irradiation, should be re-examined.

1.1 Research Objectives

The main objective of this research is to create a gamma-ray irradiator using ^{46}Sc. This radioisotope, never used for this type of irradiation, allows irradiation with gamma energies similar to ^{60}Co, the current standard, but with a lower dose rate and closer to the one's space satellites are exposed to. Furthermore, the short half-life of the ^{46}Sc allows a dose rate decrease from the start to the end of the irradiation, therefore comparing the effects on the fibers by various dose rates. Also, photobleaching and photo-annealing the CC are the most common method to reduce the RIA occurring when a signal travels in the fiber [23], during the irradiation for the photobleaching and after irradiation for the photo-annealing. A comparison of those two methods is done to analyse the difference between their RIA and their gain recuperation. This will simulate the REDFs in function and passive form for the redundant REDFs in space missions.

To do so, four sets of seven selected REDFs are irradiated in different forms and doses to reach a dose of 60 krad in six months:

- 30 krad not in function (passive form) with the highest dose rate at the beginning of the irradiation from 0 to 30 krad
- 30 krad in passive form with a lower dose rate at the end of the irradiation from 30 to 60 krad
- 60 krad in passive form
- 60 krad in function along with the test (active form).

This test aims to analyse the optical gain of the REDFs under different doses, the effect of photobleaching, photo-annealing and the radiation sensitivity under different dose rates. This thesis focuses on creating the gamma-ray irradiator and irradiating four EDFs and three EYDFs.

The main constraint of this project is radioprotection. The test was designed to comply with the procedures in place for ensuring an annual radiation dose of laboratory personnel of 1 mSv. The work done to create this irradiator can be divided into four sub-objectives.

1. Mechanical design

   The first objective is to create the irradiator mechanical design fitting inside the laboratory cylindrical lead shielding. This setup, being the irradiator itself, contains the scandium source and the optical fibers for their irradiation.

2. Gamma irradiation modeling

   The modeling of the gamma irradiation distribution on the optical fibers according to the activity of the sources was developed in parallel with the mechanical design. It calculates the relative dose on the fibers and aims to optimize the configuration of the ^{46}Sc vials in the setup to obtain homogenous radiation.

3. Sources fabrication

   After the modeling giving the relative activity of each source, the ^{45}Sc must be activated into ^{46}Sc by neutron activation to obtain a total dose of 60 krad over six months' gamma-ray irradiation of the fibers.

4. Optoelectronic setup

   For the gamma-ray irradiation of the fibers, an optoelectronic setup needs to be designed and mounted in the laboratory to activate the set of optical fibers in active form and for their output power acquisition.

After the irradiation has been carried out, a preliminary presentation of the data is shown. It presents the data during irradiation under photobleaching, an example of photo-annealing after irradiation and a comparison of data for irradiation under the standard ^{60}Co and ^{46}Sc. More investigation of those data will be done afterwards in another work.

CHAPTER 2 LITERATURE REVIEW

2.1 Sources of Radiation in Space

Space is a harsh environment characterized by low radiation dose and dose rate from several types of radiation and strong thermal change, damaging the space mission devices. Space radiation brings up challenges in the development of space technologies intending to decrease the degradation of the ionizing radiation on the performance of devices in service for several years during their mission.

During a mission, the spacecraft undergoes different constraints and their effects on the components are shown in Figure 2.1.

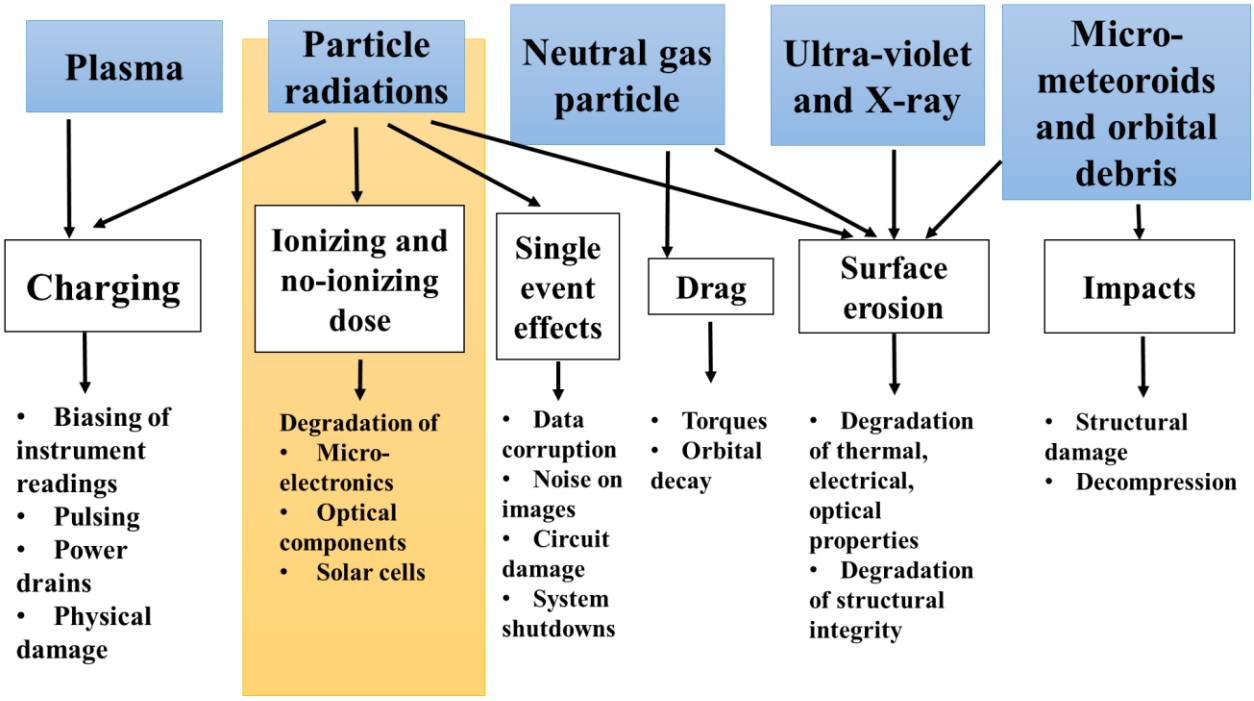

Figure 2.1 Different effects on the spacecraft components caused by the types of constraints in space. Taken from [24].

The main effect causing damage to the optical fibers is the particle radiations. The main ones are the solar particles, the trapped radiation in the Van Allen Belt and the Galactic Cosmic Rays.

2.1.1 Solar Particles

The solar particles are composed of electrons, energetic photons, heavy ions, and alpha particles with maximum energy up to the GeV. Three radiation categories can be defined as the Sun radiations: solar wind, solar flares and electromagnetic waves shown in Figure 2.2. The last one is non-ionizing and does not generate radiation damage. However, it increases the spacecraft system's temperature, affecting its performance. The solar flare produces an X-rays flare and an acceleration of proton to hundreds of MeV. The radiation from the Sun that affects the spacecraft is the plasma flow called the solar wind, coming from the outer part of the Sun corona, which consists mainly of a composition of hydrogen with a small component of helium and other ions. It is a continuous stream of ions caused by magnetic anomalies of the Sun. This ion flux is generally between 10^8 and 10^9 particles cm^{-2} s^{-1} measured at the periphery of the Earth's magnetosphere [25].

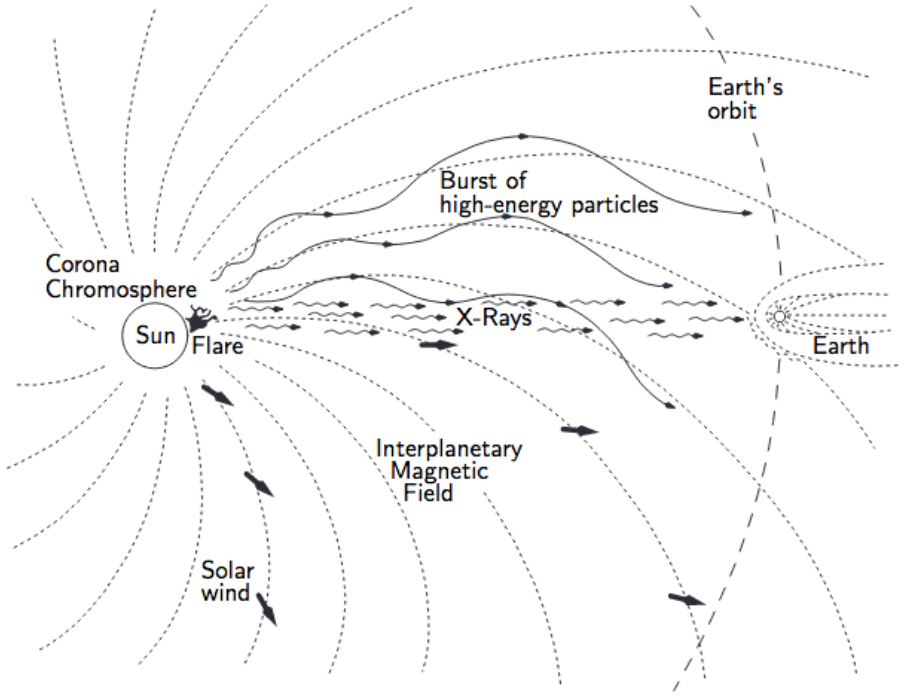

Figure 2.2 Propagation of the different radiation from the sun. Taken from [26].

2.1.2 Trapped Particles in Van Allen Belt

In 1958, Van Allen discovered the Earth-trapped radiation belts. The charged particles coming from outer space, mainly from the cosmic rays and solar wind, are trapped in the Earth's geomagnetic field. The inner belt primarily comprises energetic protons of a few hundred MeV, while the outer belt consists mainly of electrons with an energy of about 10 MeV. The particles move helically around the geomagnetic field lines between points near the south and the north poles. They are sliding along a magnetic line toward the pole, where the magnetic field increase, decreasing the particle's velocity, which can be reversed. That can make the particles reflect and bounce along the magnetic line between the two Earth's poles. Moreover, there is a longitudinal drift of the particles around the Earth. The protons drift to the west while the electrons drift to the east shown in Figure 2.3.

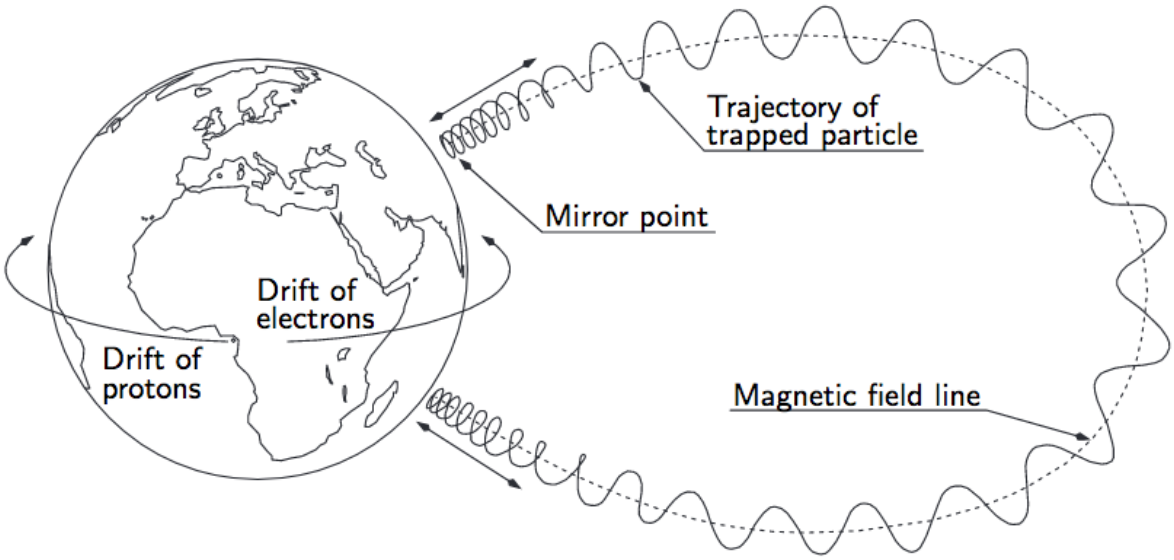

Figure 2.3 Trajectory of trapped particles trapped in the geomagnetic field with the bounce and the drift. Taken from [26].

The South Atlantic Anomaly (SAA) is the region where the inner belt reaches its lowest altitude. This anomaly is caused by the non-symmetric geomagnetic around the Earth. The axis of the geomagnetic field is tilted 11° from the Earth’s rotational axis. A consequence of this is trapped particles in the inner belt at a low altitude near the south Atlantic Ocean. That leads to an increased

proton flux in this area, exposing the space system travelling at low orbit to an essential radiation source.

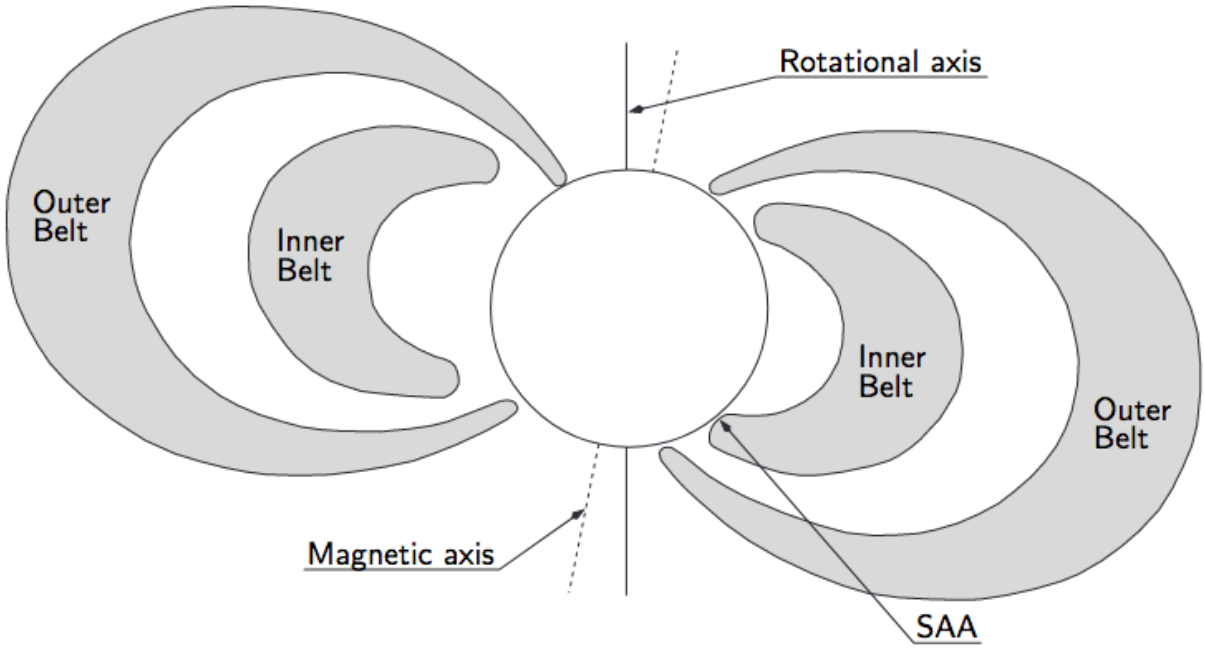

Figure 2.4 Van Allen belts with the magnetic axis and the South Atlantic Anomaly. Taken from [26].

2.1.3 Galactic Cosmic Rays

The Galactic Cosmic Rays (GCR) come primarily from outside the solar system with energy up to the TeV. The dominant part is of galactic origin, mostly from our Milky way galaxy, and a small amount of it is coming from the sun. The GCR flux consists of 90% protons, 9% alpha particles and 1% ions accelerated, probably by the magnetic field of supernova remnants, to near the speed of light.

The GCR is the dominant source of radiation for space missions. Having high energy, those heavy particles can penetrate spacecraft and shielding against those rays are very difficult.

2.2 Application of REDFAs in Space

In spacecraft, various fiber-based applications are thriving technology due to their reliability. NASA has never reported any optical fibers failures on board for transmission links after using them for more than 30 years [27]. This device has various potential in many different applications for space technologies [28-30] :

- Telecom and transponders.
- Light detection and ranging (LIDAR) and differential absorption LIDARS (DIAL). Those technologies used lasers to probe atmospheric properties. It can characterise the Earth's magnetic field, CO2, wind detection, water vapor, and volcanic activities.
- Altimetry for altitude measurement in spacecraft and Earth and planetary mapping.
- Spectroscopy; to analyse the composition of planets or a space body using Raman spectroscopy and laser-induced breakdown spectroscopy (LIBS).
- Fiber optical gyroscope (FOG) using the Sagnac effect to monitor the angular velocity and the orientation.
- Automated planetary rovers for diverse applications.

Therefore, this study targets the applications in space of the telecommunication devices.

2.2.1 Telecommunication in space

Before photonic technologies arrived in space, data transmission was principally made using radio communication. New space data acquisition technologies, such as microphones, spectrometers and high-resolution cameras in satellites, rovers and other space devices, are acquiring increasingly large data sets. They required fast data processing and communication, especially for photo and video transmission. Those need to be sent to Earth control or paired devices, and with the minimum possible delay, for example when decisions on Earth need to be taken after the transmission of information from a Martian rover. However, the limit in data rate transmitted per second has been reached, making it impossible to transmit data efficiently with all the new devices.

The EDFA has high data rates of up to 10 $\mathrm{Gb} \cdot \mathrm{s}^{-1}$ in the 1550 nm band, making him a good candidate for space telecommunication [29]. REDFAs are used to amplify the signal as a receiver and a transmitter in free space optic (FSO) telecommunication and are used for inter-satellite communication between low earth orbit (LEO) satellites and geostationary equatorial orbit (GEO) satellites, between LEO-LEO satellites and satellite-to-ground communication.

2.3 Principle of an Optical Amplifier

The optical amplifiers use the spectroscopy advantages of the RE ions located in the core of the doped fiber to amplify the signal. The first energy levels for the common optical fibers doped with erbium are shown in Figure 2.5. This figure also shows the absorption wavelength between certain excited-state. Every energy level can be excited and have its own lifetime, significantly affected by the glass composition. The Er^{3+} energy level that has the longest lifetime is the $^4I_{13/2}$ metastable state and has various lifetimes for various hosts shown in Table 2.1. It can be seen in this table that this energy level's lifetime can vary from 4 ms to 14 ms with different glass hosts.

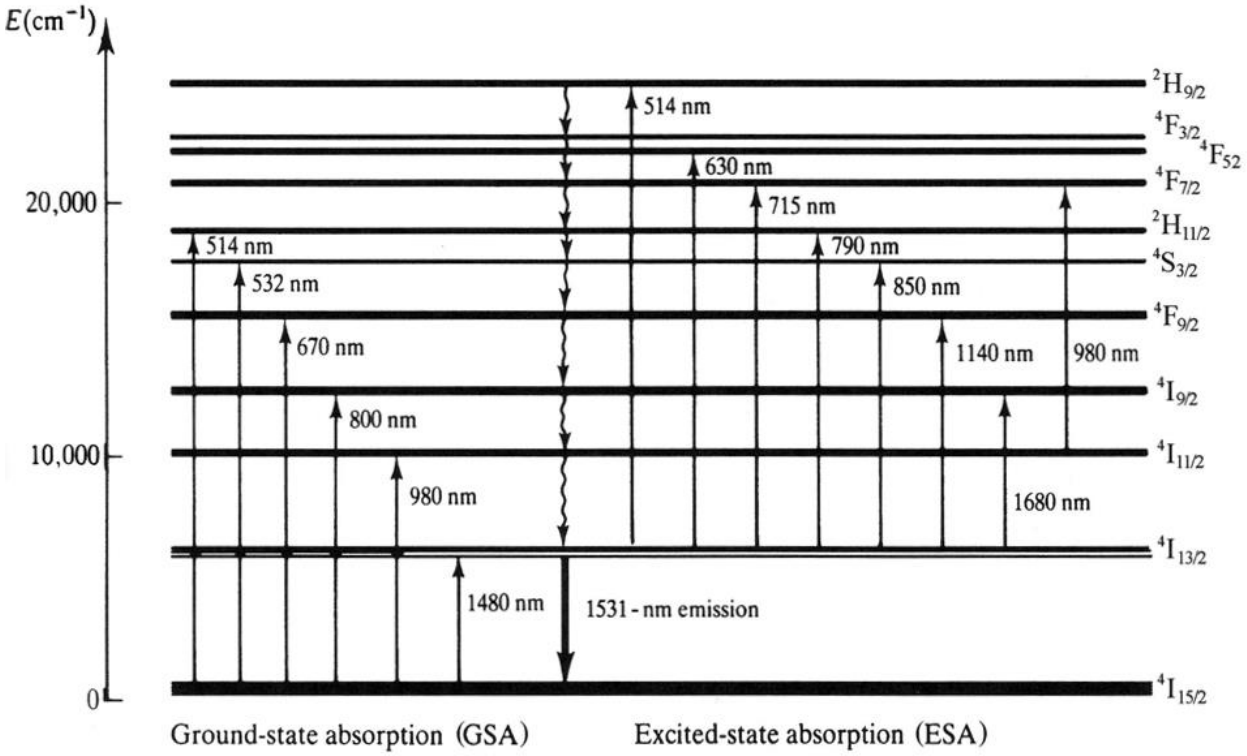

Figure 2.5 Energy level of Er^{3+} with the absorption wavelength from the ground-state absorption and the excited-state absorption of the $^4I_{13/2}$ and $^4I_{11/2}$ metastable states. Taken from [31].

Table 2.1 Lifetime of the $^4I_{13/2}$ metastable state of Er^{3+} in various glass hosts. Taken from [32].

Host Glass	Lifetime (ms)
Na-K-Ba-silicate	14
ED-2 (silicate)	12
Silicate	14.7
Silicate L-22	14.5
Al-P silica	10.8
Al-Ge silica	9.5-10.0
Na-Mg-phosphate	8.2
LGS-E (phosphate)	7.7
LGS-E7 (phosphate)	7.9
Phosphate	8.5-10.7
Fluorophosphate	8.0
Fluorophospahte L11	8.25
Fluorophospahte L14	9.5
Ba-La-borate	8.0
Na-K-Ba-Al-germanate	6.5
Fluoride	10.3
Fluorozirconate F88	9.4
Tellurite	4

The EDF amplifier exploits the $^4I_{13/2}$ energy level lifetime, which is long enough to create a population inversion. By pumping the EDF at 980 nm, erbium ions are excited from the ground state to the $^4I_{11/2}$ excited state of a short lifetime. From there, ions are almost immediately relaxed, by radiation heat, to the $^4I_{13/2}$ excited state. With sufficient pump power and the appropriate wavelength launched in the fiber, the population inversion is achieved between the ground state and the $^4I_{13/2}$ excited state. It is also possible to pump the erbium at 1480 nm. At this wavelength, the ions are excited directly from the ground state to the $^4I_{13/2}$ excited state, where population inversion can be achieved. This population inversion, the basic principle of the amplifier, creates an amplification by stimulated emission with the laser signal injected into the fiber at around 1550 nm, as shown in Figure 2.6.

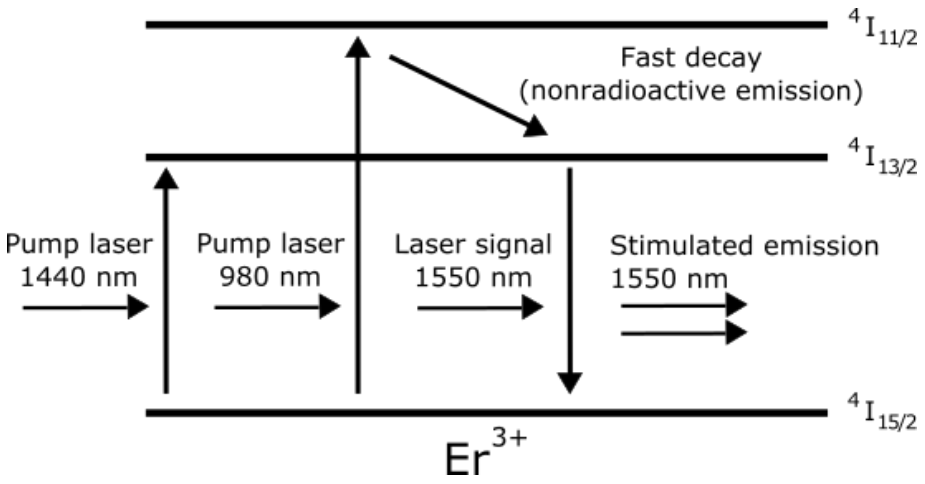

Figure 2.6 Mechanism of the population inversion of Er^{3+} with absorption at 980 nm and 1440 nm with the stimulated emission by the laser signal.

The amplifiers using EYDF are usually high-power amplifiers by pumping in the fiber cladding. This fiber is co-doped with Er^{3+} and Yb^{3+}, where the latter is used to increase the absorption of ions by its high absorption cross-section. That is necessary first because a higher erbium doping level leads to a low amplifier efficiency caused by increased interactions of erbium ions pair. In contrast, higher ytterbium doping does not have this problem. Secondly, the cladding pumping configuration has the disadvantage of a low overlap between the core and the pump light, decreasing the absorption [33].

EYDF amplification is based on the population inversion on the energy level $^4I_{13/2}$ of the erbium ions. To do so, a pump signal between 900 and 980 nm excites the ions of the Yb^{3+} from its ground state $^2F_{7/2}$ to the excited state $^2F_{5/2}$. From there, the excited Yb^{3+} ions transfer their energy to the Er^{3+} ions raising them to the excited state $^4I_{11/2}$. From there, the same process of the EDF amplification occurs with the population inversion on the $^4I_{13/2}$ excited state and the stimulated emission creating the amplification of the laser signal, as shown in Figure 2.7.

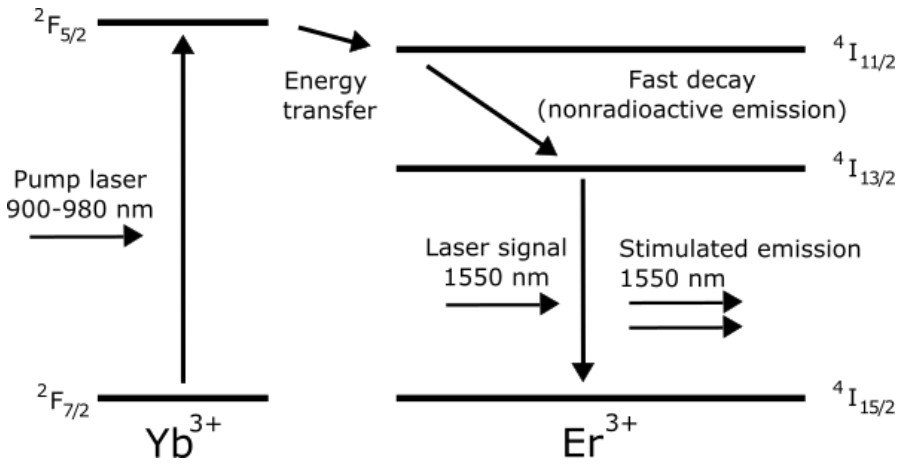

Figure 2.7 Energy diagram of EYDF and its amplification mechanism. It starts with the absorption from 900 to 980 nm of the Yb^{3+} ions to their energy transfer to the Er^{3+} ions. That follows by non-radiation decay to the $^4I_{13/2}$ state to the stimulated emission.

A common amplifier is constructed using different components as shown in Figure 2.8. The signal is amplified by stimulated emission in the REDF with the pump source achieving the population inversion, which is the main mechanism of the amplifier. Amplifiers have three main configurations: the active fiber can be configured in forward pumping when the laser diode wave travels in the same direction as the signal wave shown in Figure 2.8 a); in backward pumping when the laser diode wave travels in the opposite direction of the signal wave shown in Figure 2.8 b); or in bidirectional pumping shown in Figure 2.8 c). The other components are used for ensuring the proper functioning of the amplifier. The wavelength division multiplexing (WDM) coupler is to inject the input signal and the pump light together in the REDF and the isolators are to stabilise the signal amplification by eliminating back reflection and are also used to protect components.

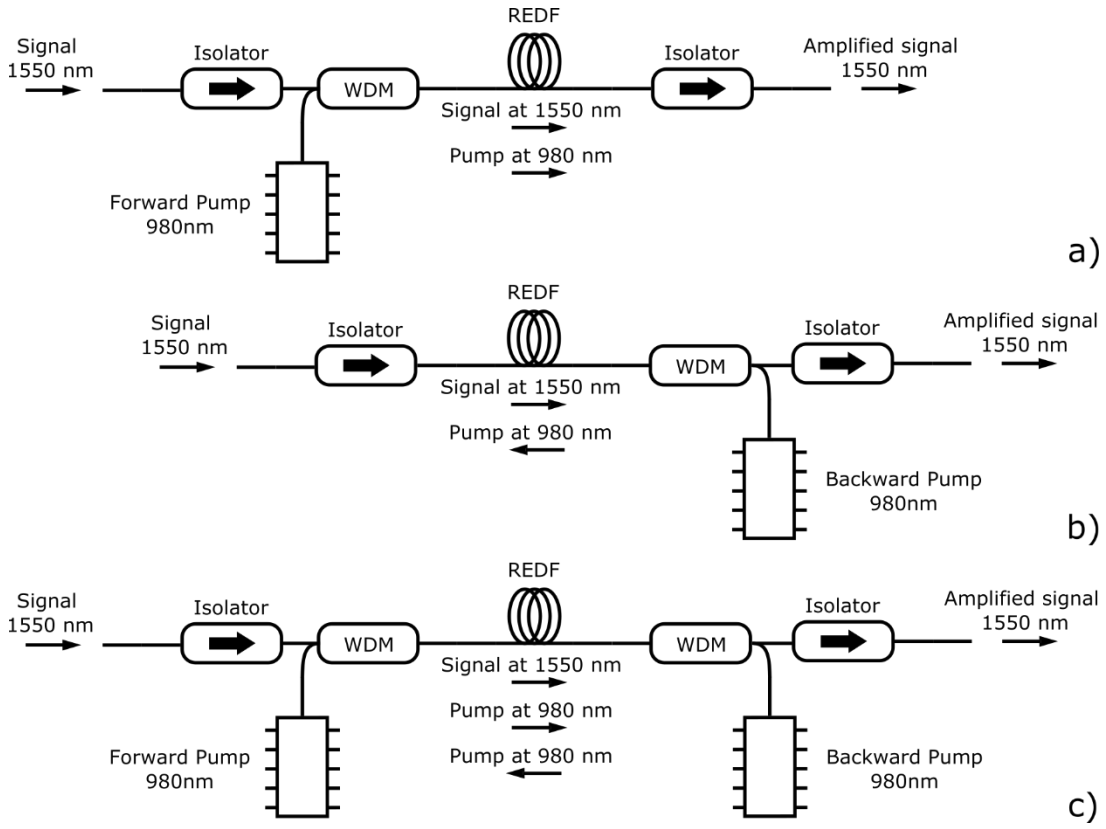

Figure 2.8 Schematic setup of a REDFA design, (a) with a forward pumping configuration, (b) with a backward pumping configuration, and (c) with a bidirectional pumping configuration.

2.4 Radiation effects on rare earth doped optical fibers

When optical fibers are exposed to radiation, their transmission properties are deteriorated, especially for the REDFs. The main effect caused by the REDFs is the RIA which is increasing with the dose rate accumulation.

The creation of CC causes the RIA of optical fibers, also called point defects. This phenomenon is the release of electrons and holes during irradiation, getting trapped in the defects of the amorphous silica network that were pre-existing before irradiation or being created during irradiation. Their generation rates and optical properties rely on parameters such as the fiber composition, manufacturing process and irradiation condition [34].

Previous studies have proved that the REDFs are very sensitive to radiation, making them the major limiting component in the telecommunication systems used in space [13, 16]. Their high sensibility to radiations is at the origin of the composition of the host matrix, mostly co-doped with aluminium or phosphorus. The erbium or/and ytterbium dopant concentration in the fibers weakly affects the RIA response, caused mainly by the aluminum and phosphorus defects [21, 35, 36].

2.4.1 Color center bleaching and annealing

The effect of the RIA on the fiber's transmission can be reduced by methods such as bleaching and annealing. During irradiation, fibers in the active form go through photobleaching. In this case, the creation of point defects in the fibers is influenced by two counter mechanisms, the CC mechanism and the photobleaching. The last one allows for decreasing the point defects during their creation by radiation [23]. In this case, the dose rate for the same total dose is an essential factor, slowing down or increasing the speed of the point defects mechanism going against the photobleaching. When the dose rate is slower, the photobleaching has a stronger influence than a fast one for the same total dose because the irradiation is done at a slower pace, giving more time for recovery by the photobleaching. After the irradiation, by injecting a signal inside the fiber the photo-annealing mechanism can be used to anneal the point defects produced during irradiation. The efficiency of these mechanisms depends on the core composition, the fiber dimension and length, the signal wavelength with its injection power and the pumping configuration [10, 15].

Another mechanism used to recover the transmission proprieties is thermal annealing. This occurs when the irradiated fiber is exposed to a high temperature, resulting in its efficiency increasing with the temperature. The temperature needs to be above 250°C for a significant recovery [37].

2.4.2 Effect of the dose rate on the radiation induced attenuation

In the literature, there is a controversy on the effect of the dose rate on the RIA for REDFs. Various studies showed that a higher dose rate induces a lower RIA [11, 19, 20], while others declare that a lower dose rate induces a lower RIA [17, 18, 21]. This disagreement is an important point to investigate for the understanding and prediction of the performance of the optical system for long-term space missions. Consequently, accelerated irradiation tests at a high dose rate may not be sufficient to predict REDFs degradation in a low dose rate environment like in space.

In the investigation made by Thomas *et al.* [20], tests exhibited an enhanced low-dose-rate sensitivity (ELDRS) to radiations. All of their tests have shown increasing RIA with a decreasing dose rate. The range is between 50 rad/h to 1200 rad/h using the wavelength of interest for telecommunication, 980 nm and 1550 nm, shown in Figure 2.9. The test was performed on EDFs without photobleaching during irradiation and using a switching-dose rate method.

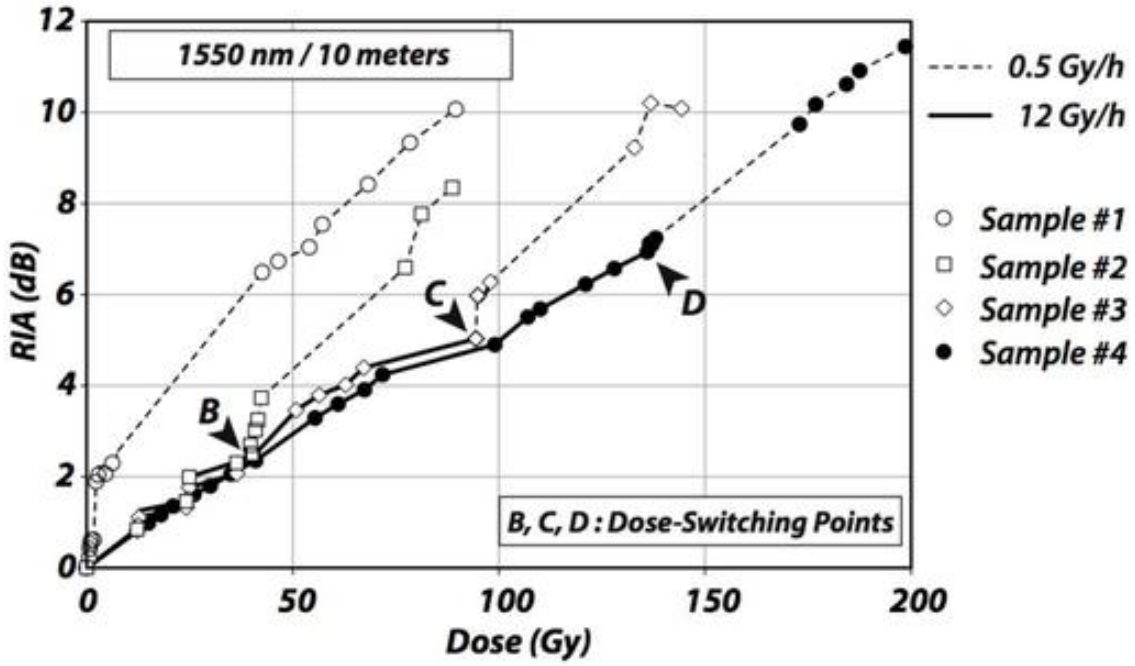

Figure 2.9 Test result of the RIA as a function of the total dose for four EDFs samples at 1550 nm with the switching-dose rate method performed by Thomas *et al.*. Sample #1 was irradiated at the low dose rate of 50 rad/h while the others were switched from the high dose rate of 1200 rad/h to the low dose rate at the respective point B, C and D. Taken from [20].

In another experiment by Fox *et al.* [11], the RIA increases with a lower dose rate. In this study, EDFs were under irradiation with dose rates of 32 040 rad/h, 53 280 rad/h and 109 440 rad/h. The RIA for the different dose rates has been studied for the spectrum in the near-infrared for a total dose of 0.4 krad, 2.6 krad and 8.5 krad, shown in Figure 2.10.

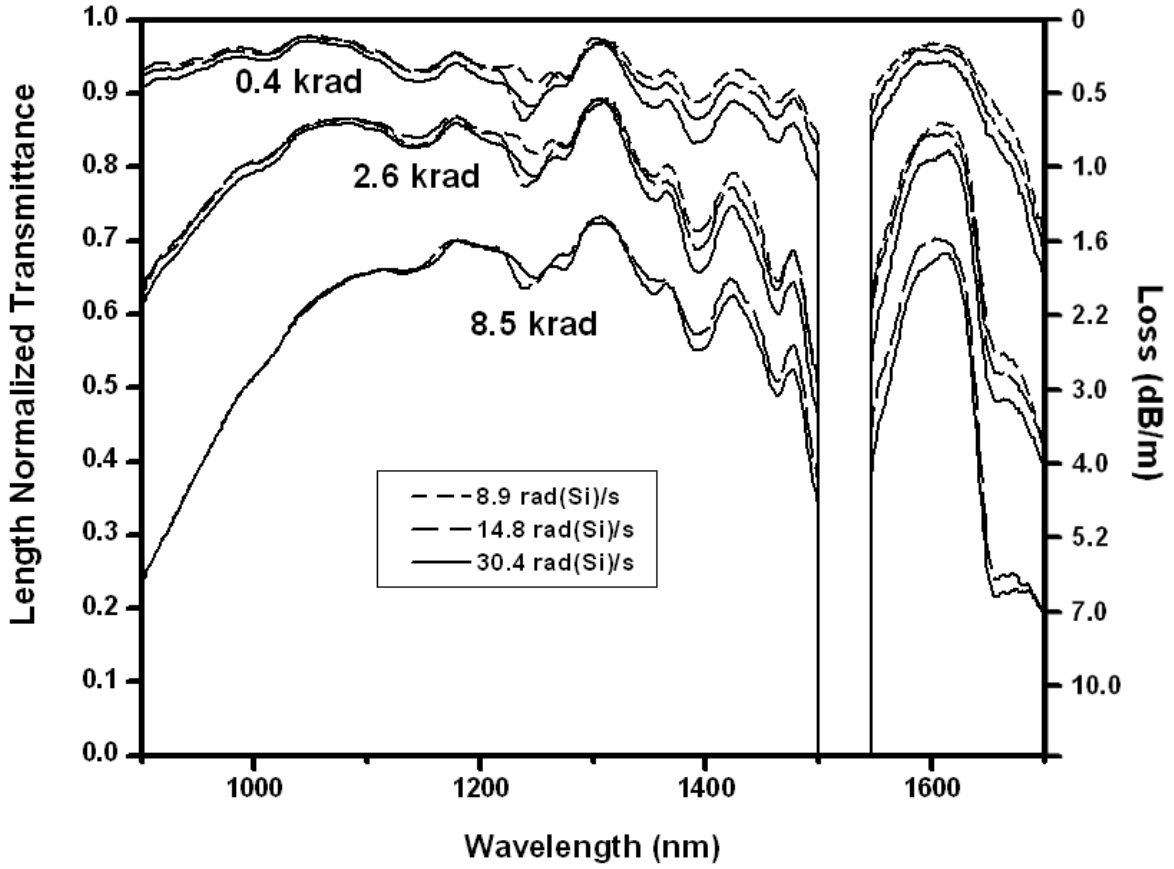

Figure 2.10 Test result of the RIA as a function of the wavelength for different dose rates and doses done by Fox *et al.* and taken from[11].

Those results show that loss of gain increases with a lower dose rate and that some regions of the spectrum are more sensitive to the dose rate.

While the results of the previous experiments showed an increasing RIA with decreasing dose rate, others came to the opposite conclusion. In one paper by William *et al.* [17], two EDFs were irradiated for a total dose of 145 krad with respective dose rates of 3000 rad/h, 64 980 rad/h and 1 218 000 rad/h. The loss as a function of the dose rate for different signal wavelengths is shown in Figure 2.11

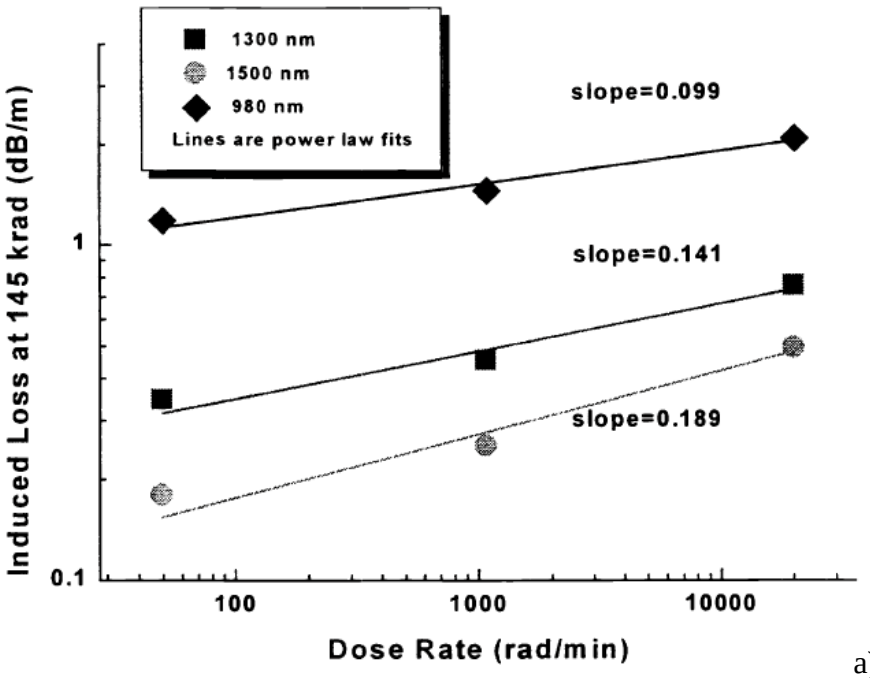

a)

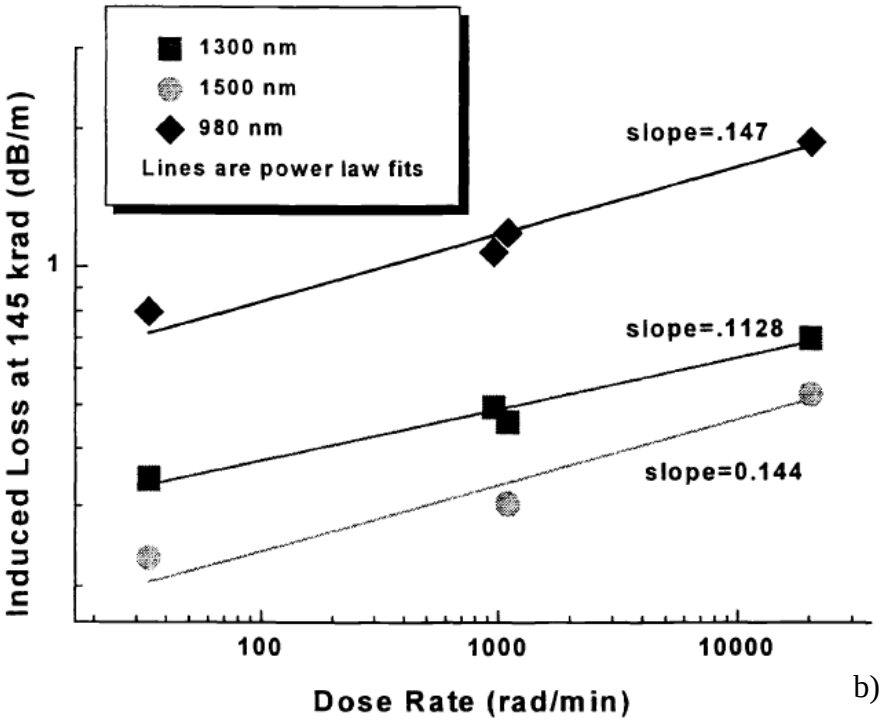

b)

Figure 2.11 Test result of the loss at 145 krad as a function of dose rate for different wavelengths for (a) the first EDF fiber and (b) the second EDF fiber done by Williams *et al.* and taken from [17].

Those results show the loss caused by the RIA increasing with the dose rate.

Another experiment was conducted by Ahrens *et al.* [18] irradiated an EYDF at dose rates of 12 600 rad/h, 100 rad/h, 50 rad/h and 20 rad/h. Significant differences in radiation responses were observed for various dose rate irradiations for a transmission signal of 1310 nm. For a total dose of 16 krad, the irradiation on the fiber induced loss of 0.27 dB/m at 12 600 rad/h, 0.09 dB/m at 100 rad/h for 15 krad and around 0.09 dB/m for 50 and 20 rad/h as shown in Figure 2.12.

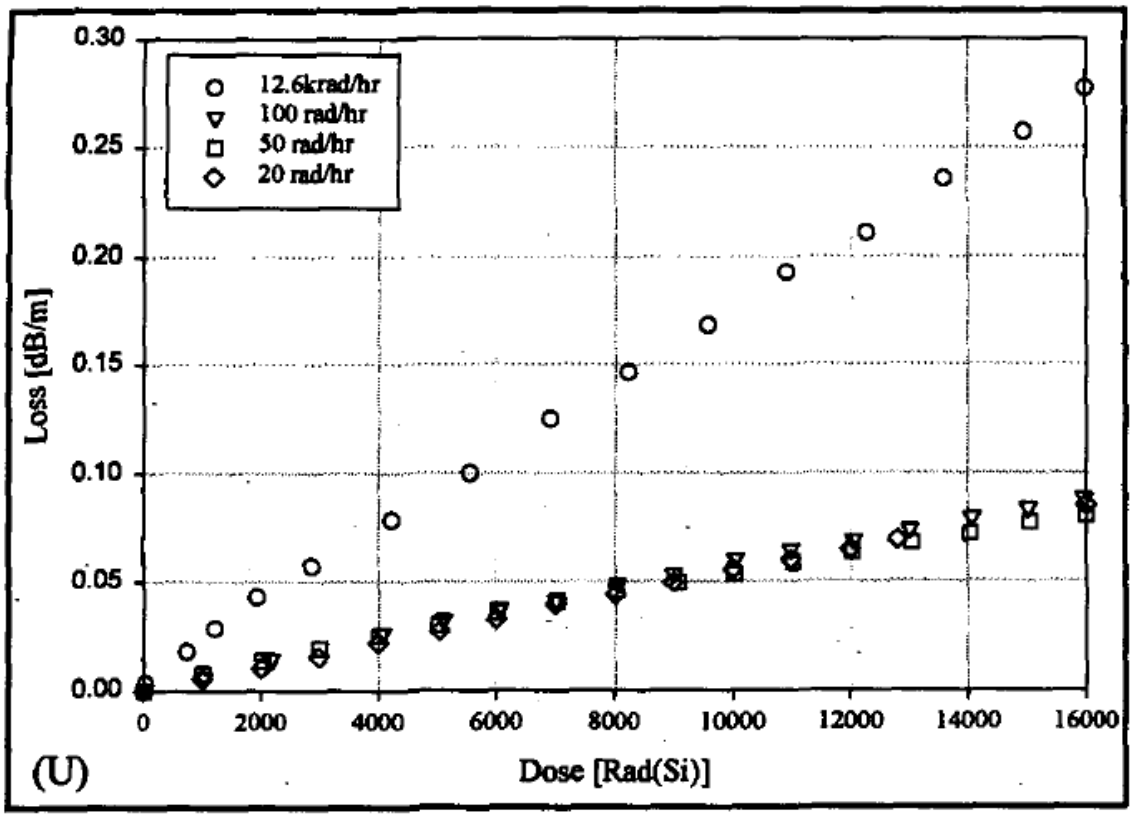

Figure 2.12 Test result of the loss as a function of dose for different dose rates for an EYDF after exposure to 16 krad at 1310 nm done by Ahrens *et al.* and taken from [18].

In this experiment, irradiating an EYDF, the loss increases with the dose rate.

Friebele *et al.* irradiated various EDFs co-doped with Al_2O_3 and studied the effect of the dose, dose rate, photobleaching and photo-annealing [21]. In one test, one fiber was irradiated for a total dose of 3 krad with a dose rate of 50 rad/h and 50 000 rad/h. Both fibers were active for a total time of 12 hours, undergoing photobleaching and photo-annealing. The fiber with the lowest dose rate lost 0.4 dB/m less than the one with a higher dose rate. This experiment demonstrated that a higher dose rate increases the loss caused by the RIA.

In Brichard *et al.* [19] research, EDFs were irradiated at different dose rates. Those fibers were made without co-dopant such as aluminium or phosphorus. They are usually used to improve the solubility of the erbium in the glass but contribute to the RIA. The wavelength used for this test was 980 nm and 1590 nm with dose rates of 45 rad/h, 450 rad/h and 4500 rad/h. The result shows a higher RIA for a lower dose rate shown in Figure 2.13 a), c), d) and a lower RIA for a lower dose rate in Figure 2.13 b).

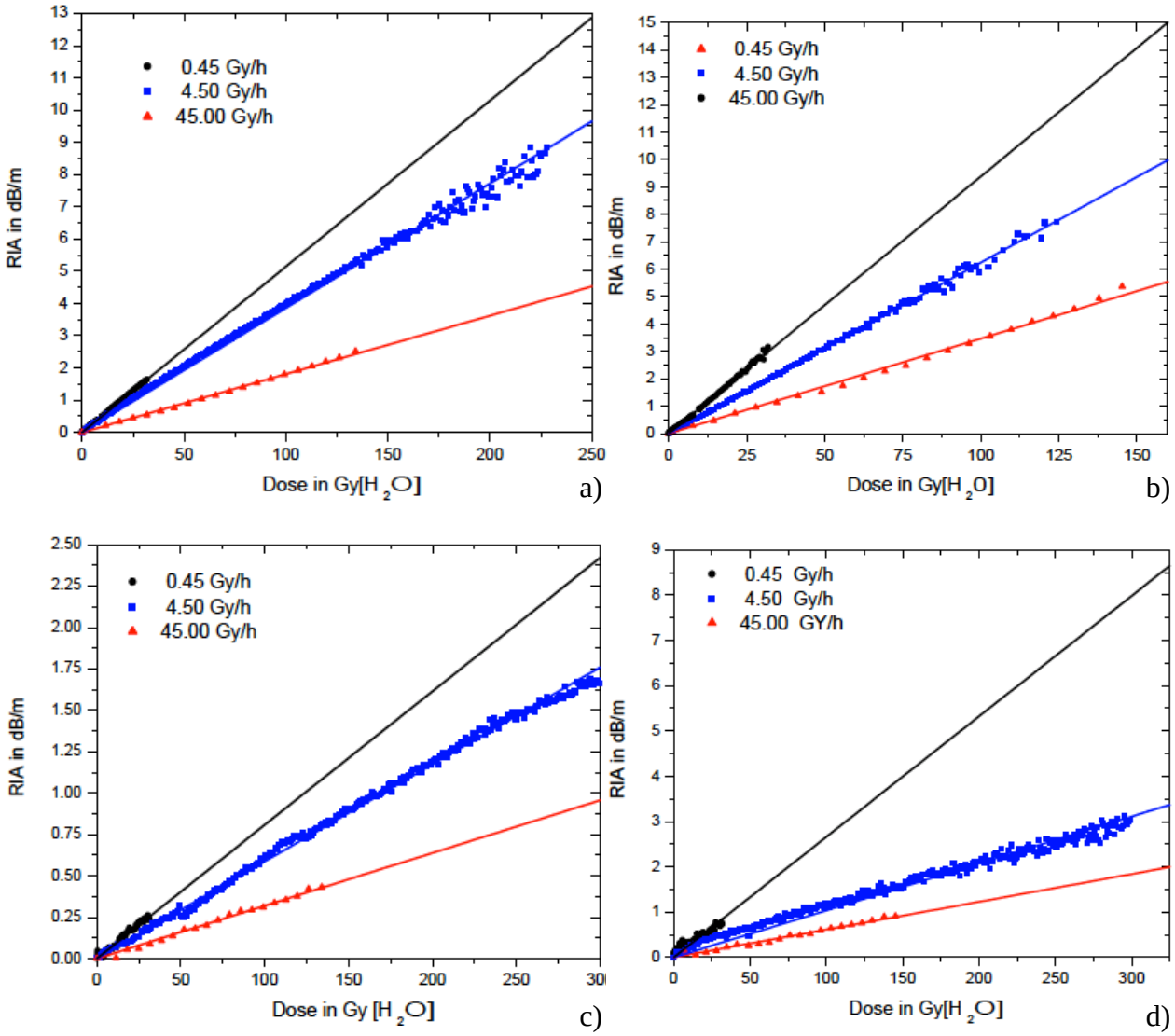

Figure 2.13 Test result of the RIA as a function of the total dose for two different EDFs without co-dopant at 980 nm for a) fiber #1, b) fiber #2, and at 1590 nm for c) fiber #1, d) fiber #2 from the test perform by Brichard *et al.* Taken from[19].

In those data, fiber #2 was activated at 960 nm with a higher RIA for a higher dose rate while for the same fiber activated at 1590nm, the RIA was higher with a lower dose rate. This test demonstrated the opposite effects on the same fiber activated at a different wavelength.

Various tests carried out by different groups showed different results. The paper published by Gilard *et al.* [12] works on that controversy and has proposed a theoretical framework to explain the dose rate dependence on the RIA. This theory assumes that only two antagonistic mechanisms influence RIA growth, the generation of CC and their annihilation at a constant rate over time. This development relies on two approximations, the first being that the CC is the single dominant effect responsible for the RIA and the second one being that radiation induced defect created in the fiber is negligible compared with the one pre-existing in the fiber. They concluded that certain fibers exhibit ELDRS under a dose rate threshold shown in Figure 2.14. This threshold depends on parameters such as the dose rate, the dose, the CC density, and the trapped carrier's decay time.

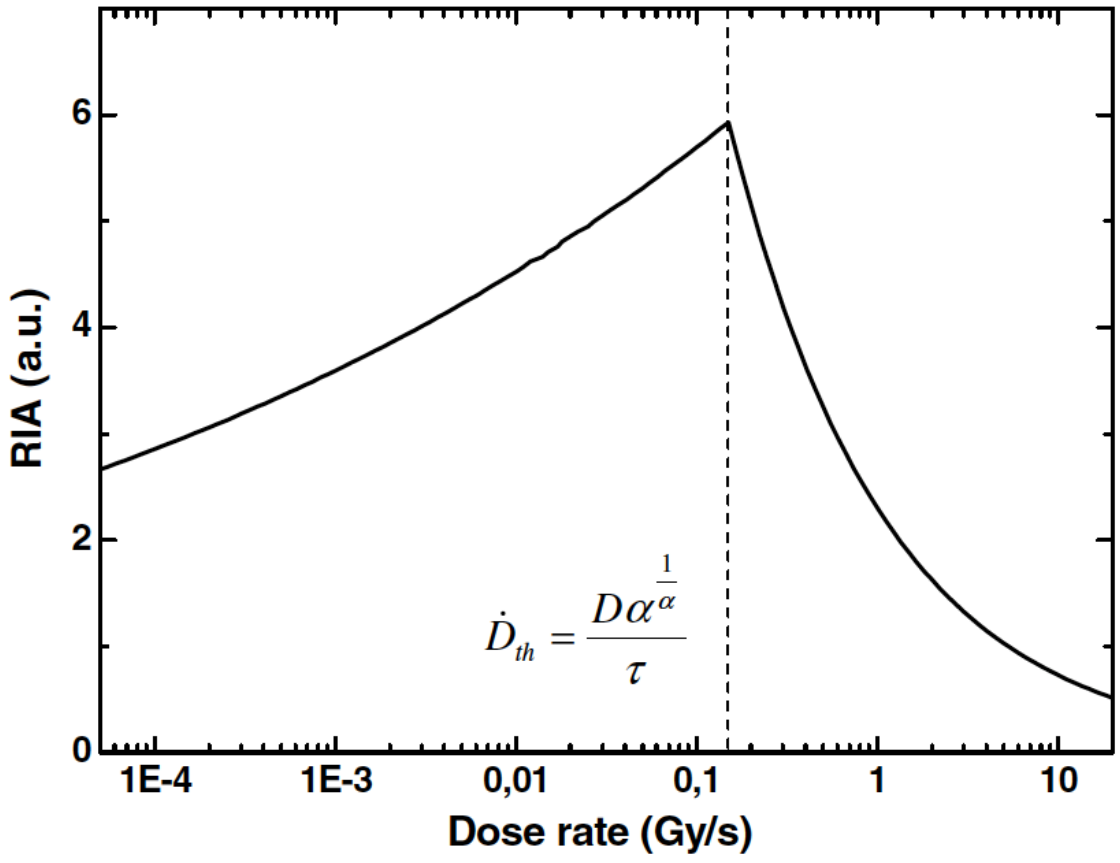

Figure 2.14 Threshold showing the dose rate where the ELDRS effect appears from the theoretical framework for a specific fiber developed by Gilard *et al.* and taken from [12].

Over that threshold, the RIA decreases with increasing dose rate, and the ELDRS effect appears above that threshold. This theory can explain the controversy in the results obtained in the different research. However, the effects of the ELDRS are not detected in the optical system in service in space exposed to a low dose rate [22]. More investigations need to be done on the effect of the dose rate on the RIA to understand its mechanism. That will improve irradiation testing of REDFs for harsh environments like space, leading to improved optical systems for these environments.

2.5 Basics Radiation Concepts

2.5.1 Radiation

Radiation is energy transmitted or emitted in the form of waves or particles through space or a material medium. Radiation can be divided into two main categories according to its energy. The first one is the ionizing radiation with higher energy than the second one, the non-ionizing radiation. Ionizing radiation is so-called because its energy can break electrons away from an atom. The radiation intensity can be approximated by defining the source of ionizing radiation by point sources. A point source represents a point in space whose intensity follows the inverse square law:

$$intensity \propto \frac{1}{distance^2}. \tag{2.1}$$

2.5.2 Radioactivity

Radioactivity is the process of an unstable atomic nucleus spontaneously transforming by decay into another element. This modification of the atomic structure generates emissions of radiation:

$$X \rightarrow Y + a_1 + a_2 + \cdots + a_n. \tag{2.2}$$

A material containing unstable atomic nuclei is defined as radioactive. The unstable atomic nucleus, called radionuclides or radioisotopes, exists naturally or can be created artificially with a nuclear reactor or particle accelerator.

The radioactive decay of the radionuclide is a stochastic event for a single atom. However, the probability of decay per unit of time for the number of atoms N is constant and defined by the activity A:

$$A = -\frac{dN}{dt} = \lambda N. \tag{2.3}$$

The decay constant λ, expressed as a half-life $t_{1/2}$ is used to define the activity:

$$\lambda = \frac{\ln (2)}{t_{1/2}}. \tag{2.4}$$

With the decay constant and the initial quantity of atoms N_0, the atoms that remain and did not decay $N(t)$ after a time t can be found following:

$$N(t) = N_0 e^{-\lambda t}. \tag{2.5}$$

This decay is characterized by the emission of alpha α particles, beta β particles or gamma γ radiation.

2.5.3 Alpha-Ray

The alpha-ray α occurs when a heavy nucleus decays and ejects an alpha particle. The alpha particle is the nucleus of the helium atom ($^4_2$He), being a heavy particle and can be stopped with a sheet of paper:

$$^A_Z X \rightarrow {}^{A-2}_{Z-2}X + \alpha(^4_2\text{He}). \tag{2.6}$$

The α particle is charged, made of two neutrons and two protons bound together. This particle is created during an alpha decay, involving only heavy nuclei with an excess of protons, generally when $Z > 82$ and $A > 200$. After the decay, the daughter nucleus has two fewer neutrons and protons than the parent nucleus. The energy of the alpha particle will be the same if it decays from the same nucleus and is more ionizing than the beta particles and gamma-rays.

2.5.4 Beta-Ray

The β particle corresponds to a negatively charged electron β^- or a positively charged positron β^+ emitted during the beta decay of a nucleus.

The β^-decay occurs when a neutron converts into a proton p, an electron e^- and an antineutrino $\bar{\nu}_e$:

$$n \rightarrow p + e^{-} + \bar{\nu}_e. \tag{2.7}$$

Where the generic equation of the β^{-}decay is:

$$^{A}_{Z}X \rightarrow {}_{Z+1}{}^{A}Y + e^{-} + \bar{\nu}_e. \tag{2.8}$$

The β^{+}decay occurs when a proton converts into a neutron n, a positron e^{+} and a neutrino ν_e:

$$p \rightarrow n + e^{+} + \nu_e. \tag{2.9}$$

Where the generic equation of the β^{+} decay is:

$$^{A}_{Z}X \rightarrow {}_{Z-1}{}^{A}Y + e^{+} + \nu_e. \tag{2.10}$$

Beta particles are less ionizing than alpha particles but are more penetrating, requiring an aluminum paper of a few centimetres to block the particles. They can interact easily with matter caused by their property of being charged.

2.5.5 Gamma-Ray

A gamma-ray γ is an electromagnetic wave-like visible light but more energetic. It consists of the shortest electromagnetic wave spectrum wavelength and the most energetic photon. This massless particle is not charged and has a high penetration property, interacting less with the matter. Gamma-ray emission occurs during a gamma decay, generally after an alpha or beta decay, leaving the daughter nucleus in an excited state. The energy emitted by the photons is the difference between the two transition levels of the nucleus. To attenuate the gamma-ray for radioprotection purposes, the shielding needs to be a dense material with a high atomic number Z as concrete or lead. Typically, gamma-ray shielding material is defined by the half-value layer (HVL), the thickness of absorber material needed to reduce the intensity of incident radiation by a factor of two.

2.5.6 Cross Section

The cross section determines the probability of interaction between an incident particle like a neutron or gamma-ray and a target object for an effective area.

The neutron cross section is used to characterize the nuclear reaction rate being the number of reactions per second. Furthermore, this rate is proportional to the incident neutron flux ϕ and depends on the energy of the incident neutron, the type of nuclear reaction occurring, the nuclear proprieties of the nucleus and the target size.

The probability of interaction between an incident neutron beam and the effective target area of a single nucleus is defined as the microscopic cross section σ_x of the nuclear reaction of type x, express in barns (1 barn = 10^{-24} cm^2). This cross section does not rely on the dimension of the actual target, while the macroscopic cross section Σ does. The last one represents the effective target area of every nucleus in the volume of the target, expressed in cm^{-1}. The macroscopic cross section is derived from the atomic number density N in $\mathrm{nuclei/m^3}$ and the microscopic cross section:

$$\Sigma = N\sigma_x. \tag{2.11}$$

In the case of the material composing the target is a mixture of different types i of nuclides, the macroscopic cross section is:

$$\Sigma_x = \sum_i N_i \sigma_{i,x}\ . \tag{2.12}$$

To calculate the macroscopic cross section, the microscopic cross section for the interactions with a single isotope are available in a data library such as ENDF/B-VIII.0.

2.6 Irradiation of the Sources

2.6.1 Neutron Activation

Neutron activation is the process of inducing radioactivity in materials with a neutron flux. That occurs when a material is exposed to neutron flux, and its nuclei capture free neutrons. The combination of the incident neutron and the target nucleus increases the atomic mass of the nucleus and forms a compound nucleus.

If the incident neutron targets the target nucleus ${}^{A}_{Z}X$, where X is the chemical symbol of the element, A the atomic mass number and Z the atomic number, the reaction is:

$$ {}^{A}_{Z}X + {}^{1}_{0}n \rightarrow ({}^{A+1}_{Z}X)^{*}. \tag{2.13} $$

The compound nucleus being excited nuclei, highly unstable, decay immediately by emitting a neutron, particles such as particles alpha, particles beta and protons or a gamma-ray leading to a radiative capture (n, γ). When a radiative capture occurs, the nuclide form is unstable, even after an intermediate decay and becomes radioactive. The period of radioactivity can vary from a fraction of a second to years.

The reaction of a radiative capture is expressed as:

$$ {}^{A}_{Z}X + {}^{1}_{0}n \rightarrow ({}^{A+1}_{Z}X)^{*} + \gamma. \tag{2.14} $$

It can also be written in its short form:

$$ {}^{A}_{Z}X(n, \gamma)^{A+1}_{Z}X. \tag{2.15} $$

This is the reaction of the radiative capture of the ^{45}Sc, used in this project. This element was irradiated with a neutron flux in the SLOWPOKE-2 nuclear reactor:

$$ {}^{45}_{21}\mathrm{Sc} + n \rightarrow ({}^{46}_{21}\mathrm{Sc})^{*} + \gamma. \tag{2.16} $$

2.6.2 Induced Activity in the Sample

The formation of radioisotopes causes the activity induced in a sample. The number N^* of radioisotopes $({}^{A+1}_{Z}X)^*$ formed during irradiation for a time dt is proportional to the stable atoms of the target sample N_0, the incident neutron flux ϕ $(\mathrm{n}\cdot\mathrm{cm}^{-2}\cdot\mathrm{s}^{-1})$ and the cross section of the radiative capture $\sigma_{n,\gamma}$ (cm^2):

$$N^* = N_0\sigma_{n,\gamma}\ \phi dt. \tag{2.17}$$

At the same time as the formation of radioisotopes N^*, the number N of their disintegration for a given isotope present at time t is:

$$N = N^*(t)\lambda dt, \tag{2.18}$$

where λ is the constant of disintegration of the radioisotope N^* (s^{-1}) present in Equation (2.4).

The radioisotopes growth rate in the target material at the time t is given by:

$$dN = N^* - N = \left(N_0\sigma_{n,\gamma}\ \phi - N^*(t)\lambda\right)dt. \tag{2.19}$$

By integrating the last equation and assuming that $N^*(0) = 0$, we obtain the number of radioactive atoms formed for an irradiation time t_i:

$$N^*(t_i) = \frac{N_0\sigma_{n,\gamma}\ \phi}{\lambda}\left(1 - e^{-\lambda t_i}\right). \tag{2.20}$$

The induced activity, expressed in Bq (decay/s), is obtained by multiplying λ by the last equation:

$$A(t) = \lambda N^*(t) = N_0\sigma_{n,\gamma}\ \phi\left(1 - e^{-\lambda t}\right). \tag{2.21}$$

It is better to express this equation as a function of the mass of the sample since the mass of the sample is known. At $t = 0$, the number of nuclei in the sample follows:

$$N_0 = \frac{N_A m\theta}{M_a}. \tag{2.22}$$

To obtain the induced activity as a function of the mass:

$$A(t_i) = \frac{N_A m \theta \sigma_{n,\gamma}\ \phi}{M_a}\left(1 - e^{-\lambda t_i}\right), \tag{2.23}$$

where N_A is the Avogadro constant, m the target element's mass (g), θ the target isotope's abundance in the element and M_a the irradiated isotope's atomic mass.

The induced activity of the samples will decrease between the end of its irradiation and the start of the gamma irradiation of the fibers. Then the induced activity after a time t_d of radioactive decay is:

$$A(t_i, t_d) = \frac{N_A m \theta \sigma_{n,\gamma}\ \phi}{M_a}\left(1 - e^{-\lambda t_i}\right)\left(e^{-\lambda t_d}\right). \tag{2.24}$$

The term $e^{-\lambda t_d}$ represents the time of radioactive decay after the irradiation to obtain the induced activity of the sample used as the gamma source for the irradiation of the optical fibers.

2.6.3 Neutron Self-Shielding

The neutron self-shielding diminishes the neutron flux over a short distance in a sample. When a sample is submerged in neutron flux, the neutrons have a higher probability of being absorbed by the nuclei at its surface, decreasing the neutron flux reaching its center. Then, in other words, the surface layers of the sample will shield the inner layer from the neutron flux. This effect is more significant the larger the sample, the larger the density of absorbing nuclei or the larger the cross section.

The neutron self-shielding factor or the coefficient of neutron absorption is the relationship between the average flux through the sample on the flux that would be at the same location without the sample. Then, the radioactivity induced in a radionuclide is calculated by replacing the flux ϕ with a corrected flux ϕ':

$$\phi' = G_{eff}\phi. \tag{2.25}$$

Where G_{eff} is the neutron self-shielding for the sample used [38].

2.7 Irradiation of the Fibers

2.7.1 Interactions of the Gamma-Ray with the Matter

Overall the interactions between the gamma-ray and the matter, only three mechanisms play a considerable role in the deposition of the ionizing energy:

- Photoelectric effect
- Compton scattering
- Pair production

Those three mechanisms allow a transfer of the energy of the gamma photon, partially or totally, to the target atom into electron kinetic energy. The dose deposition from the gamma-ray is correlated with the energy and direction of the emitted electron.

2.7.1.1 Photoelectric Effect

The photoelectric effect dominates for incident gamma-rays of low energy. In this mechanism, the target atom absorbs the photon and collides with one of its electrons. This electron is ejected from one bound shell of the atom and leads to an emission of a photoelectron. To achieves this mechanism, the incident photon needs to have energy reaching or exceeding the threshold energy, being the electron's binding energy in its original shell E_b:

$$E_e = h\nu - E_b. \tag{2.26}$$

Where E_e is the energy of the photoelectron, h is the Planck constant and ν is the frequency of the gamma-ray. This interaction also leads to an ionized absorber atom with a vacancy electron [39].

2.7.1.2 Compton Scattering

The Compton scattering becomes prevalent for gamma-rays of intermediate energy. This mechanism is an inelastic scattering of a gamma-ray photon by an electron. This incident photon transfers a fraction of its energy to the electron called the recoil electron. After they collide, the

incident photon is deflected through an angle θ from its original direction and can interact with another target electron. The energy transfers can vary from zero to a significant fraction of the photon energy, caused by all the angles possible of the scattering. The energy of the deflected photon $h\nu'$ has a lower frequency than the incoming photon $h\nu$, caused by the transfer of energy [39].

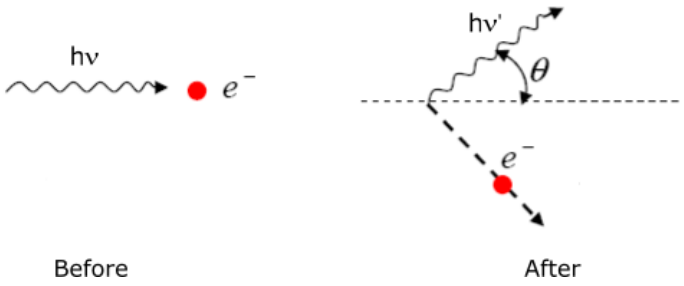

Figure 2.15 Compton scattering. Taken and modified from [40].

The energy of the recoil electron is:

$$E_e = h\nu - h\nu'. \tag{2.27}$$

The energy of the deflected photon is:

$$h\nu' = \frac{h\nu}{1 + \frac{h\nu}{m_0 c^2}(1 - \cos(\theta))}, \tag{2.28}$$

where $m_0 c^2$ is the rest-mass energy of the electron equal to 0.511 MeV.

The energy the incident photon loses is transferred to the electron, leaving the parent nucleus and becoming an ionizing particle. The Compton scattering is more likely to occur with an electron weakly bonded to its nucleus, named free electron.

2.7.1.3 Pair Production

It is energetically possible for a gamma-ray photon with an energy above 1.02 MeV, being twice the rest-mass energy of an electron $2m_0 c^2$, to cause the pair production interaction. The probability of this interaction stays very low until the incident photon has energy over several MeV and collides

with an atom. This interaction converts all the energy of the incident photon to matter. The energy of the photon above 1.02 MeV is transferred into kinetic energy to the electron e^+ and the positron e^-:

$$E_{e^+} + E_{e^-} = h\nu - 2m_0c^2. \quad (2.29)$$

2.7.2 Gamma-Ray Attenuation

Gamma attenuation is based on the assumption that gamma-ray cannot be stopped entirely but only attenuated. This concept is the fractions of gamma-rays that pass through an absorber of thickness t (cm) without interacting and will undergo exponential attenuation. The beam of the gamma-ray photon can be absorbed or scattered away from its main direction. It can be represented by a fixed probability of occurrence per unit path length in the absorber. This probability refers to the gamma-ray removed from the beam, called the linear attenuation coefficient μ (cm^{-1}), involving the interactions of the gamma-ray matter:

$$\mu = \tau(photoelectric) + \sigma(compton) + \kappa(pair). \quad (2.30)$$

The number of transmitted photons I expressed as the photon intensity without attenuation I_0 and the linear attenuation coefficient:

$$I = I_0e^{-\mu t}. \quad (2.31)$$

Therefore, the mass attenuation absorber is more widely used and is defined as the linear attenuation coefficient and absorber density ratio μ/ρ. The attenuation law for gamma-rays with the mass attenuation absorber is:

$$I = I_0e^{-(\mu/\rho)\rho t}, \quad (2.32)$$

where ρ is the density (g/cm^3) and ρt is the mass thickness (g/cm^2) of the absorber.

2.7.3 Radiation Dose

Radiation dose is the energy deposition of ionizing radiation penetrating an object or human body per unit of mass. The energy deposition is different for every material. Then the dose is often expressed as a radiation absorbed dose. The unit for the dose can be given in radiation absorbed dose (rad) or Gray (Gy), being the International system of units (SI) derived units where:

$$100\ \text{rad} = 1\ \text{Gy} = 1\ \text{J/kg}. \tag{2.33}$$

2.7.4 ^{46}Sc as the gamma source

Accelerated gamma irradiation tests for a low dose rate radiation environment like space are usually done using ^{60}Co. However, the activity of the industrial ^{60}Co source is too high for the objective of this test. For similar energies to the ^{60}Co source, ^{46}Sc was activated to use as a source in this irradiation. The choice of ^{46}Sc was made to facilitate waste management. Its half-life is 83.79 days, while the one of the ^{60}Co is 1923.55 days. The ^{46}Sc also has a short half-life, resulting in an important dose rate decrease over the irradiation, making it possible to study the effect of the dose rate variation.

When the ^{46}Sc is formed by neutron activation, it undergoes beta decay by emitting gamma-rays and transforming into titanium-46, a stable isotope.

$$({}^{46}_{21}\text{Sc})^{*} \rightarrow {}^{46}_{22}\text{Ti} + \text{e}^{-} + \gamma \tag{2.34}$$

The disintegration schematic of the ^{46}Sc with the beta and gamma-ray energy is shown in Figure 2.16.

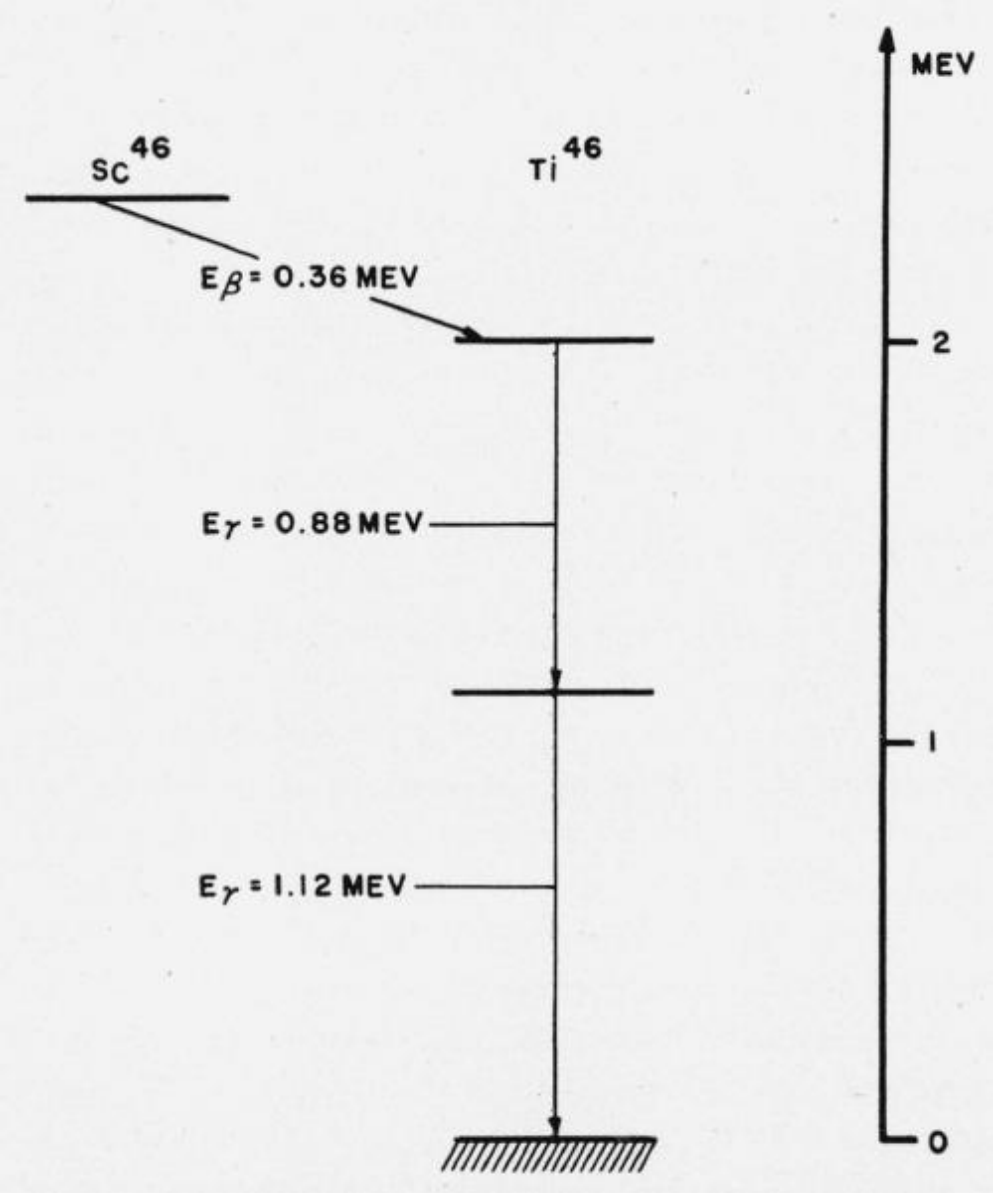

Figure 2.16 Disintegration of the ^{46}Sc into ^{46}Ti with the beta and gamma-ray energy. Taken from [41].

CHAPTER 3 DESCRIPTION OF THE SLOWPOKE-2 NUCLEAR REACTOR

The ^{46}Sc radioisotope was produced using the installations of the SLOWPOKE-2 reactor of Polytechnique Montréal, where the acronym SLOWPOKE is for Safe Low Power Critical Experiment. This nuclear reactor is used for research, especially for neutron activation analysis and the production of radioisotopes. Its design allows to operate it 24 hours per day, at a thermal neutron flux of $10^{12}\ cm^{-2}s^{-1}$, with a maximal power of 20 kW.

This pool-type nuclear reactor has a core located at the bottom of the reactor container in aluminum, filled with light water acting as the moderator and coolant. From the controller, the samples to be irradiated access the different irradiation sites of this reactor via a pneumatic rabbit system through the sample tube shown in Figure 3.1.

The assembly with the main part, the fuel region of the nuclear reactor and its coolant flow are shown in Figure 3.2.

The nuclear reactor core is an assembly of 198 fuel pins and has a diameter of 22 cm and a height of 22 cm. The fuel pins of this reactor are made of ceramic uranium dioxide (UO_2) pellets with low enrichment uranium (LEU) pins of ^{235}U at 19.8% [40].

The control of the fission rate of the nuclear fuel is ensured by the control rod, made of cadmium and covered by aluminum. This rod is moving vertically in and out of the center of the core, guided by an aluminum tube passing by the upper reflector.

The core is surrounded by a neutron reflector made from beryllium annulus and two slabs, one below and one above the core. The upper reflector is shaped into semi-circular shims with a variable thickness, shown in Figure 3.2. The annulus has five inner irradiation sites for the samples and the neutron flux detection site, as shown in Figure 3.3. For this experience, the activation of the radioisotopes ^{45}Sc was made in the irradiation site 5.

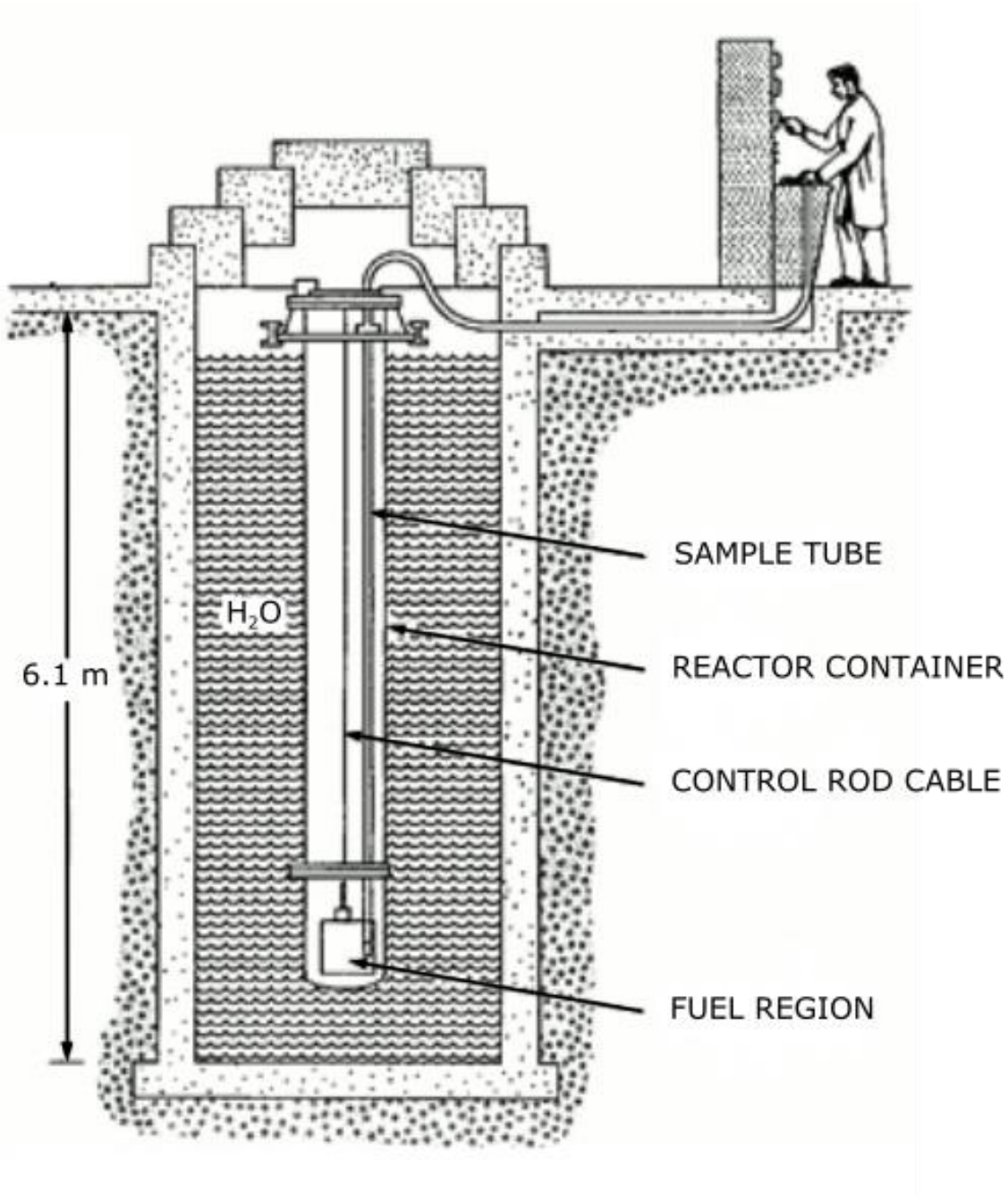

Figure 3.1 Pool of the nuclear reactor with the pneumatic rabbit system. Taken and modified from [42].

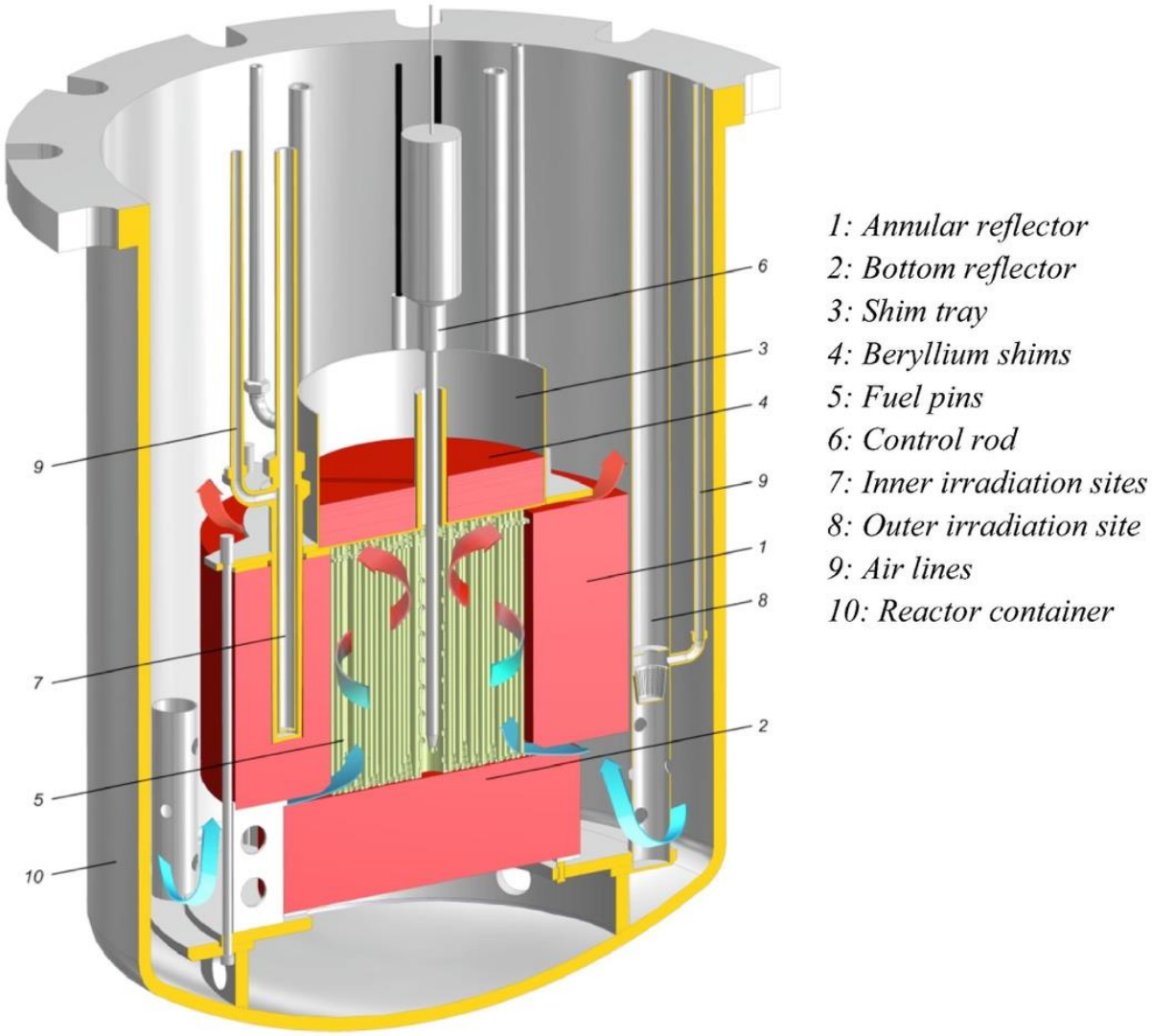

Figure 3.2 Vertical cross section of the lower section assembly of the SLOWPOKE-2 nuclear reactor with the main parts and the coolant flow. Taken from [43].

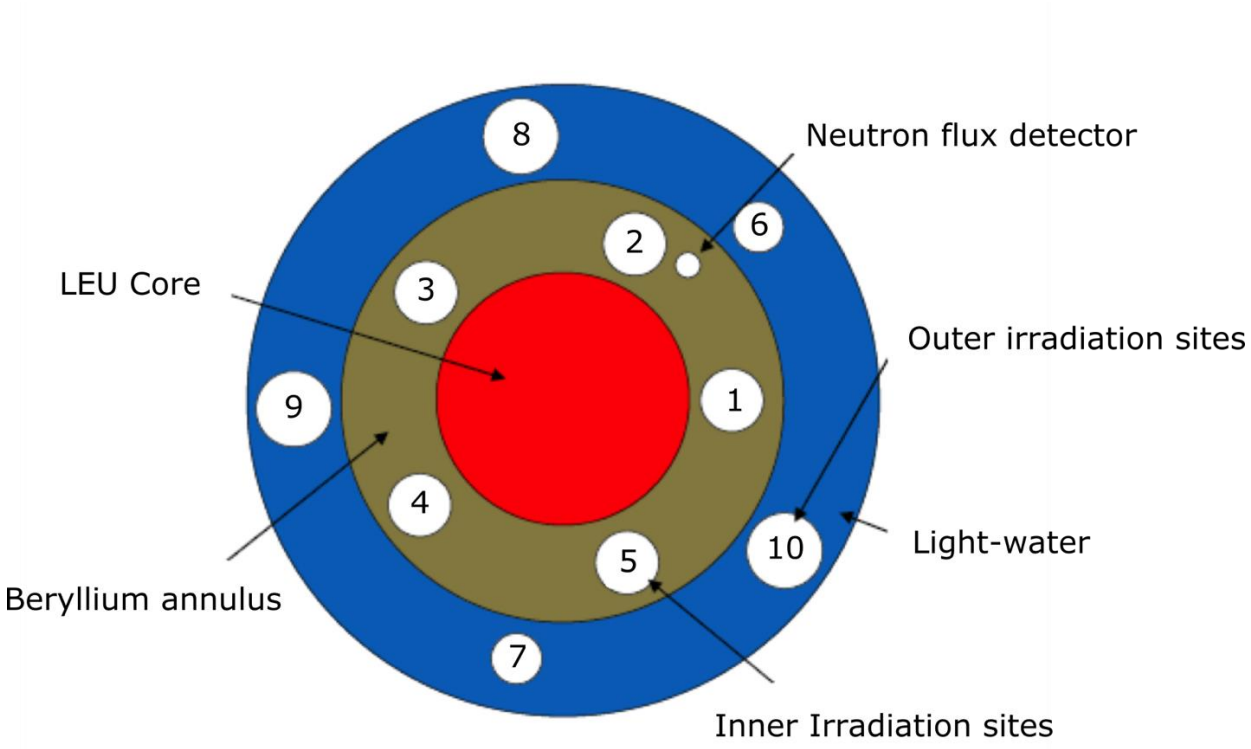

Figure 3.3 Horizontal cross section of the lower section assembly of the SLOWPOKE-2 with the irradiation sites. Taken and modified from [40].

Table 3.1 Example of a table Specifics characteristics of the SLOWPOKE-2 reactor at Polytechnique Montréal. Taken from [40, 44].

Diameter of the core	22 cm
Height of the core	22 cm
Volume of the core	8360 cm^3
Enriched uranium ^{235}U	19.76 %
Critical mass	1100 g
Maximal neutron flux	10^{12} $n/cm^2/s^1$
Fuel life at 10^{11} $n/cm^2/s^1$	20 years
Number of fuel pins	198
Outer diameter of the nuclear container (m)	0.61 m
Height of the nuclear container (m)	5.273 m
Temperature difference of the pool at 10^{12} $n/cm^2/s^1$	17 °C
Diameter of the pool	2.5 m
Height of the pool	6.1 m
Thickness of the beryllium annulus	102 cm
Diameter of the reflector below	322 cm
Height of the reflector below	102 cm

CHAPTER 4 COHERENCE OF THE ARTICLES IN RELATION TO THE RESEARCH GOALS OF THIS THESIS

The research goals in this thesis are the conception, realisation and utilisation of a ^{46}Sc irradiator for REDFs to study their behavior when exposed to a low dose rate of radiation. This project was done in partnership with MPB Communications. The mechanical design and the optoelectronic setup were made in their laboratories with the collaboration of their researchers. The others parts of this project related to the irradiation of the fibers were done at Polytechnique Montréal. The article presented in Chapter 5 was submitted on December 12th, 2022, to the journal "Applied Radiation and Isotopes", and is a summary of the entire work toward achieving the goals of this thesis. It explains all the steps with their elaboration for the realisation of the irradiator. The presentation of the EDFs and EYDFs irradiation using this irradiator is also present at the end of this article with preliminary results. The various authors of this article are all the main collaborators for this project.

CHAPTER 5 ARTICLE 1: ^{46}SC GAMMA-RAY ASSEMBLY FOR STUDYING ERBIUM AND ERBIUM-YTTERBIUM DOPED OPTICAL FIBERS FOR SPACE APPLICATIONS

Clarent Diep[1,2], Emile Haddad[2], Kamel Tagziria[2], Piotr Murzionak[2], Darren Hall[1], Ahmed Naceur[1], Cornelia Chilian[1]

[1]Department of Engineering Physics, École Polytechnique de Montréal, Montréal H3T 1J4, Québec, Canada

[2]Space photonics Division, MPB-Communication, Montréal H9R 1E9, Québec, Canada

This work was submitted in Journal of Optics, November 18, 2022.

5.1 Abstract

The present paper describes the development of a novel low dose rate gamma-ray irradiator based on a ^{46}Sc source inserted in an optical assembly. The performance of seven rare-earth doped fiber amplifiers (REDFAs) was studied during the gamma-ray irradiation of their rare-earth doped fibers (REDFs). The activity and position of the ^{46}Sc vials were modelled with is cylindrical setup, resulting in a radiation dose rate distributed quasi-homogeneous on the REDFs. The model considers neutron self-shielding during vials activation and calculates gamma-ray attenuation in the layers separating the source from the optical fibers. The initial dose rate of the ^{46}Sc source on the REDFs was 27 rad/h and, with the radioactive decay of ^{46}Sc over six months, decreased to 6.3 rad/h, for a cumulative dose of 60 krad. From each of the seven REDFs, three sets were prepared and irradiated to study the effect of gamma-ray radiation with and without photobleaching followed by post-irradiation photo-annealing of the fibers. During gamma-ray irradiation, the first set was functional undergoing photobleaching with an output power between 20.0 and 30.6 dBm. To dissipate their heat, those fibers were spooled on an aluminum cylinder. The other two sets were spooled on 3D-printed Prusa support and irradiated in passive form at 30 and respectively 60 krad. This is the first time this kind of radiation test has been performed at such a low dose rate, more representative of what is received on satellites (0.1 - 10 rad/h). The paper is focused on the irradiator itself connected to the optical setup. For exemplification, a few experimental results are also presented.

5.2 Introduction

Rare-Earth Doped Fiber Amplifiers (REDFAs) are components of interest in several industrial and research sectors. Widely used in telecommunication, they can amplify the signal directly in the third telecom window of 1550 nm with high output powers and low power consumption. This growing technology has other areas of interest, including space missions. REDFAs can provide a high bit rate of information transmission and can be used for inter-satellites and space-based communication due to their efficiency in telecommunication, large bandwidth, lightweight, small volume, reliability and cost efficiency [45]. However, space is a harsh radiation environment, where REDFA are exposed to ionizing radiation.

The high sensitivity to radiation of erbium and erbium-ytterbium doped fibers (EDF, EYDF), the main component used in REDFAs, is the major limiting factor for their use in space. When this component is exposed to irradiation, point defects, also named color centers (CC), are created by electrons and holes trapped on defects in the amorphous silica network pre-existing or created during the exposure [46]. These point defects cause the radiation-induced attenuation (RIA) at the origin of the gain reduction, increasing with the dose and strongly dependent on the core composition [21, 35].

In parallel to those studies, producers of optical fibers are working towards radiation-hardened EDFs and EYDFs to decrease as much as possible the RIA. When they exist, the cost of these radiation-hardened fibers is still too high to permit their commercialization. Hopefully, other approaches can be used to recuperate part of the losses by the RIA. The most common are "bleaching" and annealing the color centers with "photobleaching" [23], photo-annealing and thermal annealing. This gain recovery happens when an optical signal travels in the fiber during the irradiation for the photobleaching and after the irradiation for the photo-annealing. In contrast, thermal annealing occurs when the fiber is exposed to high temperatures.

The efficiency of these mechanisms depends on the fiber dimension, the core composition and the application characteristics like the wavelength, the power, the length of the fiber, the pumping configuration and the temperature [10, 15]. Also, the gain recovery from the optical fiber increases with the injected power for the photobleaching and the photo-annealing, and increases with the temperature for the thermal annealing, which needs to be above 250°C for significant recovery of the optical gain [37].

Various studies characterized the RIA depending on the different parameters to optimize the radiation-hardened erbium and erbium-ytterbium doped fiber amplifiers (EDFAs, EYDFAs) [10, 13, 15, 21]. One study showed the difference in the gain performance of an EDFA by changing the total radiation dose, the EDF lengths, and the type of pumping configuration used during the photobleaching process. They have proven that the optical gain depends on those parameters, and they must be optimized on the EDFAs and EYDFAs for space missions. However, this study has neglected the importance of photo-annealing after the irradiation test [10]. Other studies irradiated fibers with different compositions. They found that the concentration of the rare-earth dopant is not the principal responsible for the radiation sensibility; it is the type of co-dopant affecting the fiber at different intensities. However, the photo-annealing was more powerful when the fiber had significant losses during the irradiation [13, 21].

Terrestrial accelerated-radiation tests at high radiation dose rates in the range of hundreds of rad/h, used to characterize the RIA for space missions, are a common practice for reducing cost and increasing time efficiency, even if satellites are exposed to radiation at a much lower dose rate. In a satellite, an optical component protected from radiation with 0.5 mm of aluminum is exposed to a dose of 100 krad for ten years, giving a dose rate of 1.15 rad/h. However, a REDF can be shielded under many other components and can be exposed to a dose rate as low as 0.1 rad/h to 0.3 rad/h [22]. It was commonly suggested by the European Space Agency (ESA) and European satellite primes (Thales-Alenia Space and Airbus) to perform the radiation test with a dose rate below 390 rad/h to avoid. However, the effect of the irradiation dose rate on REDFs is unclear, bringing controversy on the impact of the dose rate on the RIA. Some research claims that a lower dose rate will induce a higher RIA [11, 12, 19, 20], while others suggest that a lower dose rate will induce a lower RIA [17, 18, 21].

Two erbium fibers without co-dopants have been made to study the RIA effect on the erbium itself by Brichard *et al.* [19]. Each fiber has been irradiated at 45 rad/h and 4500 rad/h for the same total dose of 3 krad. The EDFs with the lower dose rate shows a radiation sensitivity 2.5 higher than the EDFs exposed to the higher dose rate [19]. Furthermore, a theoretical prediction by Gilard *et al.* [12] showed that below a dose rate threshold, defined by the physical characteristics and the temperature of the fiber, the RIA could be up to six times higher than for a dose rate above this threshold. However, this theoretical prediction is not observed in other tests carried out in laboratories or for the EDFAs and EYDFAs used on satellites in service.

In another experiment by Friebele *et al.* [21], fibers co-doped with Al_2O_3 irradiated with a dose rate of 50 rad/h had a loss of 0.4 dBm/m less than for a dose rate of 50 000 rad/h for a total dose of 3 krad. Both fibers were photobleached and photo-annealed during that test for 12 hours combined. Afterward, the fiber with the low dose rate presented a lower loss than the one with the higher dose rate of 0.1 dBm/m [21].

In a real space environment of a low dose rate, an EDFA onboard Probra-2 satellite from the ESA, launched in 2009 and still in service, has been irradiated with an average of 1.11 krad per year from 2009 to 2016 for a total of 8 krad (0.127 rad/h). The RIA is less than 5% (0.2 dB). Moreover, no variation of the RIA was detected during the change in the radiation dose rate in space caused by solar flares [22]. Therefore, accelerated gamma irradiation tests for low dose rate radiation environments, like space, should be re-examined.

This paper presents the modelling and the fabrication of the ^{46}Sc source, its experimental setup to irradiate EDFs and EYDFs receiving a uniformly distributed gamma-ray dose, and the optical instrumentation of the experimental assembly. Three sets of the same fibers were installed for irradiation with ^{46}Sc as a source. One set was active at a nominal power similar to the one used in telecom applications (0.1 W to 1 W), the second set was passive and removed after 30 krad, and the third set, also passive, was removed after a total dose of 60 krad. The objective is to compare the effects of gamma-ray irradiation with or without photobleaching followed by post-irradiation photo-annealing for different fibers. In a subsequent paper, the RIA of those fibers will be compared with the data previously collected by MPB Communications (MPBC) in their last irradiation test with a higher dose rate using the standard method with a ^{60}Co irradiator [16].

The irradiation of the fibers for a cumulative 60 krad, was spread over six months due to the relatively short half-life of ^{46}Sc (83.79 days) compared with that of ^{60}Co (5.27 years). The comparison of the ^{46}Sc and the ^{60}Co nuclear parameters are presented in Table 5.1.

The choice of irradiation tests conducted at low dose rates and over long periods of time is intended to simulate the real-life conditions observed in space. The ^{46}Sc source allowed irradiation of the fibers up to 60 krad using a low dose rate which varied from 27 to 6.3 rad/h. In comparison, ^{60}Co has a dose rate greater than 100 rad/h [16], practically constant during the irradiation process. A previous preliminary irradiation test using a ^{46}Sc source was performed in 2012 with a dose rate of about 350 rad/h. This test showed similar effects to those observed on active fibers using ^{60}Co

sources for the same total doses of 30, 50 and 100 krad [16]. According to the open literature, this is the first experimental gamma radiation test on EDFs and EYDFs at a low dose rate, close to the real dose rate and the total dose observed in space.

Table 5.1 Comparison of the parameters of the ^{46}Sc and the ^{60}Co.

Parameters	**^{46}Sc**	**^{60}Co**
Physical-Half-life (days) [47]	83.79	1923.55
Maximum Beta Energy (keV) [47]	356.8 (100%)	318.1 (99.9%)
Maximum Beta range in air (cm) [48, 49]	93	74
Gammas (keV) [47]	1120.5 (100%)	1332.5 (100%)
	889.3 (100%)	1173.2 (99.9%)
F-factor (cGy/R) [50]	0.965	0.965
Exposure Rate (C m^2 / kg MBq s) [50]	2.09 X 10^{-12}	2.50 X 10^{-12}
Exposure rate (R cm^2 / m Ci h) [50]	10.8	12.9
Half-Value Layer (HVL) for Lead Shielding (mm Pb) [50]	12.5	15.6

This experiment requires a uniform gamma-ray dose on the optical fibers. Therefore, the geometry and the activity of the ^{46}Sc source and the mechanical design need to be optimized while respecting the dimensions of the cylindrical lead shield surrounding the spools. Despite the space constraint, the assembly was designed to accommodate the highest number of fibers, and also to evacuate the heat from the high-power fibers pumped up to 1W. The mechanical design was performed in iteration with the gamma irradiation modeling by calculating and optimizing the configuration of

the ^{46}Sc source in conjunction with the adjustment of mechanical design for converging to an assembly ensuring a uniform dose distribution on all the fibers. Based on the modeling and using the SLOWPOKE-2 nuclear reactor at Polytechnique Montréal, the ^{46}Sc radioactive source was obtained by neutron activation of scandium oxide powder fixed in epoxy. Afterward, the optoelectronic setup was created for the fibers in an active form aiming to investigate the effect of photobleaching by constantly monitoring the output power of the fibers.

This paper presents the design and the implementation of the mechanical structure, the modeling of the gamma irradiator, the preparation and the neutron activation of the scandium source and the optoelectronic setup of the REDFAs. For exemplification, a few preliminary data describing the gain obtained from the active and passive fibers under irradiation with the effects of photobleaching and photo-annealing on the fibers are discussed. Also, this paper presents a data comparison obtained from one specific REDF irradiated with gamma-ray from ^{60}Co and respectively ^{46}Sc sources. The bulk of the tests and analyses are still ongoing. There will be analysed and discussed in a further publication and a comparison of the effects of using ^{46}Sc instead of ^{60}Co radioisotopes.

5.3 ^{46}Sc GAMMA-RAY IRRADIATIOR

The mechanical design, shown in Figure 5.3 was the first step in creating the irradiator. Three main constraints needed to be respected:

1. The limited space inside the irradiator cylindrical lead shield, with an inner diameter of 31 cm and a height of 75 cm.
2. The radioprotection procedures restricted the manipulation of the ^{46}Sc source, therefore the spools supporting the fibers were separated from the tube holding the source. This setup allows inserting and removing the fibers from the cylindrical shielding without irradiating the personnel of the laboratory.
3. The top spool should be removable from the other spool to extract it at a specific time, e.g., to take out certain fibers after 30 krad without disassembling the whole structure.

This mechanical design was drawn with Solidworks 2020, and many components were 3D printed with a Prusa i3 MK3S+ 3D printer using the Prusament PLA Prusa Orange wire material [51]. The two inner tubes consist of clear cellulose (or butyrate). The first 1″ outer diameter (OD) tube guided the vials of scandium inside the setup, while the second tube of 2″ OD aligned the spools with the radiation source. The active fibers were spooled onto an aluminum spool linked to a heat sink to dissipate their heat. The final configuration of the stack of spools has a total length of 208 mm, an outer diameter of 101.6 mm for the spool in PLA and 102.1 mm for the spool in aluminum.

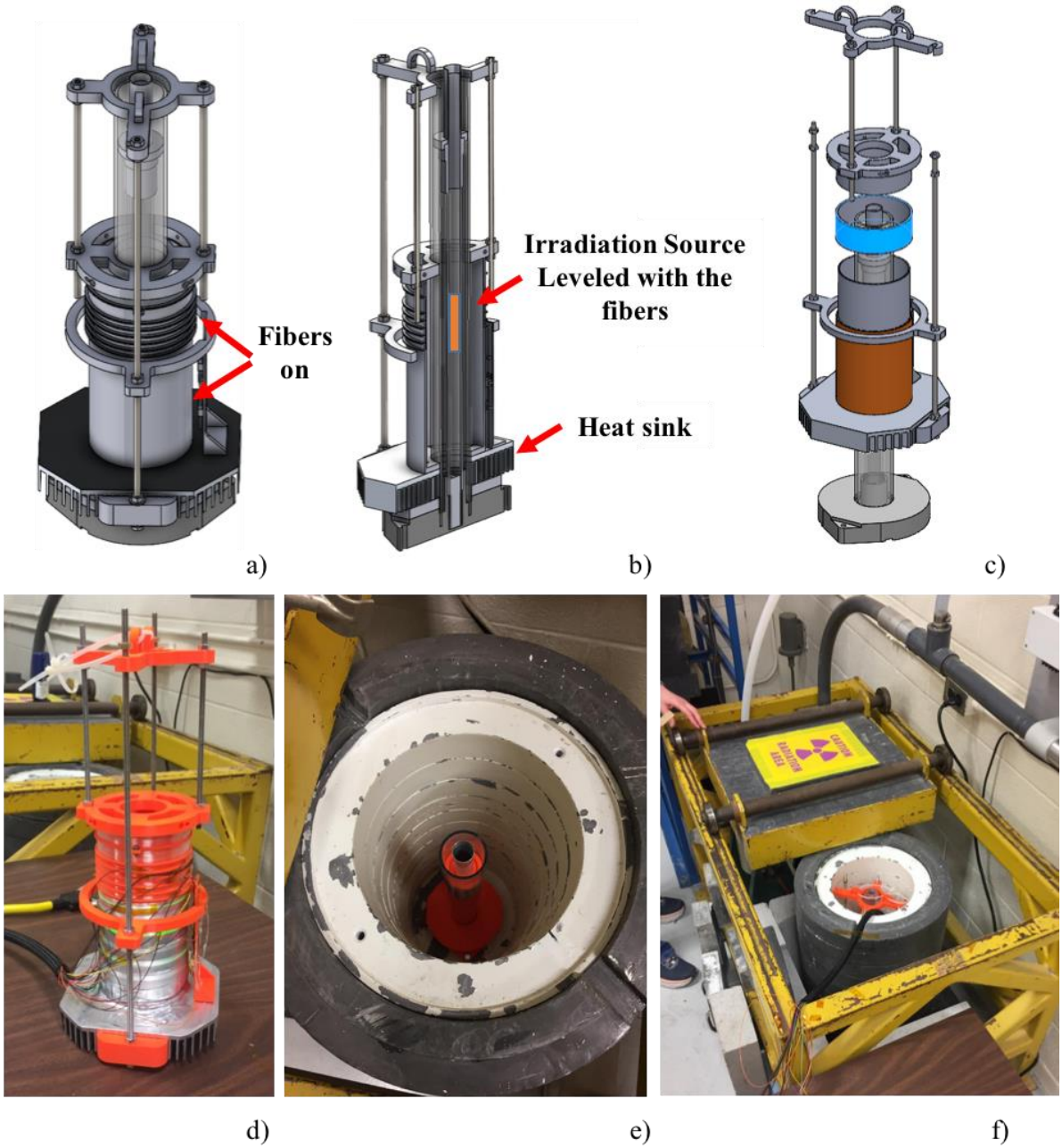

Figure 5.1 Mechanical setup: (a) Schematic of the entire setup with the location of the fibers. (b) Schematic of the cross-section with the location of the irradiation source and the heat sink. (c) Schematic of the removable top spool and the two main parts, the spools and the inner tube. (d) Picture without the inner tube. (e) Picture of the inner tube inside the laboratory's cylindrical lead shield. (f) Picture of the irradiator in the laboratory's cylindrical lead shield during irradiation.

5.3.1 Heat Dissipation

It was planned to mount seven doped fibers pumped up to 2 watts as output power, releasing heat. Therefore, the system's overall temperature increases and could damage some components and skew the optical gain when measured at a higher temperature. However, the heat released by the fibers is not high enough to provoke thermal annealing that usually occurs above 250°C. To dissipate the heat and keep the fibers close to room temperature, the spool for the active fibers is made of aluminum and linked to an aluminium heat sink at the bottom (Figure 5.1 d).

The first test measured the heat on the aluminium cylinder created by the three high-powered fibers. The pump power and output power amplified by the doped fibers are shown in Table 5.2 while the position of the fibers and the thermal sensors are shown in Figure 5.2. The fiber with 2 W output was placed at the bottom to dissipate the heat on the heat sink. The fiber with less power was placed at the upper end of the aluminum cylinder while spacing the three fibers to distribute the heat over the spool. The first thermal sensor was placed on the inner face of the cylinder, while the two others were placed on its external face. The thermal sensors were in direct contact with the cylinder, with a thermal pad over it for good heat conduction and an aluminum tape to hold it.

Table 5.2 Pump power and output power of the three high-powered fibers for the heat test.

Fiber	**Pump power (W)**	**Output power (W)**
EYDF5	9.66	2.02
EYDF6	9.75	1.77
EYDF9	2.43	0.872

The target cylinder temperature was 30.5 C, which represents the hottest component (at room temperature) of the amplifier EOAM-1705 made by MPBC and constructed with the doped fibers to be tested, in operation at 487 mA.

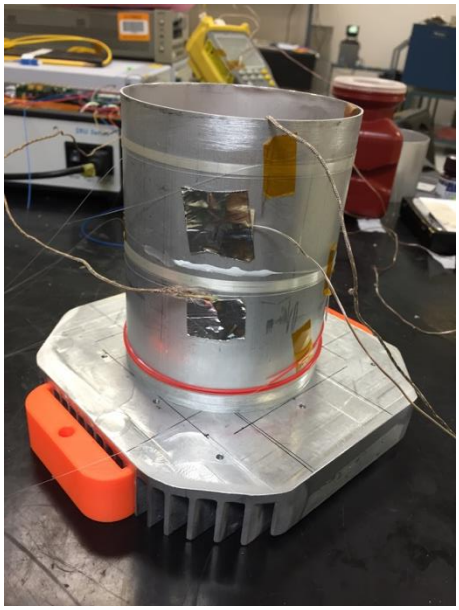

Figure 5.2 Position of the high-powered fibers on the aluminum spool sited on a heat sink with one thermal sensor inside the spool and two others on its surface.

The average temperature on the aluminum spool with the three high-powered fibers was above 44 °C, therefore 13.5 °C higher than the target temperature. Then, to ensure the proper functioning of the fibers over six months of irradiation, the following measures were implemented: insert the heat sink under the spool; link the heat sink with the spool for better heat transmission using a 40 μm thick copper foil; add a copper foil to the entire surface of the inner part of the spool; add Artic Silver 5 high-density polysynthetic silver thermal paste between the spool and the heat sink. All these measures increased the transmission of heat resulting in an average temperature of 36.5 °C, still higher than the target temperature. For this reason, the signal output power of the fibers in an active form has been decreased to 1 W to ensure the proper functioning of the experiment when the seven pumped fibers were mounted.

5.3.2 Gamma irradiation modeling

This section presents the modeling of the gamma irradiation of the optical fibers according to the mechanical design and the activity of a well-defined radioactive source. The objective is to calculate and optimize the distribution of the radioactive dose rate along the spools of the fibers by tunning the position and the gamma-ray activity of the ^{46}Sc gamma source. An optimized irradiator

is obtained in this case when the dose rate is homogeneous within ±1 % along the entire length of the cylinder holding the optical fibers. Therefore, using four polyethylene vials containing the radioactive scandium, a maximum height of 186 mm was achieved while respecting the constraints of the mechanical design (see Figure 5.1). The modeling of the gamma irradiation considers the following elements:

1. The relative activity of the ^{46}Sc gamma-ray vials composing the source
2. The primary gamma-ray energies of ^{46}Sc with their yield and mass energy absorption coefficients
3. The distance between the source and the fibers
4. The neutron self-shielding effect of the scandium during the activation of the vials [52]
5. The attenuation of gamma rays through the multiple layers separating the ^{46}Sc source from the fibers

The approach used for this modeling is a point-by-point method implemented through a Python script. The formalism, the variables to optimize, and the algorithms used are presented in the following sub-sections.

5.3.2.1 Initial Parameters

The variables to be optimized are the relative activity for every point inside one scandium vial within the four composing the source, noted as $A_{x_{sc}}$ $\forall x \in \{1,2,3,4\}$, and the variables *Spacer_lower*, *Spacer_center*, and *Spacer_upper*, representing the spacing in mm between each vial shown in Figure 5.3. All seven of these variables must be optimized to reach a quasi-homogeneous dose over the length of the spools.

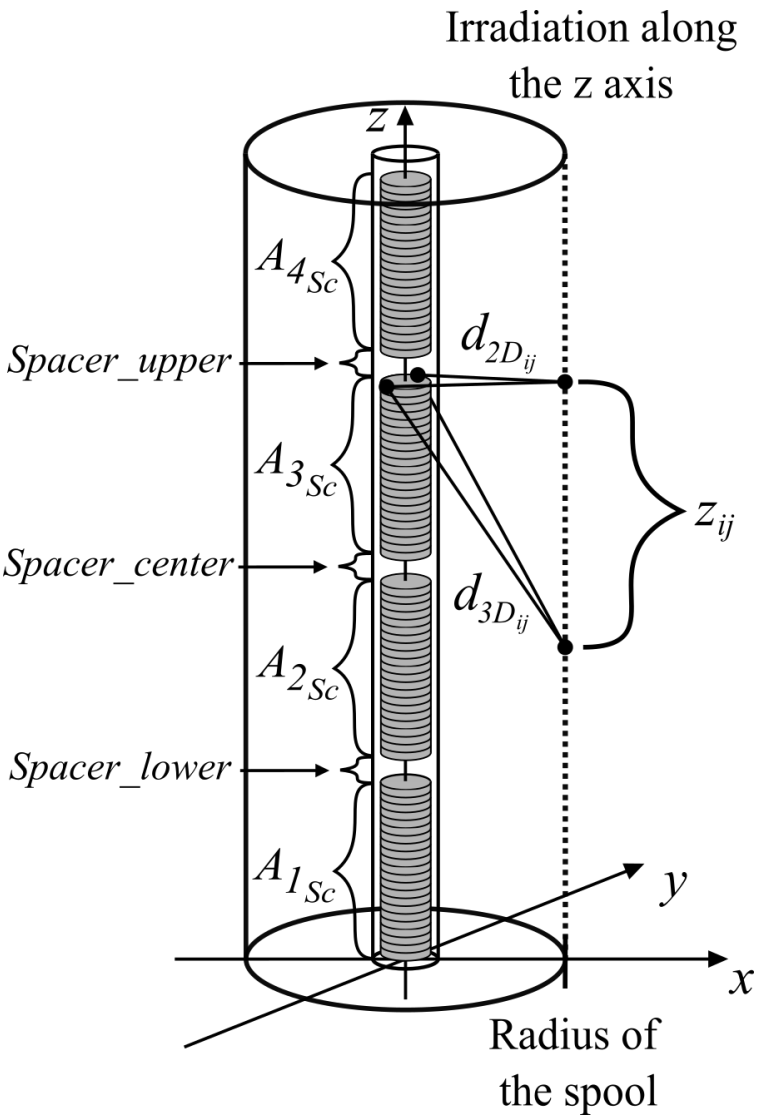

Figure 5.3 Schematic of the irradiator with the scandium vials. This figure shows (i) the variables to be optimized; (ii) the dotted line representing the simplification of the dose calculation along the z-axis; (iii) the schematic representation of the division of each scandium vial into 49 equidistant discs (iv) and $d_{3D_{ij}}$, the distance between point *i* of the optical fiber and the source point *j* of the scandium.

5.3.2.2 Discretization of the optical fibers and the ^{46}Sc gamma-ray source

The source is represented by four cylindrical vials filled with ^{46}Sc which irradiates the optical fibers on a cylindrical spool, resulting in a concentric configuration. Given this radial symmetry, the dose rate is identical for all the fibers located at the same height on the spool; therefore, the dose calculation on the optical fibers is considerably simplified. This calculation is done only on a line along the z-axis at the radius of the spool of coordinates (x, y, z) = (radius of the spool, 0, z) $\forall z \in [0, \text{spool height}]$ shown in Figure 5.3. Afterward, the line representing the optical fibers is divided into points and used with a point-by-point discretization. This type of modelling uses one point per mm, making 208 points along the height of the spool.

Thereafter, the scandium vial needs to be discretized into points, with each vial divided into equidistant discs along the z-axis. Each vial has a height of 55 mm and the scandium mixture inside has a height of 49 mm and was discretized into points over 49 discs, as schematically shown in Figure 5.3. Subsequently, each disc is decomposed into points on seven concentric circles all spaced by a radial distance of 1 mm including the center point. In addition, the circumference of the circles is made up of points spaced by 1 mm, giving 177 points per disc with a total of 8 673 points per vial. The points on the discs were generated in a Python module. Each point is considered a radiation point source to be used further for the dose calculation on the optical fibers.

5.3.2.3 Dose rate calculation

The point-by-point method generates at each point of the optical fibers the cumulative dose rate from the gamma-rays emitted from each point source composing the ^{46}Sc vials. The dose rate calculation follows the inverse square law resulting from the well-known fact that the intensity of the radiation decreases with the square of the distance separating two points, thus:

$$D_{f_{ij}} = \Gamma \frac{A_{x_{sc_j}}}{d_{ij}^2} \tag{5.1}$$

where $D_{f_{ij}}$ is the dose rate on the fibers at point *i* irradiated by a point source *j* located within one of the scandium vials, $A_{x_{sc_j}}$ is the activity of the scandium vial x at point *j* in Bq, d_{ij} is the distance between the points *i* and j in cm. The gamma factor Γ is found using equation (5.2) expressed in

$[\mathrm{s}\cdot\mathrm{R}\cdot\mathrm{cm}^2\cdot\mathrm{h}^{-1}]$ in terms of the primary photon energies of the ^{46}Sc with their yield *y* and their mass energy absorption coefficients $\left(\frac{\mu_{en}}{\rho}\right)_{air}$ shown in Table 5.3. The mass energy absorption coefficients in the air for the photon were found using interpolation from the database given by NIST [53].

$$\Gamma = 5.263\times10^{-6}\cdot\sum_{m} y_m E_m \left(\frac{\mu_{en}}{\rho}\right)_{air_m} \tag{5.2}$$

Table 5.3 ^{46}Sc main photon energies, yield and mass energy absorption coefficient in air.

Energy [54] (MeV)	**Fractional yield [54]**	$(\boldsymbol{\mu_{en}/\rho})_{air}$ **[53]** $(\mathbf{cm^2/g})$
1.1205 45	0.9998 7	0.0273 0
0.8892 27	0.9998 4	0.0284 1
0.1425 29	0.620	0.0247 0
0.0040 91	0.0378	72.99
0.0040 86	0.0191	73.17

With the values given in Table 5.3, the Γ parameter can be calculated using equation (5.2), therefore the dose rate on the fiber becomes:

$$D_{f_{ij}} = 3.9482\times10^{-7}[\mathrm{R}\cdot\mathrm{s}\cdot\mathrm{cm}^2 h^{-1}]\frac{A_{x_{Sc_j}}}{d_{ij}^2}, \tag{5.3}$$

Therefore, by setting an arbitrary value for $A_{x_{sc_j}}$, the only unknown variable needed to find $D_{f_{ij}}$ is d_{ij}.

The distance between a radioactive point source inside the scandium vial and a point making up the optical fibers (d_{ij}) is calculated using the Pythagorean equation: $d_{ij} = d_{3D_{ij}} = \sqrt{d_{2D_{ij}}^2 + z_{ij}^2} = \sqrt{x_{ij}^2 + y_{ij}^2 + z_{ij}^2}$. An example of this geometrical calculation for the mechanical setup used is shown in Figure 5.3. The determination of the total transmitted dose from each point of the scandium to each point of the optical fiber, $d_{3D_{ij}} \forall i, j$, results in the calculation of the dose rate distribution $D_{f_{ij}}$.

Each point of the scandium vial is integrated to calculate the distance $d_{3D_{ij}}$ separating it from one point belonging to the optical fibers. With $d_{3D_{ij}} \forall i, j$, the parameter $D_{f_{ij}}$ $\forall i, j$ can be found, and the dose rate distribution on all the points of the optical fibers can be constructed. This was achieved by summing all the $D_{f_{ij}}$ values on all the points *j* of the scandium vials, thus:

$$D_{f_i} = \sum_j D_{f_{ij}} \ , \forall i. \tag{5.4}$$

This summation is repeated for every point *i* belonging to the optical fibers. The algorithm for the distance calculation with the dose distribution on the optical fiber was also generated in a Python 3.7 module.

5.3.2.4 Neutron Self-Shielding

To obtain the gamma irradiation on the optical fibers, the four vials composing the ^{46}Sc source were activated in the SLOWPOKE-2 nuclear reactor located at Polytechnique Montréal. During the activation of the vials, the outer layers of scandium reduce the number of neutrons available to the inner layers, which will reduce the neutron flux inside the vial equivalent with less activated scandium point sources. This phenomenon named neutron self-shielding is generated by materials with high content of neutron absorbers, in this particular case ^{46}Sc [52]. According to the preliminary neutron activation tests in the SLOWPOKE-2 reactor, the neutron self-shielding reduced the incident neutron flux ϕ of 15%. Thus, the neutron self-shielding decreases also the activity $A_{x_{Sc}}$ of the scandium vial *x* of 15%, and the activity subject to neutron self-shielding A_{ss}

for each vial x is given by: $\sum_j A_{x_{ss_j}} = 0.85 \sum_j A_{x_{Sc_j}}$, where $A_{x_{ss_j}}$ represents the activity of point source *j* belonging to the scandium vial x affected by the neutron self-shielding effect.

For modelling the neutron self-shielding, each scandium vial is divided into concentric cylindrical boxes nested inside each other, forming seven of them using one point per mm discretization as shown in Figure 5.4.

For a given cylindrical box, each point receives the same neutron flux, with the neutron self-shielding effect worsening the longer the neutron travels inside the material. Consequently, each cylindrical box has different activities defined by its position and its activity exponentially decreases with the cylinder diameter. Therefore, the activity of a point source affected by the self-shielding is: $A_{x_{ss_j}} = A_{x_{Sc}} \exp(-\lambda x_{j_k})$. Where $A_{x_{ss_j}}$ is defined as the activity of point source *j* belonging to the scandium vial x affected by the exponential factor. In addition, x_{j_k} represents the thickness through which the neutrons must cross in the scandium to reach the point of interest *j* on the cylindrical box *k*, and λ is an unknown parameter that needs to be determined in order to reach the 15% overall decrease in ^{46}Sc activity due to neutron self-shielding.

The total activity for a scandium vial affected by neutron self-shielding $A_{x_{ss}}$ is expressed by setting an arbitrary value of λ defined according to:

$$\sum_j A_{x_{ss_j}} = A_{x_{Sc}} \sum_j \exp(-\lambda x_{j_k}) \tag{5.5}$$

Thus, by respecting the decrease of 15% in the activity $A_{x_{Sc}}$ of the scandium vial *x*, the value of λ found for this modeling is 0.9534 cm^{-1} as implemented in its own Python 3.7 module.

The three-dimensional representation of the self-shielding factor on the activity of each point of a scandium vial is shown in Figure 5.4.

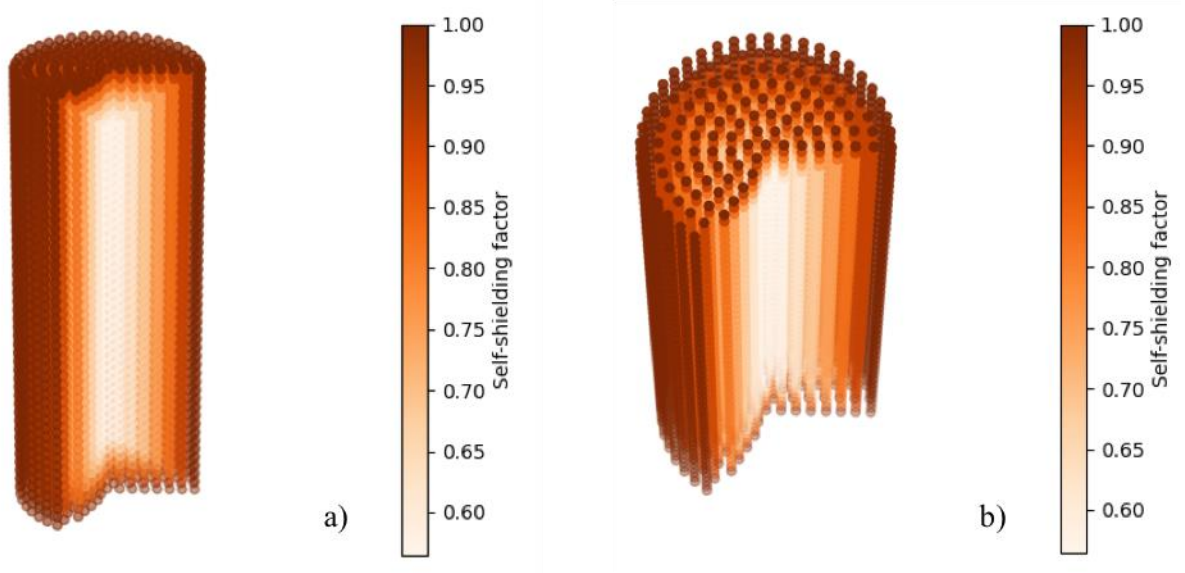

Figure 5.4 Three-dimensional representation of a sectional view of a scandium vial with all its activity points and the self-shielding factors applied to each of them. (a) View from the front, and (b) view from the top.

Therefore, the formulation needed to be considered in equation (5.3) is obtained by replacing $A_{x_{Sc_j}}$ with the activity $A_{x_{ss_j}}$ corrected for the neutron self-shielding:

$$D_{f_{ij}} = 3.9482 \times 10^{-7} \frac{A_{x_{Sc_j}}}{d_{ij}^2} \exp\left(-\lambda x_{j_k}\right) \tag{5.6}$$

which represents the dose rate at point *i* of the optical fibers from the point source *j* of the scandium vial.

5.3.2.5 Gamma-ray attenuation

In the mechanical setup, scandium vials are aligned in a central butyrate tube with the optical fibers on the surface of the spools concentric with the irradiator. With this configuration, gamma-rays pass through several layers of different materials before reaching the optical fiber itself. According to Beer-Lambert's law, the intensity of the gamma-ray is attenuated when passing through a given

material [55], $I = I_0 \exp\left(\frac{\mu_n}{\rho_n}\rho_n t_n\right)$, where I_0 is the intensity without attenuation, μ (cm^{-1}) is the linear attenuation coefficient, ρ (cm^3/g) is the density, and *t* (cm) is the thickness of the material.

The gamma-ray attenuation of each layer must be considered to obtain an accurate distribution of the dose rate along the optical fibers. The two main sections of the mechanical design are made with different materials and are shown in Figure 5.1 (d).

The attenuation calculation is separated into two parts following the two spools design. The upper spool is made only of PLA, and the lower spool is composed of an aluminum cylinder over a PLA cylinder. For both spools, the gamma-rays are attenuated by the two inner tubes made of butyrate, holding the source and respectively guiding the spools. By combining the attenuation of gamma-rays with the formalism developed from equations (5.1) to (5.6), the equation of the dose rate becomes:

$$D_{f_{ij}} = 3.9482 \times 10^{-7} \frac{A_{x_{Sc_j}}}{d_{ij}^2} \exp\left(-\lambda x_{j_k}\right) \prod \exp\left(\frac{\mu_n}{\rho_n}\rho_n t_n\right). \quad (5.7)$$

Here, the index *n* represents the different layers the gamma-rays will need to pass through for the point-by-point calculation. The linear attenuation coefficient, the density and the thickness of every material for the gamma-ray attenuation are shown below.

Table 5.4 Parameters of the different materials for the gamma-ray attenuation.

Material / **Parameters**	Butyrate	PLA		Aluminum
		section without aluminum	section with aluminum	
$\frac{\mu}{\rho}\left(\frac{\text{cm}^2}{g}\right)$ [53]	0.0687	0.0687		0.06146
$\rho\ \left(\frac{\text{g}}{\text{cm}^3}\right)$	1.19	1.24		2.7
t (cm)	0.6425	0.3814	0.3175	0.090
$\exp\left(-\frac{\mu}{\rho}\rho t\right)$	0.948829	0.968031	0.973315	0.985176

This portion of data is implemented in a module programmed in Python 3.7, calculating the gamma attenuation of the materials aligned with the z-axis and the target point of the optical fiber. Improving this implementation can be done by calculating the exact distance t the gamma-rays are going through every material for every case. This script always considers a fixed value of t.

5.3.2.6 Modeling Results

The variables in Table 5.5 have been optimized to reach a dose distribution within ±1 % along the height of the spools holding the optical fibers. To achieve this criterion, the algorithm iterated over various combinations of all seven aforementioned variables and took into account neutron self-shielding and gamma-ray attenuation effects. With the values of the optimized configuration shown in Table 5.5, the dose distribution reached a total height of 186 mm as shown in Figure 5.5. Then, the relative radioactivity of the vials should be $A_{2_{Sc}} = 0.71\ A_{1_{Sc}}$, $A_{3_{Sc}} = 0.68\ A_{1_{Sc}}$, $A_{1_{Sc}} = A_{4_{Sc}}$.

Table 5.5 The optimized relative activity of the four ^{46}Sc vials according to their position and the spacing between them.

Variable	**Value**
$A_{4_{Sc}}$ (Bq)	$A_{1_{Sc}}$
Spacer_upper (mm)	15.5
$A_{3_{Sc}}$ (Bq)	0.68 $A_{1_{Sc}}$
Spacer_center (mm)	9.5
$A_{2_{Sc}}$ (Bq)	0.71 $A_{1_{Sc}}$
Spacer_lower (mm)	14.5
$A_{1_{Sc}}$ (Bq)	A_x

The left side of Figure 5.5 shows the position of the scandium vials on the z-axis, and the right side shows the dose distribution as a function of the position along the z-axis. In this part, the interval between the two horizontal gray dotted lines is the dose distribution which respects the ±1 % variation. The gap between the two horizontal dashed lines in blue defines the lower aluminum spool, and the section between the two horizontal dashed lines in orange defines the upper PLA spool.

To homogenize the distribution of the dose rate on the fibers, the first vial was placed 9 mm below the start of the aluminum spool. Furthermore, as a precaution, to ensure that all the fibers are positioned inside the region of quasi-uniform dose rate distribution of ±1 % variation, the first fiber was placed 8 mm higher than the lower part of this region, and the upper spool ends 5 mm below the upper part of this region.

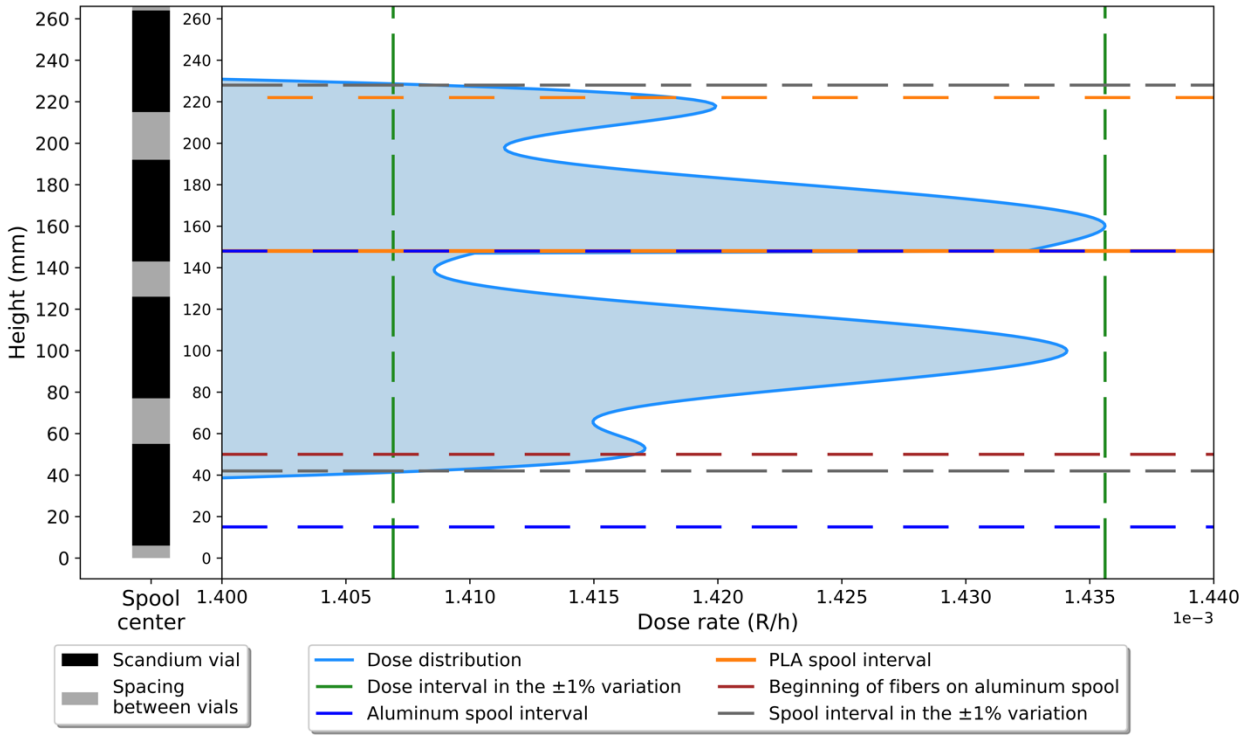

Figure 5.5 Dose distribution along the spool for a total height of 186 mm on the optical fibers. This data considers the self-shielding and the attenuation with the optimized configuration of the scandium vials.

5.3.3 Source Fabrication

For the preparation of the ^{46}Sc radioactive source, the starting point was the desired initial dose rate of 27 rad/h for a total of 60 krad after six months of gamma-ray irradiation from the decaying ^{46}Sc. The source is represented by a stack of four vials containing scandium oxide powder fixed in an epoxy matrix. As the model suggested, the total activity of each scandium vial within the four vials was distributed between 8673 points. For modeling the neutron self-shielding, the activity of each point diminishes exponentially with the depth of the layer where the considered point is located.

The first part of the fabrication of the source was to mix 25 grams of Alpha Aesar Scandium (III) oxide powder, Reactor 99.99% (REO), with 25 grams of PC-Clear Epoxy Paste. Scandium is a monoisotopic element whose atomic weight is determined solely by its isotope ^{45}Sc with an

activation cross-section of 27 barns. The mixture was distributed in four polyethylene vials with an inner diameter of 15 mm and 49 mm total length, with a mixture weight of 11.6 ± 0.2 grams per vial. A small sample of 0.4 grams was collected and further analysed by neutron activation for measuring the scandium content of the mixture. The scandium oxide was solidified with epoxy to avoid potential radioactive spills during the neutron activation of the vials. Epoxy is an organic mixture containing traces of metals such as aluminium, magnesium or sodium. Therefore, to eliminate the gamma-rays generated by their radioisotopes, we added a decay time of four days between the end of neutron activation of the ^{46}Sc source and the start of the actual experiment of gamma-ray irradiation of the optical fibers.

For assessing the neutron activation rate, each vial was pre-irradiated with a low neutron flux at 10^{10} $cm^{-2}s^{-1}$ with an exposure of 30 seconds. After a decay time of 24 hours, each vial was counted for 100 seconds live-time at 250 mm away from the surface of a detector ORTEC HPGe detector with 33% relative efficiency at 1.33 MeV. The gamma-ray activity was determined from the net surface of the 889 keV of ^{46}Sc. Also, this experimental measure of vials' individual gamma-ray activity together with the determination of the scandium content in the 0.4 grams sample confirmed the 15% neutron self-shielding effect, see section 5.3.2.4 [52]. Afterwards, each vial was again irradiated at low neutron flux but with irradiation times between 20 to 40 seconds, to reproduce the model of the gamma-ray activity at the position of each vial into the ^{46}Sc as presented in Table 5.5. Once again, the gamma-ray activity of each vial was measured to predict the neutron activation rate. The vials containing ^{46}Sc were stacked, according to the model, in the central butyrate holder, and further experimental measurement confirmed that the spatial distribution of the dose rate at 50 cm away from the source matched the prediction of the model at this distance.

The next step was to mount the complete mechanical setup including the spools and to measure the dose rate over the length of the spool, which once again confirmed the validity of the model within 3% of the calculated dose rate of 7.05 mrad/h. More, the dose rate outside the setup with the lead shield and at 50 cm distance from the ^{46}Sc source was predicted to be 3.2 mrad/h, a value confirmed later after the targeted activity of the ^{46}Sc source was achieved. The final step was to activate the vials one after the other at a neutron flux of 10^{12} $cm^{-2}s^{-1}$ for 4.2 to 6.2 hours with the target activity of each vial situated between 1.19 and 1.75 GBq. The irradiation times were increased to account the decay intervals of each vial during their sequential activation, cumulating a total time,

irradiation and decay, of close to 58 hours, and also to account the decay time of four days between the end of activation of the last vial and the insertion of the spools into the ^{46}Sc irradiator.

5.4 OPTOELECTRONIC SETUP

5.4.1 Components and Fibers

The study of the photobleaching effect is essential for an understanding of the radiation effects caused by space radiation on REDFs. The EDFAs and EYDFAs found in satellites are pumped during their mission, being under the process of photobleaching. However, in the satellite, a redundant optical amplifier is provided as a backup in passive form, i.e., not pumped. This component does not undergo photobleaching unless the primary EDFA fails. The irradiation of seven fibers in active and passive forms was done to investigate the two possible cases found in satellites. This configuration makes it possible to investigate the performance of each amplifier during and after the irradiation. Furthermore, it makes it possible to compare the data obtained after the irradiation from the sets of fibers in active and passive forms. It also makes it possible to study the photo-annealing between them.

Three broadband sources, seven amplifiers, and one power meter were used to activate the seven fibers. This experiment used two MPBC Er3+ broadband dense wavelength division multiplexing (DWDM) Compsource 9022. That source, simulating a DWDM signal, has 90 channels composing the telecommunication C-band between 1529.55 nm and 1565.09 nm [56]. The amplifier of the EYDF7 was connected to a broadband source having a continuous wavelength between 1530 nm to 1560 nm. For the data acquisition, a Thor Labs S146C power meter was used. The parameters of each active fiber and its amplifier are shown in Table 5.6, and the optoelectronic setup is shown in Figure 5.6.

Table 5.6 Characteristics of the different amplifiers and active fibers under irradiation.

Fiber	**Specifications**	**Length (m)**	**Signal power (dBm)**	**Pump power (mW)**	**Output power at 0 krad (dBm)**
EDF1	Single Mode Er-Doped Polarization Maintaining (PM) Fiber	3.3	1.0	253	19.50
EDF2	Single Mode Er-Doped Rad-hard fiber	3	1.0	253	18.33
EDF3	Standard Single Mode Er-Doped Fiber	7.7	1.0	260	19.79
EDF4	Standard Single Mode Er-Doped Fiber	10	1.0	626	22.33
EYDF5	Er-Yb-Doped Double Cladding Fiber (DCF)	7	19.0	5725	30.60
EYDF6	Er-Yb-Doped DCF	6	19.0	6056	29.48
EYDF7	Er-Yb-Doped DCF, Contra-pumped, same kind as EDF5	6	10.5	2430	27.10

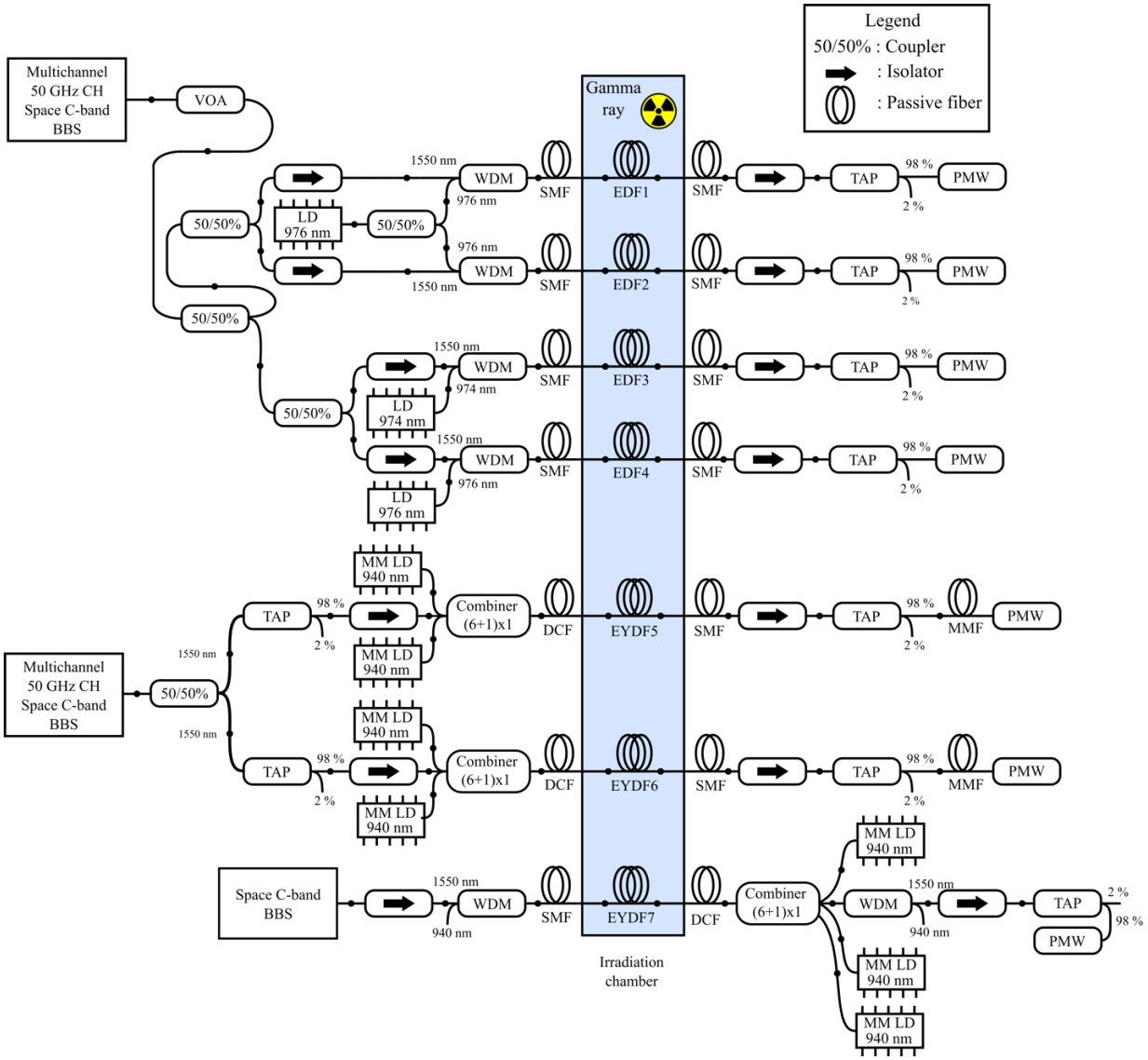

Figure 5.6 Optical schema with the amplifiers of the sevens fibers under gamma irradiation.

5.4.2 Assembly

The electronic assembly was set up in the reactor room. All the optoelectronics were connected, that is, the broadband sources were linked to the amplifiers with the fibers to irradiate. The laser diode was controlled with a computer and the last one was collecting the data acquired by the power meter moving in front of each amplifier signal output. The power meter was mounted on the mechanical stage LIMO SPVM8L150UA, having a precision of ± 0.05 mm, as shown in Figure 5.7 a). The mechanical stage, controlled by a program on the computer, took the output power of

each amplifier every 30 minutes for the duration of the irradiation. The final setup is shown in Figure 5.7 b).

a) b)

Figure 5.7 Setup in the nuclear reactor room, (a) the mechanical stage with the amplifiers and (b) the final setup at the beginning of the irradiation.

5.5 RESULTS AND DISCUSSIONS

Once the assembly was completed, i.e., when the active ^{46}Sc sources were in the laboratory's cylindrical shielding and the fibers on the spools, the spools were put in the shield around the source. At that moment, the irradiation of the fibers commenced.

At the beginning of the irradiation, the dose rate was at 27 rad/h, decreasing with its half-life of 83.79 days. The total target dose of 60 krad was reached over 174 days. In the context of this study, the ^{46}Sc source irradiated three sets of fibers. Each set contains identical fibers and lengths, as shown in Table 5.6. Their irradiation timeline, dose and dose rate throughout the irradiation are shown in Figure 5.8 and the irradiation specifications are in Table 5.7.

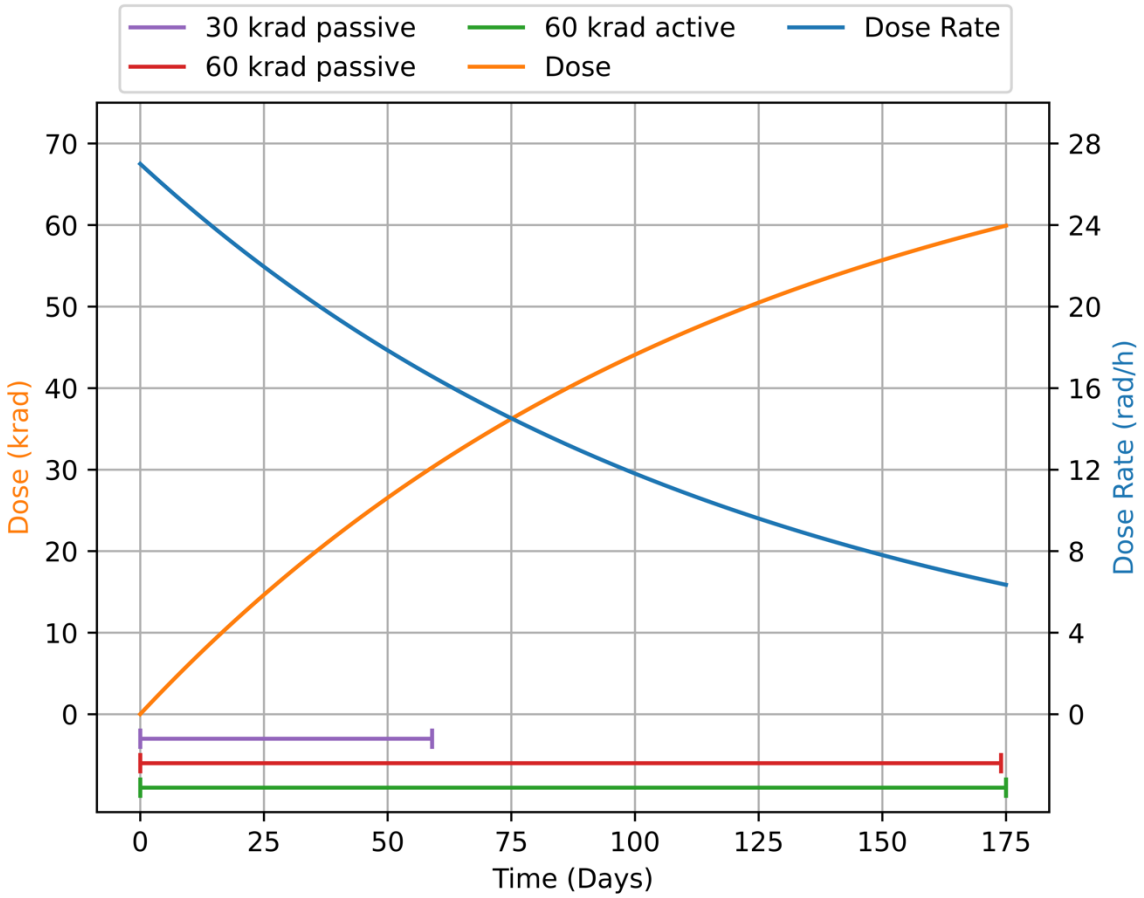

Figure 5.8 Total dose and dose rate versus the time in days and the timeline of the three sets of fibers under irradiation.

Table 5.7 Specifications of the irradiation for the different sets of fibers.

Total Dose (krad)	Form	Initial		Final		Time under irradiation (days)
		Day	Dose rate (rad/h)	Day	Dose rate (rad/h)	
30.2	Passive	0	27	59	16.6	59
59.8	Passive	0	27	174	6.4	174
60	Active	0	27	175	6.3	175

The first set of passive-form fibers was irradiated for a total dose of 30.2 krad during the first 59 days. The second set of fibers in passive form and the last in active form, under photobleaching, were installed at the beginning of the irradiation and received a total dose of 60 krad.

With the data set of the active fibers, it is possible to study the effects of the RIA on the optical gain as a function of the dose. Moreover, the photobleaching and photo-annealing effects can be investigated by comparing the fibers in passive and active forms.

Although the current paper is more dedicated to the ^{46}Sc irradiator, as a proof of concept, it presents a preliminary view and analysis of the data taken during the irradiation. Many of the fibers are still undergoing photo-annealing. A future paper will provide the analysis and discussion of the radiation, photobleaching and photo-annealing, and present a data comparison with fibers irradiated under ^{60}Co.

For this irradiation under ^{46}Sc gamma-rays, the output power was taken every 30 minutes for the seven fibers in active form. Their gain versus both the dose and associated dose rate is shown in Figure 5.9.

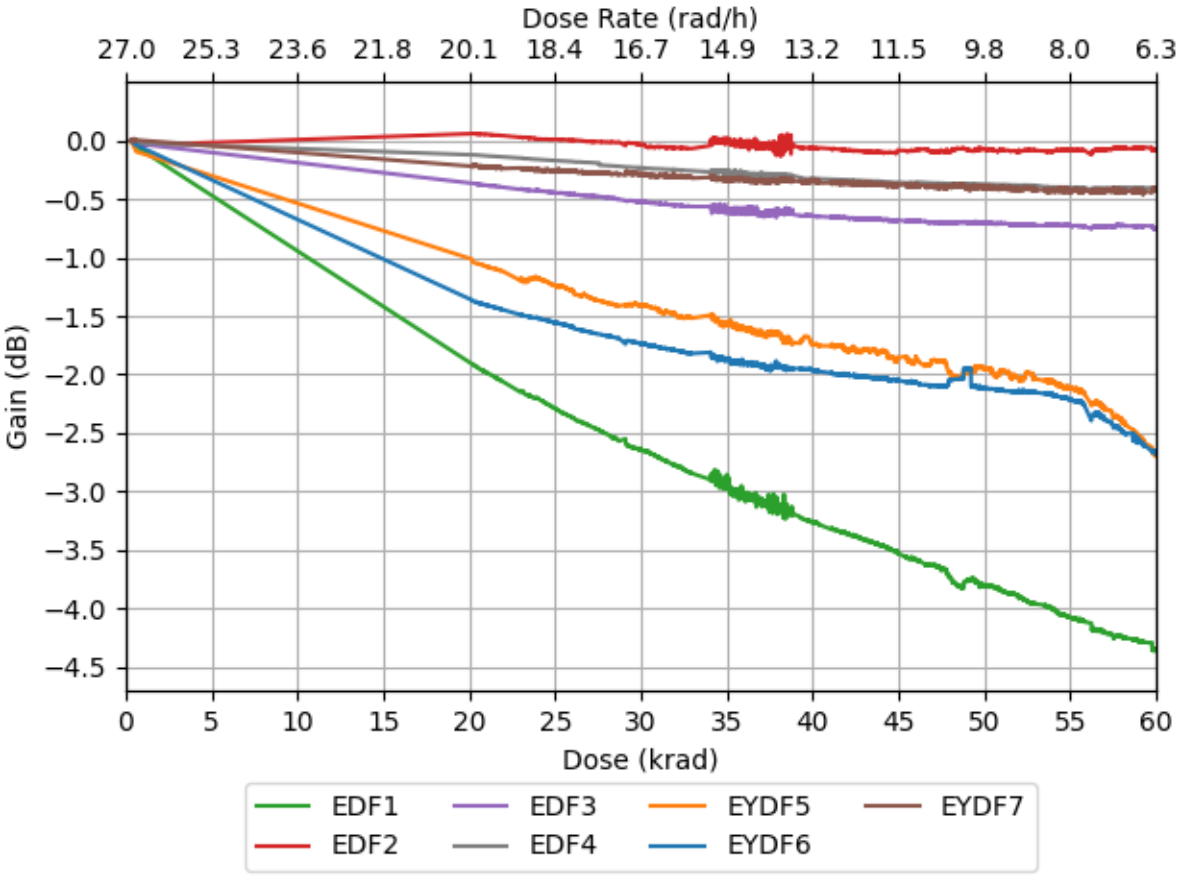

Figure 5.9 Loss in gain for each fiber in active form, undergoing photobleaching, versus both the dose from 0 krad to 60 krad and the associated dose rate.

Following the beginning of the test up to 20 krad, certain problems were encountered with the power meter and data was not acquired from 0.5 krad to 20 krad. After these issues were resolved, the data was acquired normally. Figure 5.9 also shows noise between 34 krad and 38 krad due to a large bandwidth setting on the power meter for this period.

The results obtained show, as predicted, the gain decreasing with the dose caused by the RIA. Furthermore, with this ^{46}Sc irradiator, the dose rate significantly decreases while the total dose increases. With the photobleaching, the data show less loss with the total dose as the dose rate decreases. This phenomenon can be explained by the fact that the photobleaching decreases the CC during irradiation, and a decreasing dose rate slows down the point defect mechanism. Those two effects combined reduce the RIA induced on the fibers. However, the steep gain decrease that started at 55 krad for EYDF5 and EYDF6 is for now unknown. A more detailed investigation of

this gain decrease and the effect of photobleaching over the decreasing dose rate will be presented in future work.

Also, with the acquired data, we can affirm that the RIA's effect depends not only on the fiber itself but on the application characteristics since EYDF5 and EYDF7 are the same fiber and EYDF5 loss more than 1.5 dB than EYDF7 for a total dose of 55 krad. EYDF5 is one-meter longer and has a higher signal and pumping power than EYDF7, while the latter was contra-pumped.

The RIA mechanism of the slow irradiation with this ^{46}Sc irradiator is another aspect that will be studied. The gain comparison of the same fiber and optoelectronic setup between this irradiation and other irradiation using ^{60}Co sources for various fibers will be analysed and presented in a future paper. Currently, only the EDF4 is ready to compare. Figure 5.10 shows the difference in the gain for EDF4 irradiated with this ^{46}Sc irradiator and a ^{60}Co source for a total dose of 60 krad. The ^{60}Co irradiation was 12.5 days with a constant dose rate of 204 rad/h, while the irradiation with the ^{46}Sc was 174 days at a varying dose rate of 27 rad/h to 6.3 rad/h. The EDF4 exposed to the lower dose rate under the ^{46}Sc shows a higher gain. This observation could be explained by the photobleaching of this fiber for 161.5 days more than the one irradiated with the ^{60}Co. However, Figure 5.10 mainly aims to prove that REDFAs used in satellites and exposed to a lower dose rate over an extended period of time have a higher gain than terrestrial accelerated gamma irradiation tests.

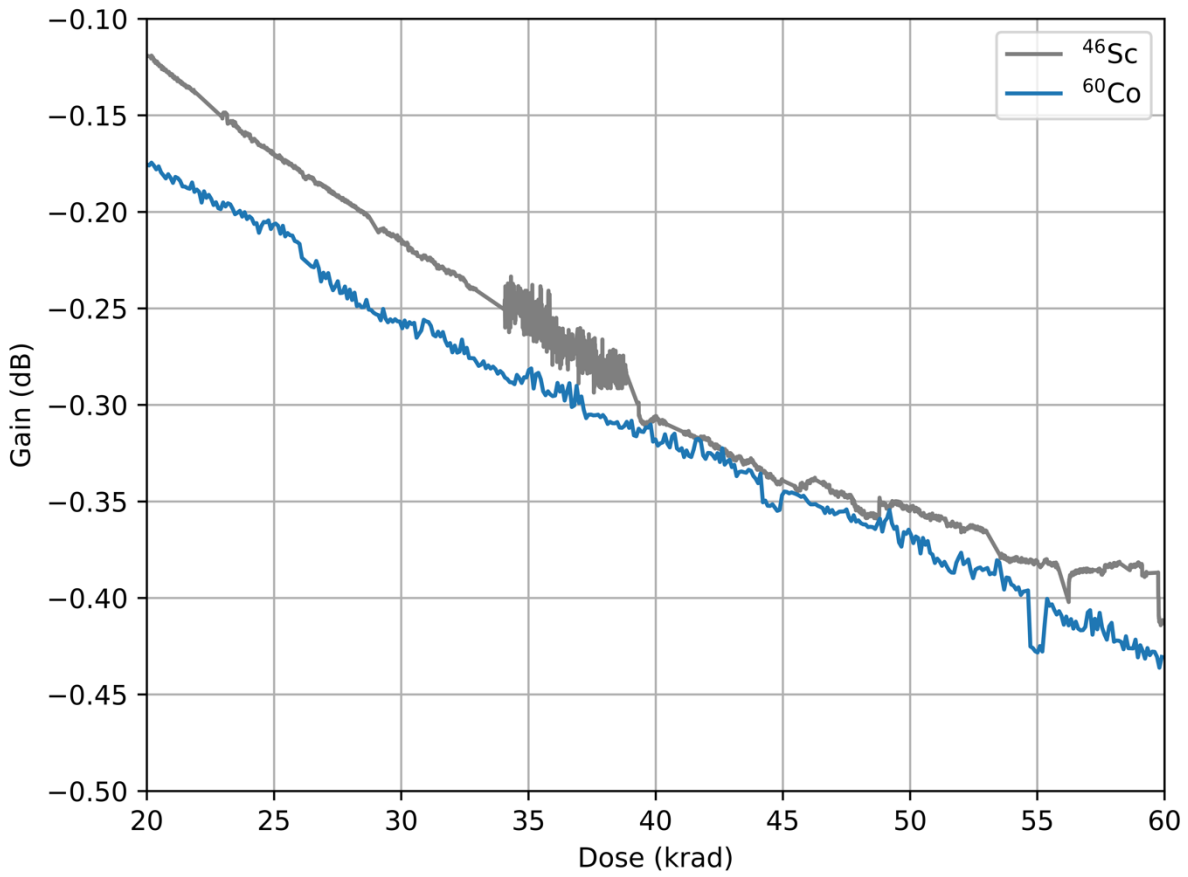

Figure 5.10 Gain vs the dose for EDF4 irradiated with this ^{46}Sc irradiator and a ^{60}Co source.

During this irradiation using ^{46}Sc, fibers in passive and active forms were irradiated for the study of their comparison with the photobleaching and photo-annealing. Currently, the fibers are continuously under photo-annealing. The comparison of EDF4's gain, photobleaching effect and photo-annealing is presented in Table 5.8. The photo-annealing of EDF4 was done under the same conditions then the EDF4 in active form during irradiation shown in Table 5.6.

Table 5.8 EDF4 gain and recuperation with photobleaching and photo-annealing.

Total Dose (krad)	**Irradiation form**	**Gain (dB)**	**Gain Recuperation**	
			Photobleaching (dB)	**Photo-annealing for 7 days after irradiation (dB)**
30	Passive	-1.37	-	0.85
	Active	-0.22	1.15	Not measured
60	Passive	-2.42	-	1.55
	Active	-0.43	1.99	0.03

The EDF4 under photobleaching has recovered more than the ones in a passive form during irradiation and exposed only to photo-annealing. The gain recuperation of the photo-annealing shows a strong recovery at the beginning of the first day. Afterward, the gain increases slowly which gives the impression of following an asymptote, but always increasing quietly without having an actual asymptote. Furthermore, the photo-annealing after photobleaching on the fiber followed the same trend as the fiber not under photobleaching during irradiation but recuperates much less than the last one as shown in Table 5.8.

5.6 CONCLUSION

This experiment demonstrates the successful building and testing of a novel REDF irradiator that uses a low dose rate ^{46}Sc gamma source to irradiate optical fibers under radiation conditions similar to those found in space. We irradiated three sets of seven REDFs, namely, 4 EDFs and 3 EYDFs. The first set was irradiated for a total dose of 30 krad and the second for 60 krad, both in passive form. The last set was in active form, up to 60 krad, undergoing the photobleaching effect throughout the entire irradiation. The fibers in active form were pumped from 0.1 W to 1 W. During the test, the dose rate decreased from 27 rad/h to 6.3 rad/h for a total irradiation of 60 krad due to the limited lifetime of the ^{46}Sc radioisotope. Given the experimental results we obtained, the irradiator presented in this work represents an advantageous alternative to the commonly used ^{60}Co sources for fiber radiation tests.

The irradiator was developed through various tasks. Firstly, the mechanical setup of the irradiator was 3D printed with additional components having specific thermal conductivity properties. After heat tests, an aluminum spool and a heatsink were added to the setup to dissipate the heat generated by active fibers. For radioprotection purposes, the design of this irradiator was made in different parts, that is, the fiber spools could be added and removed from the SLOWPOKE laboratory's cylindrical lead shield separately from the part containing the radioactive source. Secondly, the irradiation modeling, using a point-by-point method, was used to optimize the homogeneity of the dose on the optical fibers. This was achieved considering the mechanical setup dimension, the neutron self-shielding of the ^{46}Sc source and the gamma-ray attenuation. A homogenous dose of a maximum height of 186 mm on the spools was achieved with four ^{46}Sc mixtures of 49 mm height. Once the relative activity of the vials was calculated, the neutron activation of ^{45}Sc powder mixed with epoxy generated ^{46}Sc radioisotopes and was done in the SLOWPOKE-2 nuclear reactor at Polytechnique Montréal university. The irradiation of the four vials was done with a neutron flux of 10^{12} $cm^{-2}s^{-1}$ for different time intervals, varying from 4.2 to 6.2 hours. The end product of this activation was four radioactive vials of ^{46}Sc with an induced activity between 1.19 and 1.75 GBq.

The optoelectronic setup was designed to monitor and measure the power through the REDFs and was mounted in the nuclear reactor room before the irradiation started. This process used different configurations of amplifiers, pumped forward and backward at different powers. One power meter moving along a mechanical platform acquired data from each active fiber every 30 minutes.

This paper is dedicated to the ^{46}Sc irradiator and presents a preliminary view and analysis of the data taken during the irradiation. The measurements of a fiber, the EDF4, were analysed under radiation conditions similar to those found in space. The fiber gain in passive and active forms was compared for the same total dose (30 and 60 krad), showing an essential role of photobleaching in recuperating the loss of gain. The analysis also confirms that the configuration of REDFAs has an impact on the gain during the irradiation because the same fiber represented by EYDF5 and EYDF7 in active form with a contra-pumping configuration loses much less than with a co-pumped configuration with a higher power. To study the difference between the ^{46}Sc and the ^{60}Co, data from a ^{60}Co irradiation is compared with the data acquired with the ^{46}Sc irradiator. Both irradiations were performed on EDF4 in active form for a total dose of 60 krad. This comparison showed less critical losses for the fiber irradiated under the low dose rate of the ^{46}Sc when exposed for a longer time. This observation suggests that the loss of gain of the REDFs in space, exposed to a low dose rate for a long period, would be inferior to the loss of gain observed in the accelerated gamma tests usually made with ^{60}Co. Also, according to the open literature, this is the first time the photobleaching and photo-annealing effects were compared. Fibers under photobleaching during the irradiation recuperate a small gain during the photo-annealing, while the fibers in passive form during irradiation recuperate a critical gain. Furthermore, at least for the EDF4, the gain observed for passive fibers after photo-annealing stays lower than the gain of the fibers under photobleaching.

Various fibers are currently under photo-annealing, and data analysis is in progress. A future paper will discuss and analyse the detailed measurements of the different mechanisms present in this experience (i.e., the dose rate, the photobleaching and the photo-annealing), and offer a comparison between the effects of using ^{46}Sc and ^{60}Co radioisotopes.

CHAPTER 6 GENERAL DISCUSSION

The previous article presents in Chapter 5 did not present the passive set of fibers irradiated at a low dose rate for a total dose of 30 krad because no data is collected for these fibers at this time. Also, the active fibers continued to be under irradiation up to 75 krad. The time of irradiation of those two sets of fibers is added from figure Figure 5.8 and shown in Figure 6.1.

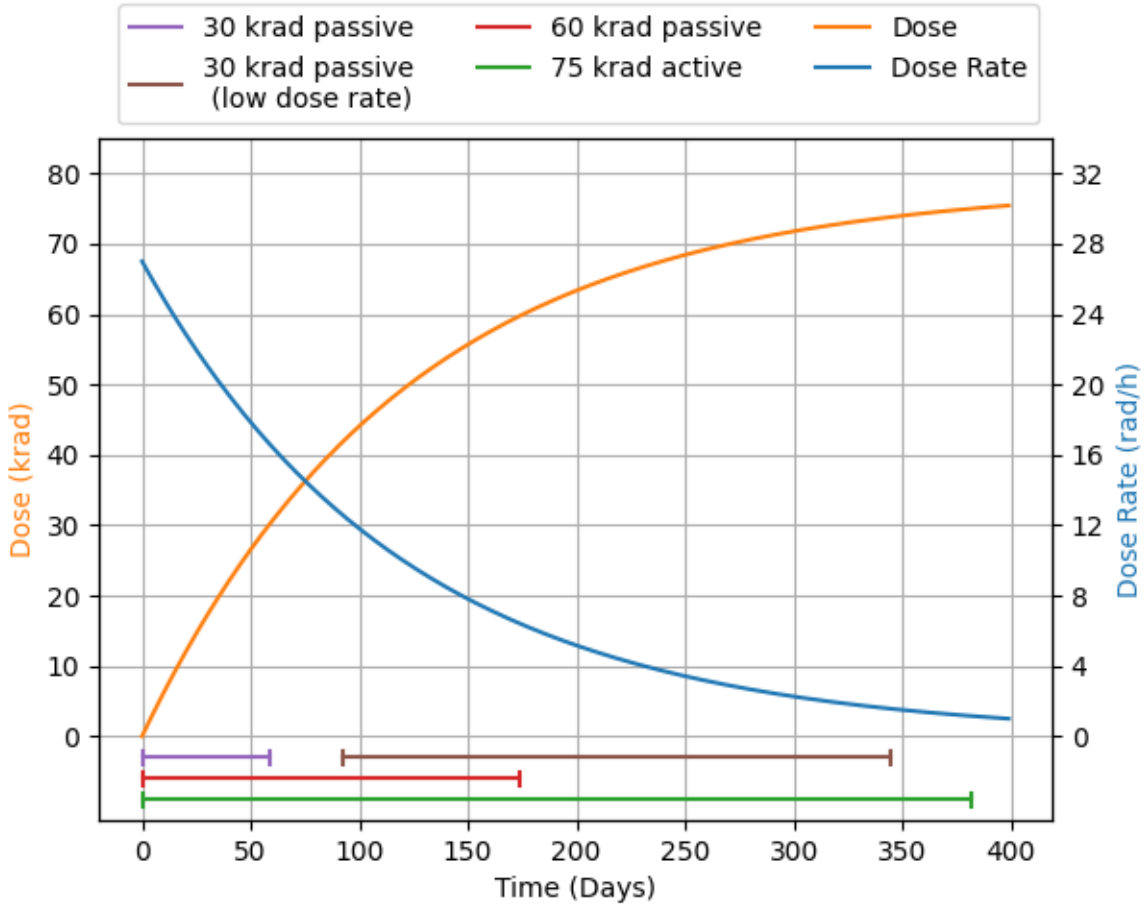

Figure 6.1 Total dose and dose rate versus the time in days and the timeline of the 5 sets of fibers under irradiation with the active fibers for a total dose of 75 krad and the set at 30 krad irradiated under a low dose rate.

Also, the article didn't mention the work on analyzing the gain gradient because the analysis is incomplete. The gain gradient studies the gain variation over a defined dose interval. The purpose is to obtain a relationship between the gain and the decreasing dose rate throughout the irradiation as shown in Figure 6.1. For this irradiation, according to some studies [11, 19, 20], the gain, mainly affected by the RIA, should decrease faster over the irradiation, then induce higher RIA with a

lower dose rate, while for others [17, 18, 21], it should decrease slower, then induce lower RIA with a lower RIA.

The gain gradient must be calculated on all the acquired data to obtain its correct representation. Due to noise and missing data on some dose intervals, data smoothing and interpolation were performed.

First, the data smoothing of EDF1 gain was made on the various continuous data intervals using the Savitzky-Golay filter on Python 3.7. This digital filter smooths the data using a subsequent subset of points by fitting them with a low-degree polynomial, third-degree for this study. Over this smoothing, data interpolation was done to obtain a continuous curve using the function *pchip* (Piecewise Cubic Hermite Interpolating Polynomial) on Python 3.7. This function interpolates using monotonic cubic splines. Figure 6.2 shows the raw data of EDF1, the smoothing and the interpolation.

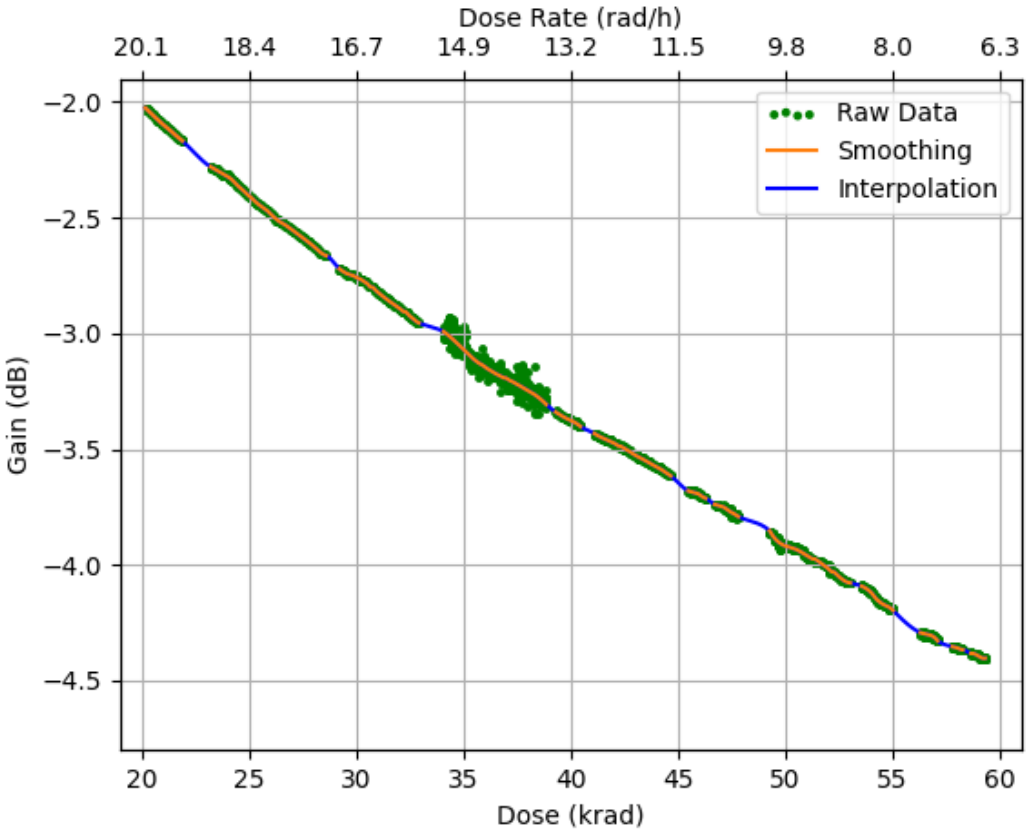

Figure 6.2 Raw data of EDF1 gain with its smoothing using the Savitzky-Golay filter and the interpolation using cubic splines on Python 3.7.

The gain gradient was calculated on the three data sets, the raw data, the smoothing and the interpolation. To do so, linear regressions were calculated on the data using a five krad moving average. The last one did not consider the data between 34 and 39 krad for the raw data because it was too noisy. The value of each linear regression slope gave the gain gradient according to the dose and dose rate, as shown in Figure 6.3. To observe the trend of the gain gradients, the slope of their linear regressions was calculated, and their values are shown in Table 6.1.

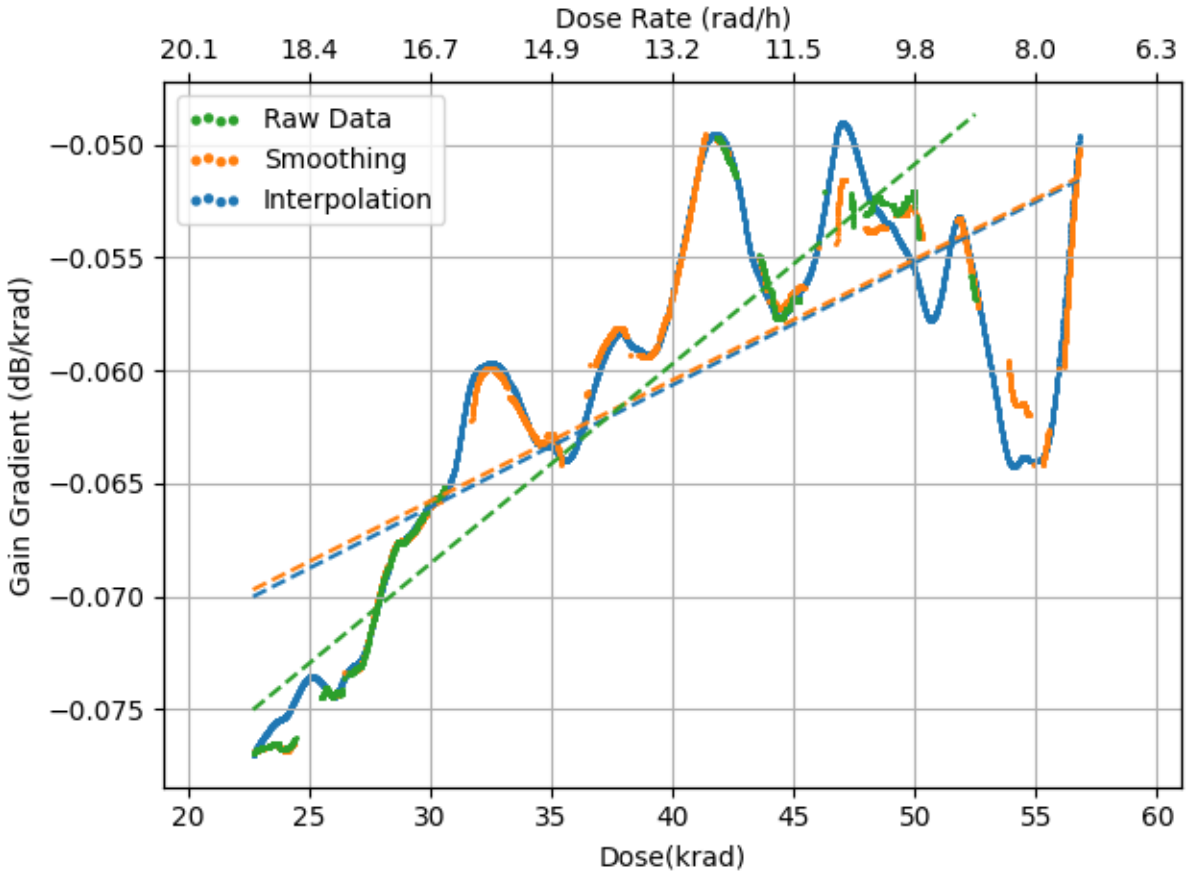

Figure 6.3 Gain gradient of the three data sets with their linear regression slope.

Table 6.1 Linear regression slope of the gain gradient for the three data sets.

Data set	**Raw Data**	**Smoothing**	**Interpolation**
Linear Regression Slope	8.83×10^{-4}	5.35×10^{-4}	5.40×10^{-4}

The results weren't present in the article because more research needs to be done to explain these results, the positive to negative slope variations and to conclude with the data. With a short analysis, this variation may be caused by temperature variation and accidental disturbances of the fibers in the laboratory since they are bend radius sensitive. However, this experience demonstrates the increase in gain with a decreasing dose rate by its positive linear regression slopes shown in Table 6.1. This led to the conclusion that this fiber, EDF1, used for space applications will have lower gain losses than terrestrial accelerated gamma irradiation tests having a higher dose rate than in space.

As mentioned before, the active fibres' irradiation was still ongoing during the article's redaction. The irradiation continued for a total dose of 75 krad, reaching a dose rate of 1.1 rad/h, as shown in Figure 6.4.

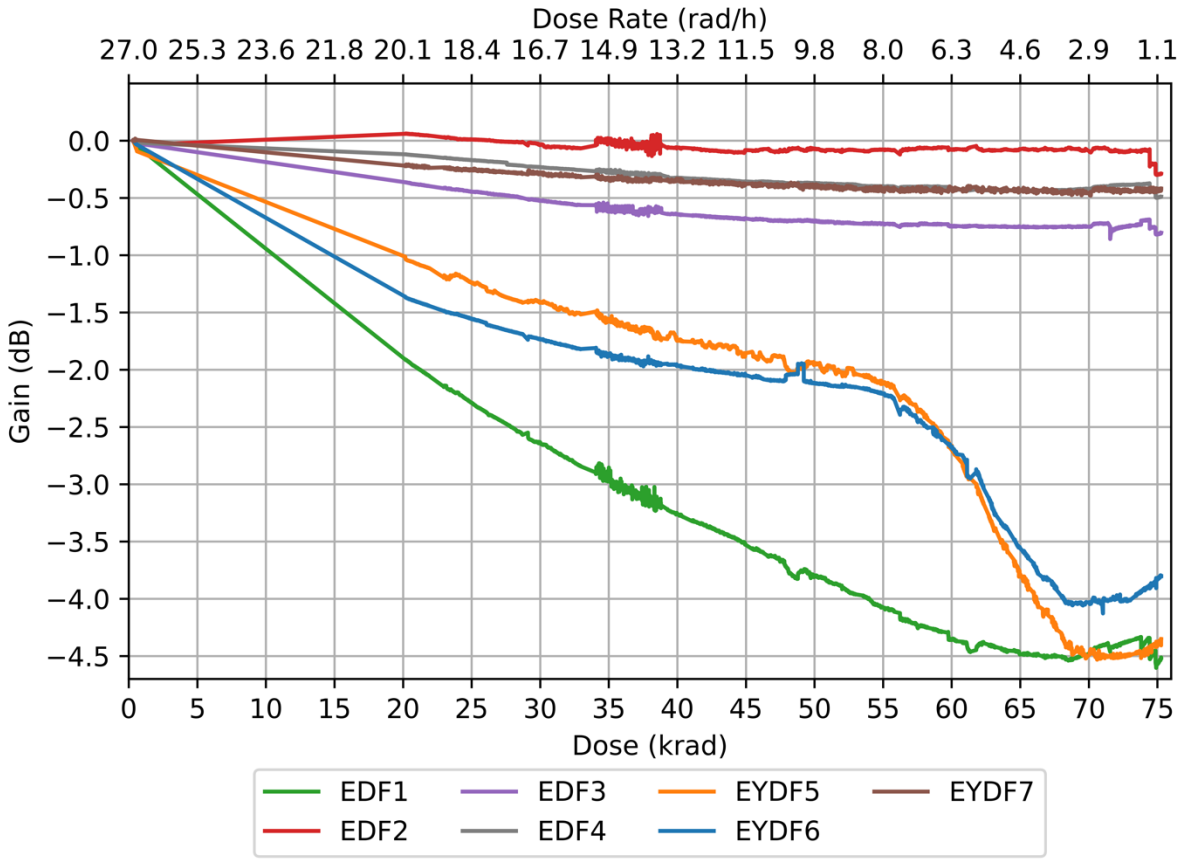

Figure 6.4 Gain of each fiber in active form, undergoing photobleaching, versus the dose going up to 75 krad with the dose rate associated.

The new data shows a fast gain decrease between 55 and 69 krad for two high-power fibers, EYDF5 and EYDF6. This significant change in slope needs more investigation to be clarified. A technical problem may cause it since they were connected to the same source, as shown in Figure 5.6. However, all the fibers gain change from decreasing to stable or increasing between 65 krad (4.6 rad/h) and 70 krad (2.9 rad/h) even if they were still under irradiation.

In the cases where the gain is stable, the two opposing mechanisms affecting the gain, the creation of point defects by radiation and their bleaching, are at the same rate. For the positive slope, the photobleaching takes over the radiation point defect creation by decreasing them faster than the radiation is creating them. Those results support the conclusion that at a low dose rate, the efficiency of the REDFs will reduce slower than at a higher one for the fibers tested. Once again, more investigation needs to be done on fibers EYDF5 and EYDF6 for their fast gain decrease at a dose rate between 8 rad/h and 3.3 rad/h. However, the results proved that the gain stops decreasing up to a certain dose rate threshold with a preliminary conclusion that the photobleaching takes over the radiation defect creation at that moment.

CHAPTER 7 CONCLUSION

7.1 Summary of the results

This work presents the achievement of a new gamma-ray irradiator for terrestrial accelerated-radiation tests using ^{46}Sc sources instead of the commonly used ^{60}Co. The asset of this irradiator is its characteristic of irradiating REDFs at a lower dose rate, closer to which optical fibers are exposed in satellites (0.1-10 rad/h). This allows studying the intensity of the RIA as a function of a low dose rate since its controversy in the literature. In this irradiation, the dose rate was from 27 to 1.1 rad/h, in comparison with the dose rate between 200 and 400 rad/h generally used with a ^{60}Co source. This irradiator also allowed the irradiation of four sets of seven REDFs in active and passive forms. Two sets of passive fibers were irradiated for a total dose of 30 krad and one for 60 krad while the active fibers were irradiated up to 75 krad, which provides a comparison of the effect of photobleaching and photo-annealing over RIA.

To complete this irradiator several steps have been carried out: i) the mechanical design, ii) the modeling and the optimization of the dose received by the fibers, iii) the activation of the sources, iv) the setup of the irradiation test with the passive and active fiber in the laboratory.

The mechanical assembly was designed to fit in the laboratory cylindrical lead shield, where the irradiation took place. This cylindrical irradiator was mainly 3D printed made of PLA with the bottom part in aluminium with a heatsink to dissipate the heat generated by the active fibers. The four sources of ^{46}Sc were located on the revolution axis of the cylindrical irradiator with the fibers spooled on its surface. The cylinder was 208 mm in height with a diameter of 101.6 mm for the part in PLA and 102.1 mm for the aluminium part.

Along with the design of the irradiator, the modeling of the gamma irradiation on the fibers was used to find the optimized configuration for a quasi-homogenous dose over all the fibers. It modeled the shape of the dose on the fiber by decomposing the sources into radiation source points and considering the self-shielding of the ^{46}Sc sources and the gamma-ray attenuation. The desired configuration was achieved by optimizing the activity and the position of each ^{46}Sc vial used. The dose of the four vials of ^{46}Sc was $A_{2_{Sc}} = 0.71\, A_{1_{Sc}}$, $A_{3_{Sc}} = 0.68\, A_{1_{Sc}}$, $A_{1_{Sc}} = A_{4_{Sc}}$ to obtain a maximum dose variation of ± 1 % on the fibers.

Before the beginning of the irradiation, an optoelectronic setup was mounted in the laboratory for the seven fibers in active mode. Three sources were used for the signal of the seven REDFAs. In this setup, only the REDFs were under irradiation and the output power of the REDFs in active form was monitored using one power meter moving on a mechanical stage.

To start the irradiation of the fibers, the four vials of scandium were activated by neutron activation in the SLOWPOKE-2 nuclear reactor to the relative activity given by the previous model. The sources were activated between 1.19 and 1.75 GBq. With this activation, the initial dose rate was 27 rad/h and reached 1.1 rad/h at 75 krad.

The first set of passive fibers was taken out of the irradiation after 59 days with a total dose of 30.2 krad while the second one was taken out after 174 days with a total dose of 59.8 krad. The fibers in active form continued their irradiation up to 75 krad. The data of the active REDFs shows that between 65 krad (4.6 rad/h) and 70 krad (2.9 rad/h), the fibers gain began to be stable or to increase. This has shown that at a dose rate between 2.9 and 4.6 rad/h, the photobleaching takes over the radiation defect creation, the two opposing mechanisms affecting the fiber gain during the irradiation. However, the two high-power fibers, EYDF5 and EYDF6 showed a significant decrease in the gain slope between 55 and 69 krad (8 and 3 rad/h). These results need more investigation to be clarified and may be caused by a technical problem since they were the only two fibers connected to the same source. These results from the active fibers showed that the efficiency of REDFs depends on the dose rate. However, it’s not possible to conclude the dose rate effect on the RIA since all fibers showed a lower RIA with a lower dose rate for a dose rate lower than 2.9 rad/h but two REDFs showed a considerable decrease in gain at dose rates between 8 and 3 rad/h.

7.2 Recommendations for further research

This project aims to study the RIA as a function of the dose rate for REDFs and compare the photobleaching and photo-annealing. This thesis presents the first step of this project, developing and using a low dose rate irradiator for REDFs with a preview of the data taken during and after irradiation.

For the data analysis, measurement needs to be continued for the photo-annealing of the passive fibers. First, analysis and comparison of the two sets of 30 krad fibers irradiated at different dose rates must be made. This comparison will define how the dose rate affects the gain of the passive fibers. Afterward, comparing the fibers in active and passive form for the same dose will give a better knowledge of the difference in the recovery of the gain for photobleaching and photo-annealing. It will also provide better information on the difference in gain between the optical amplifier used in a satellite and the redundant optical amplifier in backup in passive form when it needs to be used. The last comparison for the complete analysis is the comparison between the fibers irradiated in this project with the same fibers irradiated with the commonly ^{60}Co sources. This comparison will put into perspective if the standard radiation test with a dose rate between 200 and 400 rad/h is appropriate for space qualification.

Also, a mathematical model can be developed based on the data taken for creating and annealing the CC causing the RIA according to the dose, dose rate, photobleaching and photo-annealing.

REFERENCES

Bibliography

[1] S. B. Poole, D. N. Payne, and M. E. Fermann, "Fabrication of low-loss optical fibres containing rare-earth ions," *Electronics Letters*, vol. 21, no. 17, pp. 737-8, 08/15 1985, doi: 10.1049/el:19850520.

[2] R. J. Mears, L. Reekie, I. M. Jauncey, and D. N. Payne, "Low-noise erbium-doped fibre amplifier operating at 1.54 um," *Electronics Letters*, vol. 23, no. 19, pp. 1026-8, 1987, doi: 10.1049/el:19870719.

[3] W. A. Gambling, "The rise and rise of optical fibers," *IEEE Journal of Selected Topics in Quantum Electronics*, vol. 6, no. 6, pp. 1084-93, 11/ 2000, doi: 10.1109/2944.902157.

[4] B. J. Ainslie, "A review of the fabrication and properties of erbium-doped fibers for optical amplifiers," *Journal of Lightwave Technology*, vol. 9, no. 2, pp. 220-227, 1991, doi: 10.1109/50.65880.

[5] E. Desurvire, J. R. Simpson, and P. C. Becker, "High-gain erbium-doped traveling-wave fiber amplifier," *Optics Letters*, vol. 12, no. 11, pp. 888-90, 11/ 1987, doi: 10.1364/OL.12.000888.

[6] H. Kaushal and G. Kaddoum, "Optical Communication in Space: Challenges and Mitigation Techniques," *IEEE Communications Surveys and Tutorials*, vol. 19, no. 1, pp. 57-96, 2017, doi: 10.1109/COMST.2016.2603518.

[7] B. P. Fox, K. Simmons-Potter, D. A. V. Kliner, and S. W. Moore, "Effect of low-earth orbit space on radiation-induced absorption in rare-earth-doped optical fibers," *Journal of Non-Crystalline Solids*, vol. 378, pp. 79-88, 2013, doi: 10.1016/j.jnoncrysol.2013.06.009.

[8] R. J. Bussjager, M. J. Hayduk, and S. T. Johns, "Comparison of radiation-induced passive and dynamic responses in two erbium-doped fiber lasers," in *2002 IEEE Aerospace Conference Proceedings, 9-16 March 2002*, Piscataway, NJ, USA, 2002, vol. vol.3: IEEE, in 2002 IEEE Aerospace Conference Proceedings (Cat. No.02TH8593), pp. 3-1369, doi: 10.1109/AERO.2002.1035270. [Online]. Available: http://dx.doi.org/10.1109/AERO.2002.1035270

[9] J. Cao, S. Jian, M. Wang, J. Zhang, W. Ren, and Y. Bai, "Co60 radiation effects on rare earth doped fibers," *Optik*, vol. 127, no. 4, pp. 1677-1680, 2016, doi: 10.1016/j.ijleo.2015.11.035.

[10] S. Girard *et al.*, "Recent advances in radiation-hardened fiber-based technologies for space applications," *Journal of Optics*, vol. 20, no. 9, p. 48, 2018, doi: 10.1088/2040-8986/aad271.

[11] B. P. Fox, K. Simmons-Potter, W. J. Thomes, Jr., D. C. Meister, R. P. Bambha, and D. Kliner, "Temperature and dose-rate effects in gamma irradiated rare-earth doped fibers," in *Nanophotonics and Macrophotonics for Space Environments II, 11 Aug. 2008*, USA, 2008, vol. 7095: SPIE - The International Society for Optical Engineering, in Proc. SPIE - Int. Soc. Opt. Eng. (USA), pp. 70950-1, doi: 10.1117/12.795595. [Online]. Available: http://dx.doi.org/10.1117/12.795595

[12] O. Gilard *et al.*, "Theoretical explanation of enhanced low dose rate sensitivity in erbium-doped optical fibers," *Applied Optics*, vol. 51, no. 13, pp. 2230-2235, May 1 2012, doi: 10.1364/AO.51.002230.

[13] M. Lezius *et al.*, "Radiation Induced Absorption in Rare Earth Doped Optical Fibers," *IEEE Transactions on Nuclear Science*, vol. 59, no. 2, p. 9, 2012, doi: 10.1109/tns.2011.2178862.

[14] J. Budroweit and H. Patscheider, "Risk Assessment for the Use of COTS Devices in Space Systems under Consideration of Radiation Effects," *Electronics*, vol. 10, no. 9, p. 1008, 2021. [Online]. Available: https://www.mdpi.com/2079-9292/10/9/1008.

[15] A. Ladaci *et al.*, "Optimized radiation-hardened erbium doped fiber amplifiers for long space missions," *Journal of Applied Physics*, vol. 121, no. 16, 2017, doi: 10.1063/1.4981532.

[16] E. Haddad *et al.*, "Comparison of gamma radiation effect on erbium doped fiber amplifiers," presented at the International Conference on Space Optics — ICSO 2016, Biarritz, France, 2016.

[17] G. M. Williams, B. M. Wright, W. D. Mack, and E. J. Friebele, "Projecting the performance of erbium-doped fiber devices in a space radiation environment," in *Optical Fiber Reliability and Testing, 19-20 Sept. 1999*, USA, 1999, vol. 3848: SPIE-Int. Soc. Opt. Eng., in Proc. SPIE - Int. Soc. Opt. Eng. (USA), pp. 271-80, doi: 10.1117/12.372781. [Online]. Available: http://dx.doi.org/10.1117/12.372781

[18] R. G. Ahrens *et al.*, "Radiation reliability of rare earth doped optical fibers for laser communication systems (LT)," in *Proceedings of Conference on Military Communications (MILCOM'99), 31 Oct.-3 Nov. 1999*, Piscataway, NJ, USA, 1999, vol. vol.1: IEEE, in MILCOM 1999. IEEE Military Communications. Conference Proceedings (Cat. No.99CH36341), pp. 694-7, doi: 10.1109/MILCOM.1999.822773. [Online]. Available: http://dx.doi.org/10.1109/MILCOM.1999.822773

[19] B. Brichard, A. F. Fernandez, H. Ooms, and F. Berghmans, "Gamma dose rate effect in erbium-doped fibers for space gyroscopes," presented at the Finds and Results from the Swedish Cyprus Expedition: A Gender Perspective at the Medelhavsmuseet, Stockholm, Sweden, 2003.

[20] J. Thomas *et al.*, "Experimental demonstration of the switching dose-rate method on doped optical fibers," in *International Conference on Space Optics 2010, ICSO 2010, October 4, 2010 - October 8, 2010*, Rhodes Island, Greece, 2017, vol. 10565: SPIE, in Proceedings of SPIE - The International Society for Optical Engineering, doi: 10.1117/12.2309255. [Online]. Available: http://dx.doi.org/10.1117/12.2309255

[21] E. J. Friebele, C. C. Baker, A. Burdett, J. S. Sanghera, M. J. LuValle, and S. Logothetis, "Radiation-Resistant Nanoparticle Erbium Doped Fibers for High Power Space Laser Communications," *SPIE*, vol. 1120614, 2019, doi: 10.1117/12.2552535.

[22] M. Mena *et al.*, "Monitoring the Propulsion System of PROBA-2 with Optical Fiber Sensors during 9 Years," presented at the PROBA-2 Symposium, 2019.

[23] H. Henschel and O. Köhn, "Regeneration of Irradiated Optical Fibres by Photobleaching?," presented at the Conference: 5. European conference on radiation and its effects on components and systems, France, 1999.

[24] A. Ladaci, "Rare earth doped optical fibers and amplifiers for space applications," Université de Lyon, Politecnico di Bari. Dipartimento di Ingegneria Elettrica e dell'Informazione (Italia), 2017LYSES027, 2017. [Online]. Available: https://tel.archives-ouvertes.fr/tel-02109151

[25] Ö. AMUTKAN, "Space radiation environment and radiation hardness assurance tests of electronic components to be used in space missions," Physics, Middle East Technical University, 2010. [Online]. Available: http://etd.lib.metu.edu.tr/upload/12612238/index.pdf

[26] T. Ersmark, "Geant4 Monte Carlo Simulations of the International Space Station Radiation Environment," PhD dissertation, Physics, KTH, 2006. [Online]. Available: http://urn.kb.se/resolve?urn=urn:nbn:se:kth:diva-4007

[27] M. N. Ott, "Space flight applications of optical fiber; 30 years of space flight success," in *2010 IEEE Avionics, Fiber-Optics and Photonics Technology Conference, AVFOP 2010*, 2010: IEEE Computer Society, in 2010 IEEE Avionics, Fiber-Optics and Photonics Technology Conference, AVFOP 2010, pp. 3-4, doi: 10.1109/AVFOP.2010.5637515. [Online]. Available: http://dx.doi.org/10.1109/AVFOP.2010.5637515

[28] D. B. Coyle, "Applications of Fiber Amplifiers for Space: Laser Altimetry and Mapping," presented at the The First ESA-NASA Working Meeting on Optoelectronics, Noordwijk, The Netherlands, 5 october, 2005.

[29] D. Guilhot and P. Ribes-Pleguezuelo, "Laser Technology in Photonic Applications for Space," *Instruments*, vol. 3, no. 3, p. 50 (25 pp.), 2019, doi: 10.3390/instruments3030050.

[30] W. Fourcault, J. M. Leger, V. Costes, I. Fratter, and L. Mondin, "Athermal fiber laser for the SWARM absolute scalar magnetometer," in *International Conference on Space Optics 2010, ICSO 2010, October 4, 2010 - October 8, 2010*, Rhodes Island, Greece, 2017, vol. 10565: SPIE, in Proceedings of SPIE - The International Society for Optical Engineering, doi: 10.1117/12.2309215. [Online]. Available: http://dx.doi.org/10.1117/12.2309215

[31] E. Desurvire, *Erbium-Doped Fiber Amplifiers: Principles and Applications*. Wiley, 1994.

[32] P. M. Becker, A. A. Olsson, and J. R. Simpson, *Erbium-Doped Fiber Amplifiers: Fundamentals and Technology*. Elsevier Science, 1999.

[33] J. D. Minelly *et al.*, "Diode-array pumping of Er3+/Yb3+ Co-doped fiber lasers and amplifiers," *IEEE Photonics Technology Letters*, vol. 5, no. 3, pp. 301-303, 1993, doi: 10.1109/68.205618.

[34] S. Girard *et al.*, "Radiation effects on silica-based optical fibers: Recent advances and future challenges," *IEEE Transactions on Nuclear Science*, vol. 60, no. 3, pp. 2015-2036, 2013, doi: 10.1109/TNS.2012.2235464.

[35] S. Girard *et al.*, "Overview of radiation induced point defects in silica-based optical fibers," *Reviews in Physics*, vol. 4, 2019, doi: 10.1016/j.revip.2019.100032.

[36] T. S. Rose, M. S. Hopkins, and R. A. Fields, "Characterization and control of gamma and proton radiation effects on the performance of Nd:YAG and Nd:YLF lasers," *IEEE Journal of Quantum Electronics*, vol. 31, no. 9, pp. 1593-602, 1995, doi: 10.1109/3.406369.

[37] B. V. I. Brichard, S.; Hendrickx, C.;, "On the use of photobleaching and thermal annealing to recover the optical transmission in irradiated pure silica fibres," presented at the 2007 9th European Conference on Radiation and Its Effects on Components and Systems (RADECS 2007), Deauville, France, 2007.

[38] M. Kassakov, "Analyse par activation neutronique de substances ayant des sections efficaces macroscopiques élevées pour l'absorption de neutrons thermiques," Mémoire de maîtrise, École Polytechnique de Montréal, 2006. [Online]. Available: https://publications.polymtl.ca/7820/

[39] G. F. Knoll, *Radiation Detection and Measurement*. Wiley, 2000.

[40] H. RAOUAFI, "Étude numérique de l'autoprotection spatiale dans les échantillons fortement absorbants irradiés dans le réacteur Slowpoke," Mémoire de maîtrise, École Polytechnique Montréal, 2012. [Online]. Available: https://publications.polymtl.ca/947/

[41] I. Feister and L. F. Curtiss, "Disintegration of scandium," *United States Bureau of Standards -- Journal of Research*, vol. 38, no. 4, pp. 411-414, 1947.

[42] (2019). *SLOWPOKE Nuclear Reactors in Canada*. [Online] Available: https://www.rmc-cmr.ca/en/chemistry-and-chemical-engineering/slowpoke-nuclear-reactors-canada

[43] F. Puig and H. Dennis, "SLOWPOKE-2 alternative core loading configurations analysis for highly improved reactor performance," *Annals of Nuclear Energy*, vol. 128, pp. 216-30, 06/ 2019, doi: 10.1016/j.anucene.2018.12.016.

[44] O. E. Hajjaji, "La physique du réacteur slowpoke-2 de l'École polytechnique " Thèse de doctorat, École Polytechnique de Montréal, 1999. [Online]. Available: https://publications.polymtl.ca/7532/

[45] Z. Sodnik, B. Furch, and H. Lutz, "Optical Intersatellite Communication," *IEEE Journal of Selected Topics in Quantum Electronics*, vol. 16, 2010, doi: 10.1109/JSTQE.2010.2047383.

[46] E. J. Friebele, K. J. Long, C. G. Askins, M. E. Gingerich, M. J. Marrone, and D. L. Griscorn, "Overview of radiation effects in fiber optics," presented at the Proceedings of SPIE - The International Society for Optical Engineering, Albuquerque, NM, United states, 1985, 70.

[47] (2017). *Radionuclide Information Booklet*.

[48] "Radionuclide Data Sheet Scandium – 46." Environmental Health & Safety University of Missouri. https://ehs.missouri.edu/sites/ehs/files/pdf/isotopedata/sc-46.pdf (accessed 2021).

[49] "Radionuclide Data Sheet Cobalt - 60." Environmental Health & Safety University of Missouri. https://ehs.missouri.edu/sites/ehs/files/pdf/isotopedata/co-60.pdf (accessed 2021).

[50] D. S. Smith and M. G. Stabin, "Exposure rate constants and lead shielding values for over 1,100 radionuclides," *Health Phys*, vol. 102, no. 3, pp. 271-91, Mar 2012, doi: 10.1097/hp.0b013e318235153a.

[51] PRUSA. "Prusament PLA Prusa Orange 1kg." https://www.prusa3d.com/product/prusament-pla-prusa-orange-1kg/ - downloads (accessed 2022).

[52] C. Chilian, "Extending neutron activation analysis to materials with high concentrations of neutron absorbing elements," Thèse de doctorat, École Polytechnique de Montréal, 2008. [Online]. Available: https://publications.polymtl.ca/8124/

[53] J. H. Hubbell and S. M. Seltzer, "Tables of X-Ray Mass Attenuation Coefficients and Mass Energy-Absorption Coefficients," doi: 10.18434/T4D01F.

[54] ENSDF. *Decay Radiation database*, National Nuclear Data Center, 2022. [Online]. Available: https://www.nndc.bnl.gov/nudat3/indx_dec.jsp

[55] R. Biswas, H. Sahadath, A. S. Mollah, and M. F. Huq, "Calculation of gamma-ray attenuation parameters for locally developed shielding material: Polyboron," *Journal of Radiation Research and Applied Sciences*, vol. 9, no. 1, pp. 26-34, 2019, doi: 10.1016/j.jrras.2015.08.005.

[56] "DWDM CombSources." MPB Communications Inc. https://mpbcommunications.com/en/ofc2021/pdfs/DWDM CombSource Series.pdf (accessed February 11, 2022).